

HYBRIDIZATION OF SINGLE FLASH GEOTHERMAL POWER PLANT WITH
BIOMASS DRIVEN SCO₂ TOPPING CYCLE

A THESIS SUBMITTED TO
THE GRADUATE SCHOOL OF NATURAL AND APPLIED SCIENCES
OF
MIDDLE EAST TECHNICAL UNIVERSITY

BY

BALKAN MUTLU

IN PARTIAL FULFILLMENT OF THE REQUIREMENTS
FOR
THE DEGREE OF MASTER OF SCIENCE
IN
MECHANICAL ENGINEERING

SEPTEMBER 2020

Approval of the thesis:

**HYBRIDIZATION OF SINGLE FLASH GEOTHERMAL POWER PLANT
WITH BIOMASS DRIVEN SCO₂ TOPPING CYCLE**

submitted by **BALKAN MUTLU** in partial fulfillment of the requirements for the degree of **Master of Science in Mechanical Engineering Department, Middle East Technical University** by,

Prof. Dr. Halil Kalipçılar
Dean, Graduate School of **Natural and Applied Sciences** _____

Prof. Dr. Mehmet Ali Sahir Arıkan
Head of Department, **Mechanical Engineering** _____

Assist. Prof. Dr. Feyza Kazanç Özerinç
Supervisor, **Mechanical Engineering, METU** _____

Prof. Dr. Derek Keith Baker
Co-supervisor, **Mechanical Engineering, METU** _____

Examining Committee Members:

Prof. Dr. Ahmet Yozgatlıgil
Mechanical Engineering, METU _____

Assist. Prof. Dr. Feyza Kazanç Özerinç
Mechanical Engineering, METU _____

Prof. Dr. Derek Keith Baker
Mechanical Engineering, METU _____

Assist. Prof. Dr. Zöhre Kurt
Environmental Engineering, METU _____

Assoc. Prof. Dr. Gökhan KİRKİL
Energy Systems Engineering, Kadir Has University _____

Date:

I hereby declare that all information in this document has been obtained and presented in accordance with academic rules and ethical conduct. I also declare that, as required by these rules and conduct, I have fully cited and referenced all material and results that are not original to this work.

Name, Surname: Balkan Mutlu

Signature :

ABSTRACT

HYBRIDIZATION OF SINGLE FLASH GEOTHERMAL POWER PLANT WITH BIOMASS DRIVEN sCO₂ TOPPING CYCLE

Mutlu, Balkan

M.S., Department of Mechanical Engineering

Supervisor: Assist. Prof. Dr. Feyza Kazanç Özerinç

Co-Supervisor: Prof. Dr. Derek Keith Baker

September 2020, 108 pages

This study investigates the hybridization scenario of Kızıldere-1 single flash geothermal power plant with a biomass driven recompression sCO₂ topping cycle where a solid local biomass source, olive residue, is used as a fuel. The combustion characteristics, kinetic parameters and slagging-fouling potential of the fuel are determined using TGA, Coats-Redfern Method and XRF analysis, respectively. The apparent activation energies for two observed major stages of combustion under the heating rate of 20 °C/min are calculated as 32.6 and 17 kJ/mol, respectively. The hybrid power plant is modeled using the simulation software EBSILON Professional. Supercritical CO₂ (sCO₂) cycle is specifically chosen due to having more compact footprint compared to steam cycles and the potential to be ramped up and down more rapidly, thus enabling flexible operation. A synergy between the topping and bottoming cycle is achieved by a good temperature match between the coupling heat exchanger where the waste heat from the topping cycle is utilized in the bottoming cycle. The high temperature heat addition problem to the sCO₂ cycle is also eliminated utilizing the whole heat in the flue gas in the bottoming cycle. Hybrid cycle thermal efficiency and

biomass-to-electricity conversion of 24.5% and 22% are achieved, respectively. The net power output of the hybrid power plant is increased to 17.8 MWe while the net production of the topping cycle is kept at 3.2 MWe. Corresponding fuel consumption for the hybrid plant is found as 2.2 kg/s.

Keywords: hybridization, geothermal, biomass, sCO₂ cycle

ÖZ

TEK BASINÇ KADEMELİ JEOTERMAL ENERJİ SANTRALİNİN BİYOKÜTLE KAYNAKLI sCO₂ ÇEVİRİMİ İLE HİBRİDİZASYONU

Mutlu, Balkan

Yüksek Lisans, Makina Mühendisliği Bölümü

Tez Yöneticisi: Dr. Öğr. Üyesi. Feyza Kazanç Özerinç

Ortak Tez Yöneticisi: Prof. Dr. Derek Keith Baker

Eylül 2020 , 108 sayfa

Bu çalışma, katı bir biyokütle kaynağı olan zeytin prinasının yakıt olarak kullanıldığı, biyokütle ile güç sağlanan sCO₂ çevrimi ile Kızıldere-1 tek basınç kademeli jeotermal enerji santralinin hibridizasyonunu konu almaktadır. Yakıtın yanma özellikleri, kinetik parametreleri ve cüruflaşma potansiyeli; sırasıyla TGA, Coats-Redfern Metodu ve XRF analizi kullanılarak belirlenmiştir. 20 ° C / dk ısıtma hızı altındaki TGA analizinde gözlenen iki ana yanma aşaması için aktivasyon enerjileri sırasıyla 32.6 ve 17 kJ / mol olarak hesaplanmıştır. Hibrit enerji santrali EBSILON Professional simülasyon yazılımı kullanılarak modellenmiştir. Süperkritik CO₂ (sCO₂) döngüsü, buhar döngülerine kıyasla daha kompakt olması ve inişli çıkışlı güç üretimini desteklemesi nedeniyle hibrit santralin esnekliğini artırması yüzünden tercih edilmiştir. sCO₂ ve rankin çevrimleri arasındaki sinerji, sCO₂ çevrimindeki atık ısının rankin çevrimine aktarıldığı ısı eşanjöründe elde edilen sıcaklık uyumu ile sağlanmıştır. sCO₂ çevrimine yüksek sıcaklıkta ısı transferi sorunu, baca gazındaki ısının rankin çevrimine aktarılması sayesinde giderilmiştir. Hibrit çevrimin termal verimliliği ve biyokütle-

nin elektriğe dönüşüm verimleri sırasıyla 24.5% ve 22% olarak bulunmuştur. Hibrit santralin net güç üretimi 17.8 MWe'ye çıkarılırken, sCO₂ çevriminin net üretimi 3.2 MWe olarak bulunmuştur. Hibrit santralin azami yakıt tüketimi 2,2 kg / s olarak hesaplanmıştır.

Anahtar Kelimeler: hibridizasyon, jeotermal, biyokütle, sCO₂ çevrimi

To my only Pütür

ACKNOWLEDGMENTS

I, first of all, would like to thank Prof. Derek Baker for his academic support, valuable comments and important time. I had the opportunity to participate in a project which in some way interests my home town, Aydın. I owe sincere thanks to Dr. Feyza Kazanç Özerinç for her guidance and vision. I would not have competence in simulation software EBSILON if I had not take her undergraduate course on steam power plants.

The study on hybridization of geothermal in this thesis is made possible by a long line of research initiated by METU ME graduates who I had the opportunity to get to know personally, Cihan Özalevli and Nima Bonyadi. Thank you for your earlier contributions.

I would like to thank to my fellow graduate students from CCTL; Duarte, Kaan, Şener and Burak. They helped me a lot with the experimental studies and answered all my questions with great patience. I would also like to thank heat lab technician of our department, Mustafa abi for the enlightening conversations during our tea sessions.

I would like to thank to my family for their generosity, kindness and their endless support. I do not know how to express my deep gratitude for your sacrifices, generosity, selflessness, patience, and love.

Lastly, I was blessed with a wonderful friend who has shown endless patience during my studies. My dearest friend Gamze, thank you for always being there for me when I needed you. Thank you so much for your devoted love and priceless companionship. Thank you for becoming my family.

The author acknowledges the financial support provided from EU-H2020 Project 818576 GeoSmart: Technologies for geothermal to enhance competitiveness in smart and flexible operation. The author would also like to thank Zorlu Energy for their help on sharing operational data of their power plant.

TABLE OF CONTENTS

ABSTRACT	v
ÖZ	vii
ACKNOWLEDGMENTS	x
TABLE OF CONTENTS	xi
LIST OF TABLES	xiv
LIST OF FIGURES	xvi
LIST OF ABBREVIATIONS	xx
CHAPTERS	
1 INTRODUCTION	1
1.1 Motivation and Problem Definition	2
1.2 Contributions and Novelties	3
1.3 Potential Impacts	4
2 LITERATURE REVIEW	5
2.1 Utilization of Biomass	5
2.1.1 Biomass Energy Conversion Technologies for Power Production	5
2.1.2 Biomass Combustion	7
2.1.3 Thermogravimetric Analysis for Biomass Characterization	8
2.1.4 Combustion Kinetics	10

2.2	sCO ₂ Power Cycles	15
2.2.1	sCO ₂ Cycle Configurations	17
2.2.1.1	Simple Recuperated sCO ₂ Cycle	18
2.2.1.2	Recompression sCO ₂ Cycle	20
2.2.1.3	Partial Cooling sCO ₂ Cycle	22
2.3	Selected studies on sCO ₂ Cycles and Hybridization of Geothermal . .	24
3	MATERIALS AND METHODS FOR BIOMASS CHARACTERIZATION	29
3.1	Background of the Obtained Biomass	29
3.2	Fuel Preparation	31
3.3	Experiments	33
3.4	Methodology for Biomass Characterization	36
3.4.1	Kinetic Parameters	36
3.4.2	Higher Heating Value	39
3.4.3	Fouling and Slagging Potential	41
3.4.4	Lignocellulosic Composition and Combustibility Index	43
4	BIOMASS CHARACTERIZATION RESULTS	47
4.1	Results based on TGA data	47
4.2	Results on Kinetic Parameters	50
4.3	Results on Slagging and Fouling Potential of the Fuel	55
5	METHODOLOGY FOR HYBRIDIZATION	57
5.1	Mathematical Background	57
5.1.1	Single Flash Geothermal Steam Rankine Cycle Equations . . .	57
5.1.2	The sCO ₂ Cycle Equations	62

5.2	Design of the Hybrid Power Plant	65
5.2.1	Model Verification	65
5.2.2	Design Parameters of the Hybrid Model	68
6	HYBRIDIZATION RESULTS	83
7	CONCLUSION	91
7.1	Economical and Environmental Impacts	92
7.2	Challenges and Future Work	94
	REFERENCES	97

LIST OF TABLES

TABLES

Table 2.1 Overview of the selected standalone sCO ₂ cycles. P (bar), T (°C). . .	17
Table 2.2 Strengths and weaknesses of the analyzed sCO ₂ cycles.	22
Table 2.3 Design conditions of RC sCO ₂ cycle by Utamura as adapted to Figure 2.7	28
Table 3.1 Elemental analysis of the studied olive residue.	35
Table 3.2 Reaction models and corresponding $f(\alpha)$ and $g(\alpha)$ functions.	38
Table 3.3 Higher heating value estimation formulas for biomass fuels.	40
Table 3.4 Approximate ranges for the selected slagging and fouling indices. . .	44
Table 3.5 Correlation range of the method developed by Sheng and Azevedo. .	45
Table 4.1 Weight losses for defined stages of combustion (in wt.%, dry basis), and unaccounted weight for studied OR.	49
Table 4.2 Characteristic temperatures (T_D – Decomposition Temperature; T_{ig} – Ignition Temperature; T_P – Peak Temperature; T_B – Burnout Tempera- ture) of the studied OR in °C and Combustibility Index, S for Stage B . . .	49
Table 4.3 Temperature intervals, correspondent models and the kinetic param- eters	51
Table 4.4 Apparent activation energy values for the selected biomass fuels. . .	53
Table 4.5 Slagging and Fouling Potential of the studied fuel.	55

Table 5.1	Base inputs for the parametric analysis on the flow rates.	76
Table 5.2	Model verification results based on the model of Manente and Lazzaretto.	81
Table 5.3	Flue gas mass flow rate, temperature and composition for the studied OR.	82
Table 6.1	Optimized design parameters.	83
Table 6.2	Intensive properties for States 1-23 in Figure 5.9.	84
Table 6.3	Energy accounting for the hybrid power plant.	85
Table 6.4	Comparison of efficiencies with those of Manente and Lazzaretto . .	85

LIST OF FIGURES

FIGURES

Figure 1.1	Geothermal Resource Map of Turkey	1
Figure 1.2	The distribution of provinces on their production of table olive and olive oil.	2
Figure 1.3	The view of KZD-1 GEPP from Denizli-Aydın highway. The olive trees are short, shrub-like trees in pale forest green shade.	3
Figure 2.1	Biomass energy conversion technologies. Note that anaerobic digestion is a biological process whereas gasification and combustion are thermochemical processes.	6
Figure 2.2	Steps of solid fuel combustion	8
Figure 2.3	Illustration of characteristic temperatures.	10
Figure 2.4	sCO ₂ Application Map. Note: sCO ₂ – Supercritical CO ₂ ; ORC – Organic Rankine Cycle; WHR – Waste Heat Recovery.	16
Figure 2.5	General layout and T-s diagram of the simple recuperated sCO ₂ cycle. The layout is generated using the software EBSILON®Professional.	18
Figure 2.6	Isobaric specific heat of CO ₂ with varying temperature at different supercritical pressures. The values are obtained using CoolProp add-in in MS Excel.	19
Figure 2.7	General layout and T-s diagram of the Recompression sCO ₂ cycle. The layout is generated using the software EBSILON®Professional.	21

Figure 2.8	General layout and T-s diagram of the Partial Cooling sCO ₂ cycle. The layout is generated using the software EBSILON®Professional.	23
Figure 2.9	Layout of the solar-geothermal hybrid power plant by Bonyadi et. al.	25
Figure 3.1	Distribution of olive oil extraction technologies for European countries.	30
Figure 3.2	Overview of oil extraction methods.	31
Figure 3.3	Muffle furnace at CCTL METU	32
Figure 3.4	Ring mill grinder at Mineral Processing Laboratory METU	32
Figure 3.5	Sieves and shaker.	32
Figure 3.6	Studied OR in glass veils.	32
Figure 3.7	Perkin Elmer Pyris STA 4000 Thermogravimetric analyzer (right) equipped with Fourier-transform infrared spectrometer (left) at RÜZGEM.	33
Figure 3.8	TGA profile for the proximate analysis.	34
Figure 4.1	TG and DTG profiles for the studied OR under 20 °C/min with indication of characteristic temperatures and combustion stages	48
Figure 4.2	Evaluation of fittings to Stage B and C using reaction mechanism supplied in Table 3.2. O1 – First Order; O2 – Second Order; O3 – Third Order; R2 – Contracting Cylinder; R3 – Contracting Sphere; D1 – 1-D Diffusion Controlled; D2 – Valensi 2-D; D3 – Jander 3-D; D4 – Ginstling-Brounshtein, 3-D. Equation of the lines and the R^2 values are given in cascades as the same color with the fittings.	52
Figure 5.1	T-s diagram for a single flash GEPP	58
Figure 5.2	Direct-contact condenser. Vessel is assumed to be perfectly insulated.	61

Figure 5.3	Representative sketch of the wet cooling tower.	62
Figure 5.4	EBSILON model of KZD-1 GEPP.	65
Figure 5.5	T-s diagram of the KZD-1 model.	66
Figure 5.6	Verification model with design conditions of Utamura	67
Figure 5.7	T-s diagram for the verification model and Utamura	67
Figure 5.8	Modified T-s diagram of KZD-1 with 80% turbine isentropic efficiency.	68
Figure 5.9	Proposed hybrid power plant configuration.	71
Figure 5.10	Results of the parametric analysis on H_2O and CO_2 mass flow rates.	74
Figure 5.11	Trends in thermal efficiencies with variations in part-flow ratio.	77
Figure 5.12	Effect of turbine expansion ratio on the thermal efficiency.	78
Figure 5.13	Effect of turbine expansion ratio on the heat duty of recuperators.	78
Figure 5.14	Effect of turbine expansion ratio on the size of the recuperators.	78
Figure 5.15	Radiative-convective counter-current heater configuration.	80
Figure 5.16	Heat transfer distribution and the flue gas temperature after the radiative section in the proposed heater with varying intermediate steam quality.	82
Figure 6.1	Energetic Results of Hybridized Power Plant. Note the Geothermal Sourced Single-Flash Power Plant and the Bottoming Cycle of the Biomass Sourced Combined-Cycle Power Plant share the same turbine.	86
Figure 6.2	Allocation of biomass heat and power distribution between the cycles.	87

Figure 6.3	Q-T diagram of the radiative-convective heater with assumed TEF=1000°C.	88
Figure 6.4	Q-T diagram of the recuperators.	88
Figure 6.5	Q-T diagram of the coupling heat exchanger (cooler) between topping and bottoming cycles.	89
Figure 6.6	T-s diagram of the proposed topping cycle.	90
Figure 6.7	T-s diagram of the proposed bottoming cycle.	90
Figure 7.1	Electricity Market Price in Turkey for MWh electricity.	93

LIST OF ABBREVIATIONS

ABBREVIATIONS

A	Pro-exponential Factor
AI	Alkali Index
B/A	Base-to-acid Ratio
$B/A(+P)$	Modified Base-to-acid Ratio
Capex	Capital Expenditure
CCF	Combustion Characteristic Factor
CSP	Concentrated Solar Power
DC Condenser	Direct-contact Condenser
DTF	Drop Tube Furnace
E_a	Activation Energy
F_I	Fouling Index
FTIR	Fourier-transform infrared spectroscopy
FWO	Flynn–Wall–Ozawa Method
GE	General Electric
GEPP	Geothermal Electric Power Plant
GTI	Gas Technology Institute
HHV	Higher Heating Value
HTR	High Temperature Recuperator
k	Reaction rate
kWe	Kilowatts electric
KZD-1	Kızıldere-1
LCoE	Levelized Cost of Electricity
LTR	Low Temperature Recuperator

MC	Main Compressor
MSW	Municipal Solid Waste
OP	Olive Pomace
OR	Olive Residue
ORC	Organic Rankine Cycle
PC	Partial cooling
PR	Pressure Ratio
R	Universal Gas Constant
RC	Recompression
S	Combustibility Index
sCO ₂	Supercritical Carbon Dioxide
S_R	Slag Ratio
S_I	Slagging Index
tCO ₂	Transcritical Carbon Dioxide
T_D	Decomposition Temperature
T_P	Peak Temperature
T_{ig}	Ignition Temperature
T_B	Burnout Temperature
TAD	Adiabatic Flame Temperature
TEF	Effective Temperature of Radiation
TIT	Turbine Inlet Temperature
TRL	Technology Readiness Level
WCT	Wet Cooling Tower
WHR	Waste Heat Recovery
λ	Excess air ratio

CHAPTER 1

INTRODUCTION

As of 2019, Turkey has 1,347 MWe installed capacity in geothermal, the fourth largest in the world after the United States, Indonesia and the Philippines [1], and targets 2,000 MWe geothermal power generation capacity by the end of 2020 [2]. Most of Turkey's high temperature geothermal resources are located in Southwest Anatolia as shown in Figure 1.1 [3].

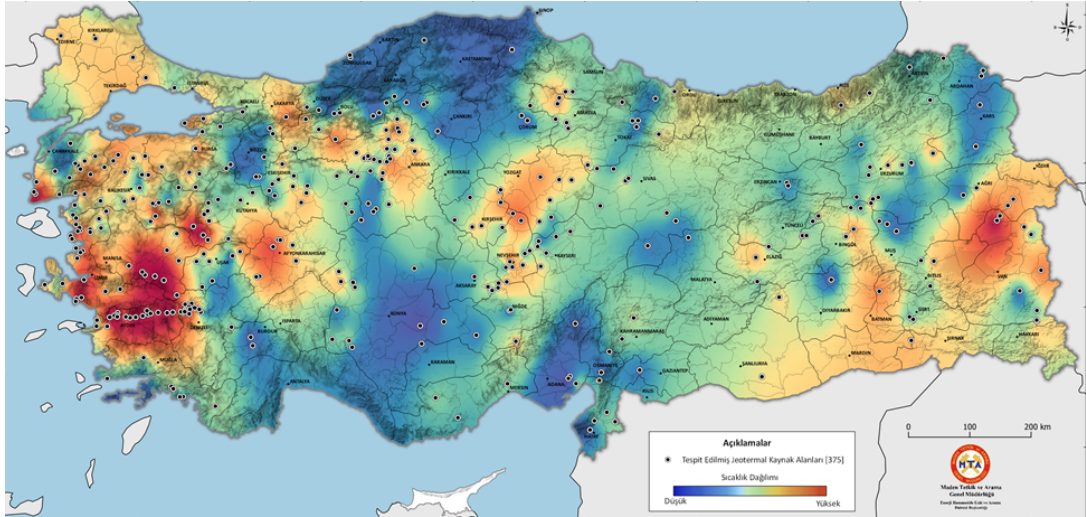


Figure 1.1: Geothermal Resource Map of Turkey as adapted from MTA[3].

Western Anatolia is also a well known region with its olive production. According to Food and Agriculture Organization of the United Nations (FAO) Databank for year the 2018 [4], Turkey is world's 4th biggest olive producer ranked behind Spain, Italy and Morocco where the most of the country's olive yield lies in the Western Anatolia region. Specifically, table olive production is concentrated in Northwest Anatolia while olive oil production is more common in Southwest Anatolia as it can

be seen from Figure 1.2 [5]. The advantageous part of the olive oil production from the biomass perspective is that it creates huge supply for a type of solid biomass fuel called as “olive residue”. Olive residue (OR) is a solid by-product of olive oil production with calorific value around 20 MJ/kg (~4800 kcal/kg).

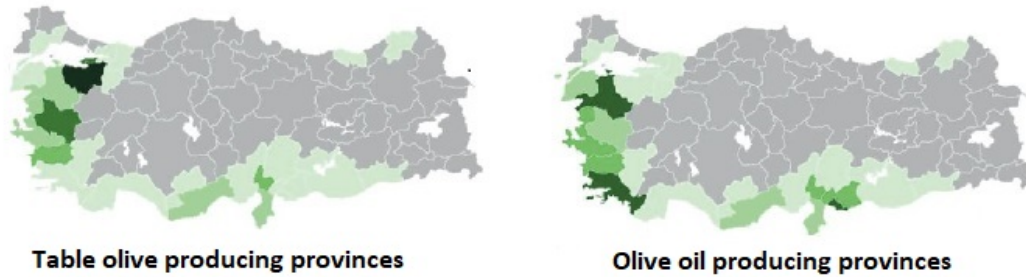


Figure 1.2: The distribution of provinces on their production of table olive and olive oil. The maps are adapted from the country report of International Olive Council[5].

1.1 Motivation and Problem Definition

METU is partner of European Union Horizon 2020 Project GeoSmart (Grant agreement: 818576). Through the original H2020 Call: LC-SC3-RES-12-2018, the European Commission (EC) asked if geothermal can be hybridized with biomass to increase flexibility, and in part funded GeoSmart to explore answers to this question. Although the main aim of project GeoSmart is meeting the different flexibility needs of operating geothermal power plants with low enthalpy and high enthalpy sources at demonstration level, the evaluation of future scenarios, including the synergistic effects of geothermal with other renewable energy resources, is one of the objectives of GeoSmart to offer an insight on hybrid power plant opportunities and make informed future energy investment decisions. In accordance with this purpose, this thesis is aligned with METU’s contribution to GeoSmart, and explores the potential of hybridizing the existing Kızıldere-1 (KZD-1) single flash geothermal electric power plant (GEPP) with biomass driven supercritical CO_2 (sCO₂) cycle. Note that KZD-1 GEPP is owned and operated by Zorlu Energy, which is also a partner in GeoSmart.

KZD-1 GEPP is located right on the Denizli-Aydın border of Turkey. In this specific region, there is coexistence of two renewable energy resources, geothermal and

biomass as highlighted by Figure 1.1 and 1.2. This coexistence is even noticeable from the original photo of KZD-1 GEPP with a view from the Denizli-Aydın highway in Figure 1.3. Note that the pale short trees are olive trees.



Figure 1.3: The view of KZD-1 GEPP from Denizli-Aydın highway. The olive trees are short, shrub-like trees in pale forest green shade.

1.2 Contributions and Novelties

No existing studies are found in the open literature on hybridization of geothermal with biomass driven topping cycle. This research aims to contribute to GeoSmart outcomes by filling this gap while meeting the high flexibility needs of the power plant with the use of a topping sCO₂ cycle. Using sCO₂ cycle as a topping cycle supports flexible operation owing to smaller footprint and compact turbomachinery of sCO₂ cycles.

There are two main parts and contributions in this thesis. In biomass part (Chapter 3 and 4) well established methods are applied to a local biomass sample, olive residue. It is believed that the main value on these chapters lies in the professional development gained by the authoring student. On the other hand, the main novelty and contributions in this thesis are put forward in the hybridization part (Chapter 5 and 6).

In order to exploit the potential of coexistence of the two renewable energy resources,

OR samples collected from an olive oil factory nearby KZD-1 site. The characterization of the collected OR samples are done using preliminary experimental methods. The calorific value and the ultimate analysis of the studied OR samples are integrated to the hybrid power plant design. Recompression sCO₂ cycle is used as a topping cycle to hybridize the KZD-1 GEPP. Biomass sourced heat is used to power the topping sCO₂ cycle and increase the steam mass flow rate feeding the KZD-1 turbine which is normally operating at half capacity.

In the scope of this thesis, only the steady-state (nominal) case corresponding the maximum power output of the hybrid plant is investigated. Based on the feasibility of results for the steady state case, the future scenarios regarding the flexible operation can be explored as a future work.

1.3 Potential Impacts

Although the socio-economic and socio-environmental impacts of the proposed hybridization study are out of scope of this thesis, it is hoped that awareness for exploitation of two specific local renewable energy sources (olive residue and geothermal) in Southwest Anatolia can be increased with the introduction of more studies such as this thesis. Despite the high geothermal potential especially in Büyük Menderes Graben is known for more than 40 years, Turkey's geothermal boom can be considered relatively recent as country's installed geothermal capacity jumped from 100 MWe in 2010 to over 1000 MWe by 2020 [3]. As a local from the region, the author of this thesis would like to state that the public acceptance of geothermal in the region is very low. Similarly, the olive residue is not utilized in electricity generation in any form, rather used as a solid fuel for domestic heating purposes in the region. Therefore, combining two specific types of renewable energy resource with a next-generation power cycle is believed to form an initial block for regional development in sustainable, economically feasible and environmentally friendly manner.

CHAPTER 2

LITERATURE REVIEW

This chapter consists of three main sections. In Section 2.1, an overview on utilization of biomass in power generation is introduced where biomass combustion and characterization methods from the literature are also included. In Section 2.2, fundamentals of sCO₂ Brayton cycles and their types are explained. In Section 2.3 the selected state-of-the-art studies on sCO₂ cycles and hybridization of geothermal power plants are investigated.

2.1 Utilization of Biomass

2.1.1 Biomass Energy Conversion Technologies for Power Production

The energy conversion technologies from biomass resources can be classified under two general categories: 1) biological; and 2) thermochemical.

In biological technologies, biomass is converted into biogas, which is mainly composed of CH_4 and CO_2 , through four steps: 1) hydrolysis; 2) acidogenesis; 3) acetogenesis; and 4) methanogenesis [6]. Overall, these processes are referred to as anaerobic digestion and it is a widely used technology especially to produce biogas from the municipal solidwaste (MSW) collected mainly from households and municipal districts. The product, biogas, can be utilized in various power generation applications.

Thermochemical technologies, on the other hand, can be divided into two main categories; 1) gasification; and 2) combustion.

In gasification, the biomass feedstock is allowed to have incomplete combustion with presence of gasifying agents such as air, oxygen or steam so that the output gas, i.e. termed as syngas, has still combustion potential. The series of processes for gasification are: 1) drying; 2) pyrolysis; 3) oxidation; and 4) reduction. The produced syngas after gasification can be utilized in reciprocating engines, gas turbines or fuel cells [7].

In the case of combustion technologies, the biomass is allowed to burn with more than a stoichiometric amount of air in an exothermic chemical reaction, generally in a boiler where the products are CO_2 and H_2O along with the by-products such as ash, soot, NO_x , SO_x . The generated heat then can be used to drive a power block to generate electricity. Since the solid particle combustion characteristics of biomass is one of the primary focus of this thesis, the combustion processes is discussed in more detail within this section.

A summary of the biomass energy conversion technologies is presented in Figure 2.1. It should be noted that the employed processes to utilize the potential of biomass are mutually exclusive. For example, biochar, which is obtained through pyrolysis, can be used as an additive to an anaerobic digester to increase the biogas production efficiency [8], or the digestate, that is the by-product of anaerobic digestion, can be used as a feedstock for pyrolysis [9].

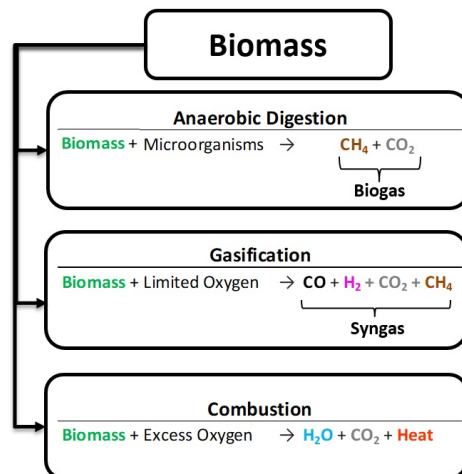
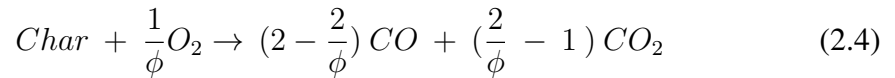
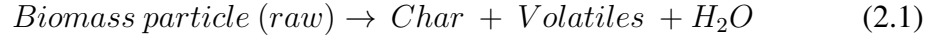


Figure 2.1: Biomass energy conversion technologies. Note that anaerobic digestion is a biological process whereas gasification and combustion are thermochemical processes.

2.1.2 Biomass Combustion

Biomass combustion, where it is considered as solid particle combustion within the context of this thesis, can be defined as the exothermic reaction between biomass and oxygen where mainly oxygen and water is formed at the end of the process. The following reactions broadly summarize this complex phenomenon [10].



Generally, the combustion of solid particles follows four distinctive steps: 1) drying; 2) devolatilization; 3) volatile combustion; and 4) char combustion. When the solid particle is first heated, it undergoes a drying stage where the desorption of gases (mainly water vapor) from the pores of the particle occurs. Then, it begins to decompose into char and volatile matter (Reaction Equation 2.1). As the volatiles are released from the particle, they interact with oxygen to form CO quickly, and after that CO_2 (Reaction Equations 2.2-2.3). These devolatilization and volatile combustion steps occur simultaneously and are very susceptible to conditions like the volatile content of the particle, size of the particle, environmental conditions, and heating rate [11]. After these steps, the remaining formation, which possesses the fixed carbon

content of the fuel, is called as char and starts to burn relatively slow compared to volatiles (Reaction Equations 2.4-2.6). It is important to have insight into how the steps regarding the volatiles develop because it forms a basis on char formation. Ultimately, the combustion duration of remaining char particles determines the size of the combustion chamber. It means the boiler design for a power plant at the macro level will depend on the char combustion kinetic parameters at the micro level. Finally, at the end of the char burning process, the remaining formation is called ash and it is mostly comprised of solid inorganic matter. These steps are also shown in Figure 2.2 as adapted from the work of Mando et. al. [12].

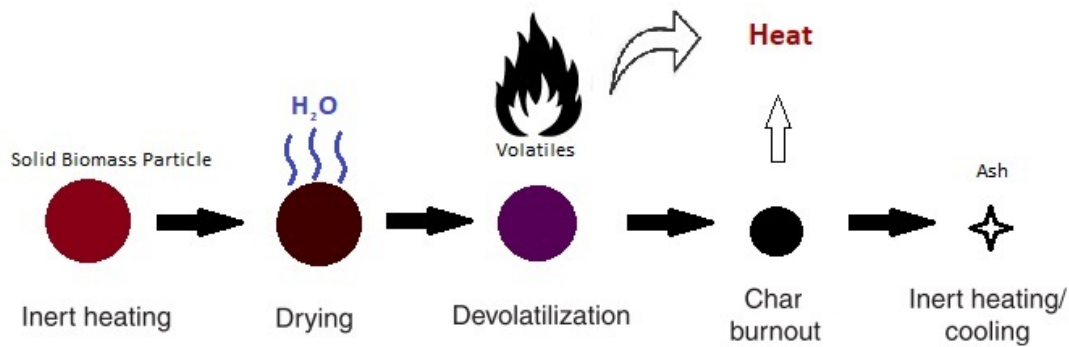


Figure 2.2: Steps of solid fuel combustion as adapted from Mando et. al. [12].

2.1.3 Thermogravimetric Analysis for Biomass Characterization

Thermogravimetric analysis (TGA) is an experimental method where the mass of the sample is monitored as a function of time and temperature with adjustable conditions such as heating rate, pressure, and gas composition. Due to its practicability and being an inexpensive instrument, it is a very common experimental device to conduct especially preliminary research on characteristics of fuel combustion. Even though the heating rates are relatively low compared to actual heating rates at the industrial boilers, the information obtained through TGA can be used for an initial evaluation of the combustion performance at the industrial scale and can easily be compared with other studies due to its high availability and repeatability [13].

The basic equipment for a TGA device is a precision balance and a furnace that can be programmed for a linear increase on temperature with time. The direct results from

TGA can be presented as:

- 1) weight vs temperature (or time) curve, referred as *Thermogravimetric (TG) curve*
- 2) rate of loss of weight vs temperature (or time) curve, referred as *Differential Thermogravimetric (DTG) curve*

where the units are generally weight percent (wt %) vs degrees Celsius, and percent change in weight per minute (%/min) vs degrees Celsius, respectively.

TG curve is simply a curve starting from 100 wt% and decreases down to 0 wt% with changing temperature (or time), while DTG curve is the derivative of TG curve. Presenting DTG curve along with TG curve can provide information about some features which cannot be easily interpreted only by TG curve such as spontaneous weight losses, which indicate burning of combustibles, or a shoulder before the peak which most likely represents adsorption of volatiles on the new solid phase [14].

Even without performing any kinetic modelling, these graphs are very useful to supply data on the characteristic temperatures of the fuel. These characteristic temperatures can be listed as: 1) peak temperature (T_P); 2) decomposition temperature (T_D); 3) burnout temperature (T_B); and 4) ignition temperature (T_{ig}). There is a widely used graphical method, i.e., method of characteristic temperatures, to determine these temperatures in the literature [15, 16, 17, 18]. They can be derived from TG and DTG curves as follows. First, TG and DTG curves must be ash-free basis, i.e., the TG curve should be normalized such that zero weight percent is reached at the end of the process, and DTG curve can be adjusted accordingly. Peak temperature (T_P) is defined as the temperature corresponding the maximum weight loss rate, and it can be found from the absolute minima of the DTG curve. Decomposition temperature (T_D) is defined as the temperature corresponding to percent weight loss rate of 1%/min after the moisture release process. Similarly, the burnout temperature (T_B) is also defined as the temperature corresponding to same rate at 1%/min at the end of the char burnout stage. Then, in order to find ignition temperature (T_{ig}), a tangent from the point on the TG curve corresponding the peak temperature is drawn. Another tangent from the point referring the end of the moisture release process on the TG curve is drawn, as well. The intersection of these two tangents corresponds the ignition temperature

of the fuel, and the interval between T_D and T_{ig} is named as decomposition stage. Similarly, the interval between T_{ig} and T_B is referred as combustion stage. These characteristic temperatures are depicted in Figure 2.3.

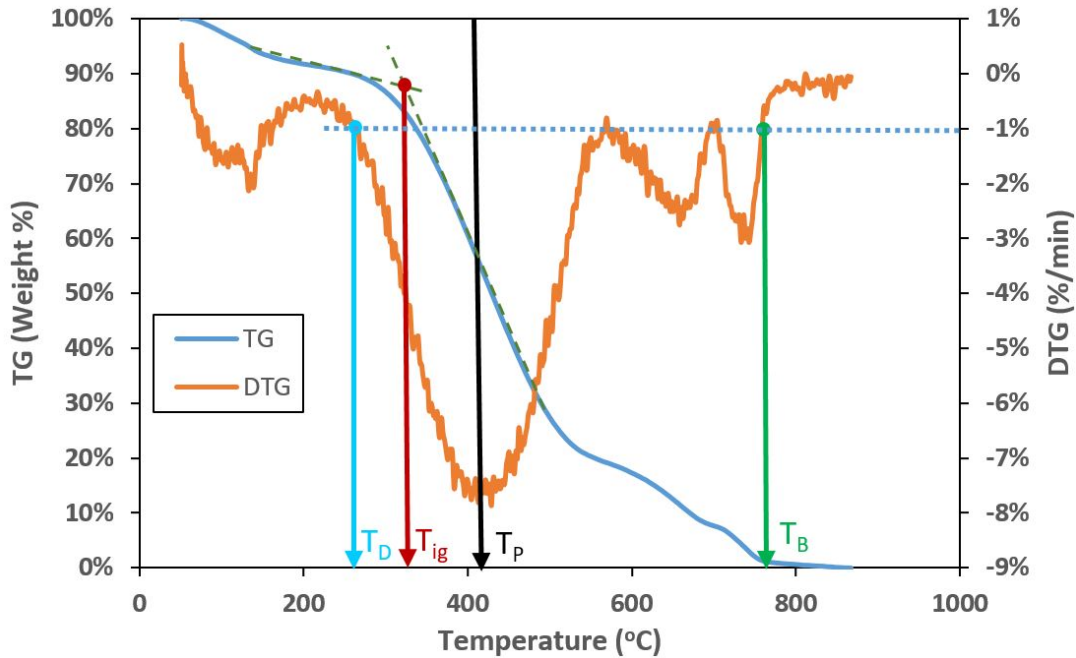


Figure 2.3: Illustration of characteristic temperatures.

It should be noted that, both TG and DTG are highly dependent on procedural details, e.g. sample weight, heating rate, crucible geometry, and condition whether the atmosphere is involved in reaction or not. For example, an inflection point appearing at a TG curve might change into a plateau (meaning no change in weight with respect to increasing temperature) for the same sample when the TGA is conducted with a slower heating rate. Thus, it can be concluded that TG/DTG curves are not unique even for the same sample.

2.1.4 Combustion Kinetics

Determining the reaction rates of the fuel in different combustion stages, mainly devolatilization and char combustion, is important to simulate what would happen in an industrial boiler. For this purpose, kinetic studies are conducted using TGA with isothermal and/or non-isothermal conditions. Within the scope of this thesis, only the

kinetics studies using non-isothermal TGA are investigated.

Kinetic analysis of solid biomass combustion is generally based on the rate equation [19]:

$$\frac{d\alpha}{dt} = k(T) f(\alpha) \quad (2.1)$$

where α is the conversion ratio, $d\alpha/dt$ is the conversion rate, k is the reaction rate, T is the temperature, and $f(\alpha)$ is the reaction model.

The temperature dependence of the reaction rate, $k(T)$, is usually represented by the first order Arrhenius equation:

$$k(T) = A e^{-E_a/RT} \quad (2.2)$$

where A (min^{-1}) is the pre-exponential factor and related to molecular collisions, E_a ($J mol^{-1}$) is the activation energy and interpreted as the minimum required energy to start the chemical reaction, R ($J K^{-1} mol^{-1}$) is the universal gas constant, and T (K) is the temperature.

There are several methods to determine the kinetic parameters, A and E_a , by using the results of TGA and Drop Tube Furnace (DTF) experiments. Similar to TGA, DTF is also an experimental method to study combustion and ignition characteristics of solid fuels where the heating rates are considerably higher (up to 10^5 °C/s), and therefore provides similar combustion conditions as the industrial boilers. However, since the study within this thesis constitutes a preliminary research about biomass characterization, kinetic studies using only non-isothermal TGA methods are going to be discussed.

Methods to determine kinetic parameters using TGA can be classified under two main categories: 1) model fitting methods; and 2) model free methods.

In model fitting methods, different reaction models are fit to portion of the TGA data that is being investigated, and the model having the best fit is selected to later determine the kinetic parameters A and E_a . In model free methods, there is no need to

define a reaction model beforehand to estimate the kinetic parameters. The conversion rate in Equation 2.1 is assumed to be constant, and thus the reaction rate only depends on the reaction temperature. These methods are simply postponing the need for an appropriate reaction model until an estimate of the kinetic parameters A and E_a is calculated [20]. Although more accurate estimations are possible with model free methods, several TGA experiments with different heat rates are required to be conducted. On the other hand, even a single experiment with a specific heat rate is enough to use a model fitting method, which is also the case within this thesis.

The first effort to use TGA data for kinetic parameters appears to be made by van Krevelen et. al. [21]. Introducing a graphical method to obtain the order of the reaction, they derived an approximate equation to show that the primary decomposition of their coal sample is first order. Historically, model free methods such as Kissinger [22], Flynn–Wall–Ozawa (FWO) [23, 24], Vyazovkin [25], Tang [26]; and model fitting methods such as Coats Redfern [14], Kennedy and Clark [27] are introduced concurrently. Among these methods, the most commonly used one in the kinetic analysis of thermal decomposition of coal and biomass is Coats and Redfern Method (CRM) which is also used in this thesis.

It is difficult to separate the kinetic studies on coal and biomass, in fact, in many cases they are studied together, either in a comparative manner [28, 29, 30] or their blends are being investigated [31, 32, 33].

Liu et. al. [32] studied kinetic parameters and combustion reaction mechanism of two types of biomass, namely beetroot and switchgrass, and their blends with bituminous coal using non-isothermal TGA. They combined model fitting and model free methods, i.e. CRM and FWO and tested the accuracy of it. It is found out that there is considerable difference in terms of kinetic parameters between biomass and coal, and therefore blending ratios have large impact on the apparent activation energies of the samples. They observed 3-4 peaks for studied biomass and blended biomass-coal samples, and the calculated activation energies of these samples for so-called pre-peak and post-peak regions of TG curves range from 100 to 239 kJ/mol, and from 44 to 133 kJ/mol, respectively.

Lopez-Gonzalez [34] analyzed different biomass samples such as black spruce, wil-

low, common reed, reed canary grass, and switchgrass using TGA and compared their combustion behaviours with defining a term, i.e. combustion characteristic factor (CCF), which can be used as an indicator for their burning profiles. The combustion process was divided into two main stages, namely devolatilization and char oxidation, and it is found out that willow and reed canary grass demonstrate best performance, with activation energies ranging from 91 to 112 kJ/mol and 81 to 98 kJ/mol for the respective samples at different stages of combustion.

Magalgaes et. al. [28] investigated the combustion behaviours of two lignites from Tunçbilek and Soma regions, and one olive residue from Balıkesir region. In addition to combustion kinetic parameters that are defined using CRM at different heating rates, a performance indicator named combustibility index is introduced to perform comparison between the fuels. The major findings regarding especially the OR are: 1) The burnout temperature of OR is always lower than that of lignites, and shifts to higher temperatures with increasing heating rate. 2) Combustibility index of OR is at least fivefold those of lignites, where the activation energy of OR is around 40-45 kJ/mol for the major stage of combustion at different heating rates. 3) The major stage of combustion for OR is controlled kinetically by a first order mechanism. 4) There observed a secondary combustion stage uniquely for OR, where the combustion is reported to be diffusionally controlled. For this stage, the apparent activation energy is around 10 kJ/mol, regardless of the heating rate.

There are studies on combustion characteristics of a broad range of biomass samples. Alvarez et. al. [35] provided a wide database for 28 biomass samples, including olive stone, extracted olive pomace and olive tree pruning, where kinetic parameters are determined using both model free (FWO and Kissinger) and model fitting (CRM) methods. It is suggested that employed model free methods (FWO and Kissinger) are not suitable to determine the kinetic parameters of biomass combustion since the assumptions for these methods are not accomplished in the full range of the combustion process. Kok and Ozgur [36] conducted a study on 3 biomass species, namely miscanthus, poplar wood, and rice husk in a similar manner but using model free methods only. In both studies, experiments are performed with different heat rates of 5, 10, 15 and 20 °C/min and the combustion was divided into two stages and kinetic parameters supplied accordingly. The apparent activation energies for extracted

olive pomace are reported as 32 and 146 kJ/mol at respective stage of combustion at [35]. More specifically on olive oil production chain residues, Buratti et. al. [37] studied olive tree pruning, two phase OP, three phase OP and their mixtures under combustion condition using non-isothermal TGA. The combustion stage is defined under two stages, namely devolatilization and char combustion as previous studies, and these stages are attributed to the decomposition of hemicellulose-cellulose and lignin, respectively. Model free methods, i.e. FWO and Vyazovkin, are employed to determine the kinetic parameters, however, the apparent activation energies were calculated globally as aggregated values, not for the single combustion stages. Therefore found average values for pure samples and their blends lies in the range of 80-90 kJ/mol.

2.2 sCO₂ Power Cycles

The history of supercritical carbon dioxide (sCO₂) power cycles goes back to late sixties where their promising thermodynamic performances are theoretically introduced [38]. However, the initial interest to sCO₂ cycles is diminished as the gas turbines became increasingly popular. Recently, there has been a global interest in sCO₂ power cycles considering the number of published scientific articles in the last decade since the unique properties of CO₂ offer intrinsic benefits over steam as a working fluid in closed loop power cycles. Some of the advantages of sCO₂ cycles can be listed as [39]:

- reduced footprint and size due to CO₂ being denser than steam
- better capex utilization due to compact turbomachinery
- flexible operation capability since it can be ramped up and down more rapidly
- better response to transient load

In addition to these advantages, sCO₂ cycles can offer equivalent or even better thermodynamical efficiencies compared to their steam Rankine counterparts. A rough but informative map for area of application of sCO₂ cycles is provided in Figure 2.4 as adapted from a report of STEP DEMO Project [39]. The improvement in the efficiency particularly becomes more apparent at higher heat source temperatures, thus sCO₂ cycles are mostly popular in CSP area. However, superior first law efficiencies compared to steam Rankine cycles are also proven both experimentally and numerically for lower temperatures, e.g. 527 °C [40, 41]. Thus, sCO₂ cycles can be considered as an option for biomass combustion applications, especially when flexible operation is desired.

To date, there has not been full-scale commercial demonstration for sCO₂ cycles as the existing studies are limited to laboratory-scale test setups under 1 MWe [42, 43, 44]. A \$119 million USD project named STEP DEMO, lead by GTI, GE, US Department of Energy, National Energy Technology Laboratory is one of the leading projects in this area, and aims to demonstrate a pilot power plant test facility of 10 MWe in TX, US by 2022 by increasing the TRL from 3 to 7[39].

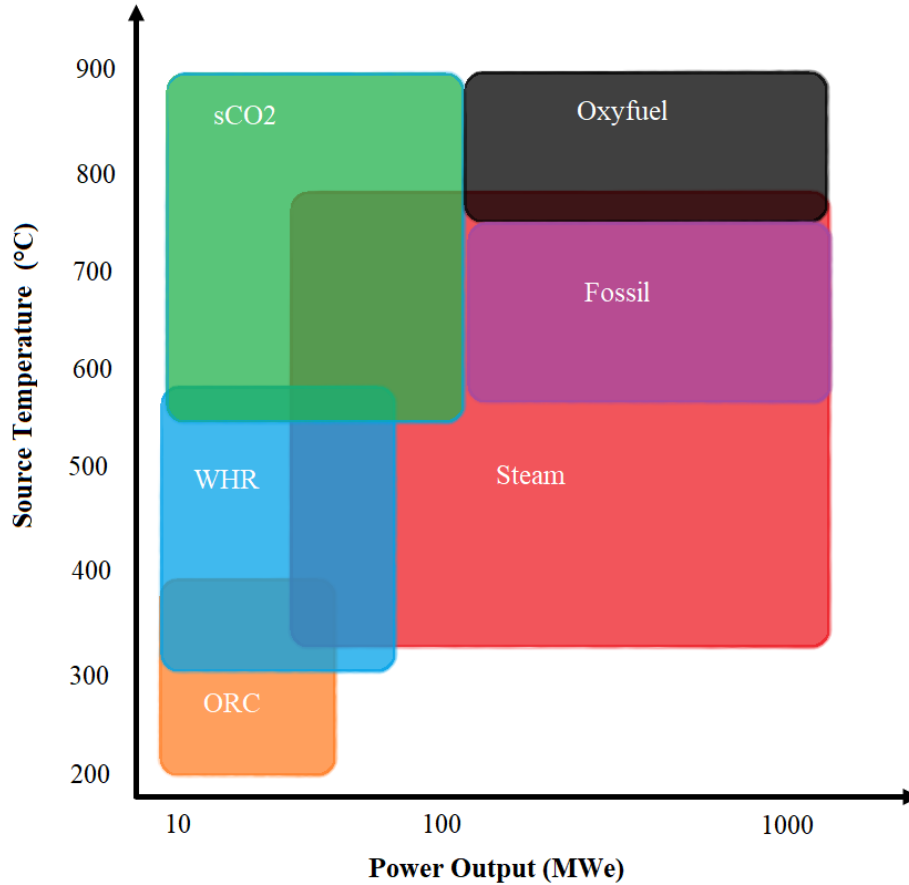


Figure 2.4: sCO₂ Application Map [39]. Note: sCO₂ – Supercritical CO₂; ORC – Organic Rankine Cycle; WHR – Waste Heat Recovery.

Although sCO₂ cycles refer to cycles using CO₂ at fully supercritical state, it is worth to mention that the difference between transcritical and supercritical CO₂ cycles is not very significant as the naming depends on how the heat rejection is performed, i.e. by cooler for supercritical and condenser for transcritical CO₂ (tCO₂). Similarly, the prefix Rankine or Brayton depends on the type of heat rejection from the cycle, i.e. cooler for Brayton and condenser for Rankine. The particular compression device also depends on the cycle, i.e. compressor for fully supercritical, and pump for transcritical CO₂ cycles.

Most of the sCO₂ cycles that are being studied by the researchers today are derived from the initial works of Angelino and Feher from the late 60s [45, 46]. Several transcritical configurations are introduced by Angelino with the main argument that the expansion of carbon dioxide at its supercritical conditions can reach the same or even

higher efficiencies than steam turbines while keeping the simplicity of closed loop gas turbines. In this context, Angelino proposed condensing transcritical cycles with recuperation layouts aiming to reduce the irreversibilities occurring at the recuperators. These layouts are considered as the forerunners of the modern Recompression (RC) cycle [38]. The shortcoming of this cycle is that turbine exhaust pressure is imposed by condenser pressure (or vice versa). In order to make these two parameters independent from each other, Angelino proposed another configuration by using additional compressor, and this layout eventually evolves into the modern Partial cooling (PC) cycle. Similarly to Angelino, Feher studied the alternative configurations of CO_2 cycles but in purely supercritical conditions. Both authors claim that supercritical carbon dioxide cycles offer potentially higher efficiencies with respect to Rankine cycles at temperatures higher than 600 °C while retaining much smaller footprint.

2.2.1 sCO₂ Cycle Configurations

The types of sCO₂ cycles great varies in the literature. More than 40 novel configuration for standalone sCO₂ cycles are reported in a comprehensive review study by Crespi et. al [38]. The maximum temperature and the thermal efficiency for the reported configurations range from 72 to 1300 °C, and 6.4 to 63 %, respectively, as sCO₂ cycles are used in a wide range of applications from WHR to oxy-combustion. Among these configurations, three sCO₂ cycles are selected as candidates for hybridization with geothermal considering the simplicity, maturity, popularity (based on the number of published articles), and their synergistic thermodynamic features with geothermal. These three layouts are commonly named in the literature as simple recuperated, recompression and partial cooling sCO₂ cycles and are explained in more detail in this subsection. A broad overview of these cycles are provided in Table 2.1 as adapted from the review study of Crespi et. al. [38].

Table 2.1: Overview of the selected standalone sCO₂ cycles [38]. P (bar), T (°C).

Cycle Name	P_{\min}	T_{\min}	P_{\max}	T_{\max}	η_{th}	Number of reported studies
Simple Recuperated	73.5	32	250	550	40.4%	34
Recompression	78	32	250	550	46.5%	47
Partial Cooling	50	32	250	550	46.1%	14

2.2.1.1 Simple Recuperated sCO₂ Cycle

Simple Recuperated sCO₂ cycle is a simple Brayton cycle utilizing CO₂ in fully supercritical state using single recuperator. The cycle is designed such that the compression work is minimized by allowing the compression to occur very close to critical point of CO₂. This phenomenon is not only unique to simple recuperated sCO₂ cycle but also observed in all of the sCO₂ cycles to exploit the thermophysical properties of CO₂ in supercritical region close to its critical point. Note that CO₂ behaves as a supercritical fluid above temperature of 31 °C and pressure of 73.8 bar. Ultimately, comparatively high thermal efficiencies are achieved when the greatly reduced compression work is combined with the recuperative nature of the cycle and the low pressure ratio (<4) [38]. The layout of the simple recuperated sCO₂ cycle is provided in Figure 2.5.

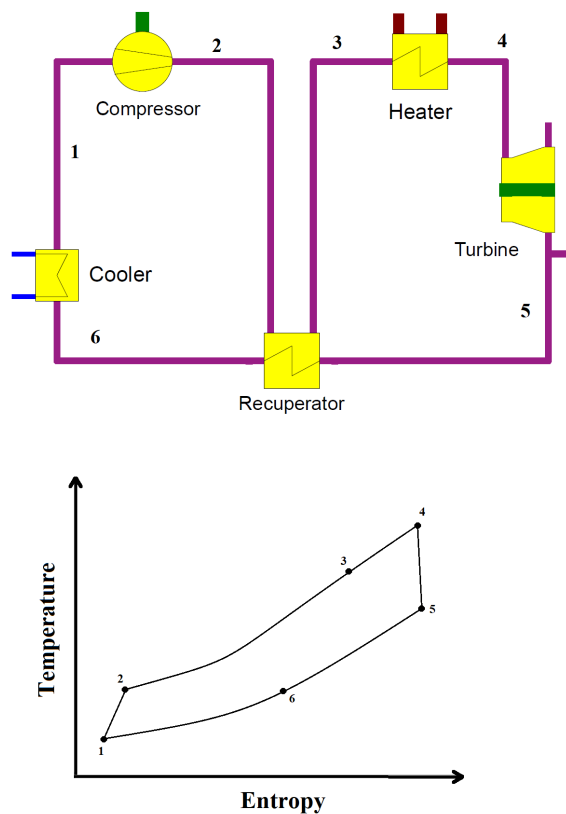


Figure 2.5: General layout and T-s diagram of the simple recuperated sCO₂ cycle. The layout is generated using the software EBSILON®Professional.

In contrary to its name and layout, the simple recuperated sCO₂ cycle is not completely straightforward as a Brayton cycle. The CO₂ as a fluid exhibits very unique properties near its critical state. Properties of CO₂ such as density, thermal conductivity, and dynamic viscosity vary greatly in the vicinity of the critical point, but specifically, the isobaric heat capacity (c_p) presents substantial peak around the critical temperature and pressure as it is shown in Figure 2.6. Although the sharpness of the peak is decreased by the increasing pressure, this non-linear behaviour causes an intrinsic problem for sCO₂ cycles, i.e. pinch point problem. Pinch point can be defined as the minimum temperature difference between the hot and cold streams at any location along the heat exchanger whose negative value implies non-physical solution while its increasing positive value ensures more realistic heat exchange size. Note that the hot side outlet of the recuperator in Figure 2.5 is to be cooled down through the cooler to a state in the vicinity of the critical point so that the compression work is minimized to achieve superior thermal efficiencies. Therefore this specific heat exchanger (Cooler in Figure 2.5) is subject to "the pinch point problem". Despite being less likely, the pinch point problem may also occur at the other heat exchanger, namely recuperator, since the hot side outlet can be as low as 45 °C in some applications [47]. Under no circumstances, the pinch point can be a negative value. Therefore, the effectiveness of the heat exchanger should be adjusted to ensure the local temperature difference between two streams is always positive, otherwise the solution becomes superficial.

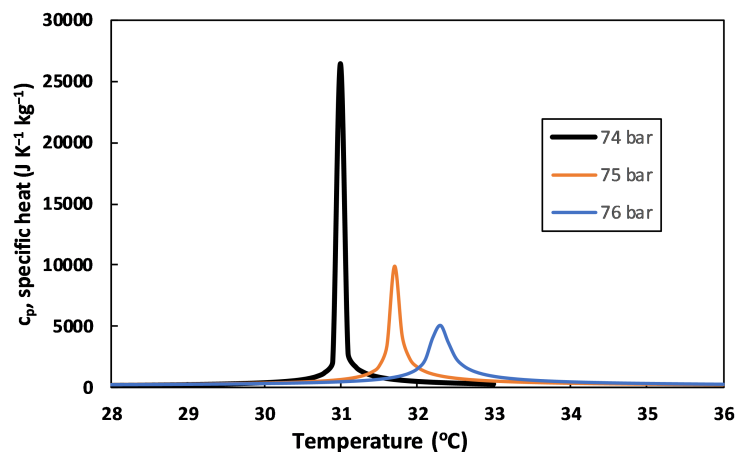


Figure 2.6: Isobaric specific heat of CO₂ with varying temperature at different supercritical pressures. The values are obtained using CoolProp add-in in MS Excel.

2.2.1.2 Recompression sCO₂ Cycle

Recompression (RC) sCO₂ cycle is the evolved version of the works of Angelino, and has clear connections with Feher's work [45, 46, 38]. Due to the additional compressor that is located parallel to the main compressor, the cycle is named as recompression cycle. After the low temperature recuperator, the flow is splitted into two for the compression processes. Therefore, sometimes the cycle is also called as part-flow cycle in the literature. Note that there are two recuperators in RC sCO₂ cycle as it is shown in Figure 2.7, making it highly recuperative.

As it can be observed from Figure 2.7, the hot side outlet of the low temperature recuperator is splitted into two streams. The first stream goes into the cooler where the temperature is decreased to a value close to the critical temperature. The other stream is not cooled but instead directly compressed in the recompressor. There are several major advantages of this configuration. Firstly and most importantly, the famous pinch point problem in the cooler can be overcome by adjusting the part-flow going into the recompressor. Secondly, since the recuperation is divided into two stages, the likelihood of pinch point problem at the recuperators is confined only to the low temperature recuperator. Thirdly, the thermal duty of the cooler is decreased, meaning that the footprint of the equipment is also reduced. Lastly, more than 5% increase in the thermal efficiency is achieved at the same turbine inlet temperature compared to simple recuperated cycle (Table 2.1) since better heat recovery from the turbine exhaust is possible with two recuperators. Overall, the RC cycle is the most extensively researched cycle in the literature due to being relatively simple while retaining good thermal efficiencies as presented in Table 2.1.

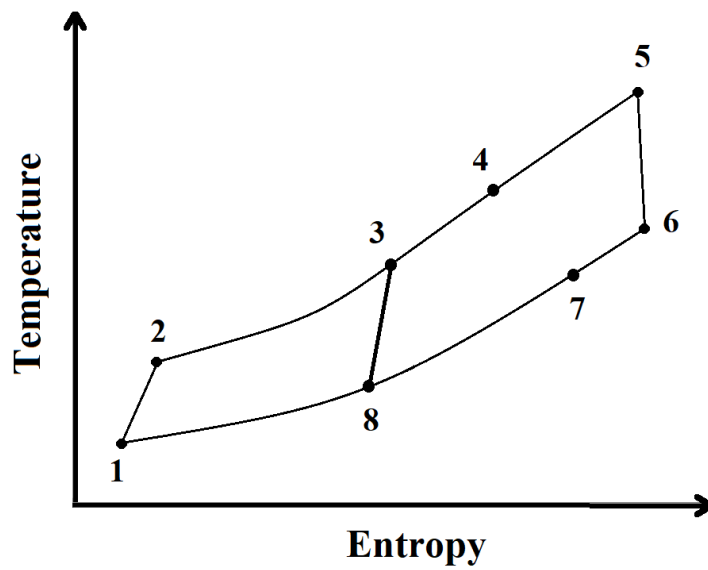
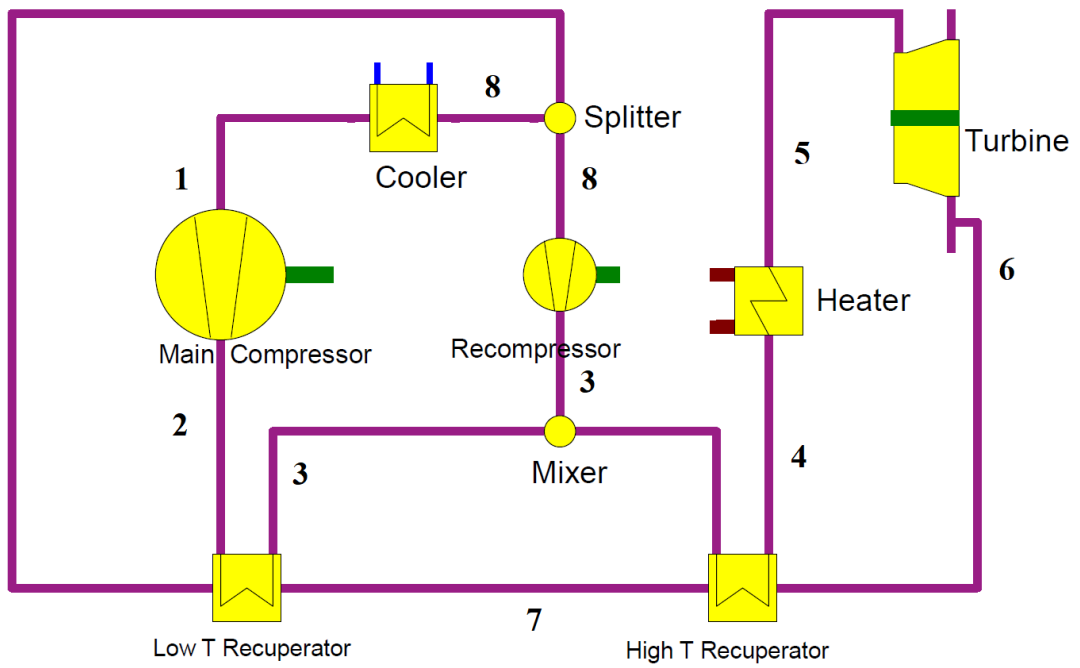


Figure 2.7: General layout and T-s diagram of the Recompression sCO₂ cycle. The layout is generated using the software EBSILON®Professional.

2.2.1.3 Partial Cooling sCO₂ Cycle

Partial Cooling (PC) sCO₂ cycle is the modified version of the RC cycle where additional compressor and cooler is placed before the main flow is splitted. Due to the additional compressor and cooler, a degree of freedom is obtained for the compressor inlet pressure which in turn makes the overall thermal efficiency of the cycle less dependant on the optimum pressure ratio. Higher specific work compared to RC cycle is achieved at the cost of more complexity [48]. The general layout of this cycle is provided in Figure 2.8.

The strenghts and weaknesses of the analysed sCO₂ cycles are provided in Table 2.2 as adapted from Crespi et. al [38]. Although the simple recuperated cycle is the most simplest cycle and potentially will have earlier market entry compared to other cycles, its potential for hybridization with other cycles is not favorable since it is highly susceptible to the intrinsic problem of sCO₂ cycles, i.e. pinch point problem. This problem especially becomes prominent if the waste heat from a topping sCO₂ cycle (by means of the cooler) is desired to be used in a bottoming cycle. Considering its maturity, relatively simpler complexity, and high thermal efficiency, RC sCO₂ cycle is chosen for hybridization with geothermal within this thesis.

Table 2.2: Strenghts and weaknesses of the analyzed sCO₂ cycles [38].

Cycle Name	Strenghts	Weaknesses
Simple Recuperated	Simple layout	Pinch point problem
	Availability of experimental facilities	Moderate thermal efficiency
Recompression	High thermal efficiency	Complex recuperator design
	Pinch point problem resolved	
	Smaller cooler	
	Availability of experimental facilities	
Partial Cooling	High thermal efficiency	Complex layout
	High specific work	
	Low sensitivity to PR deviations	

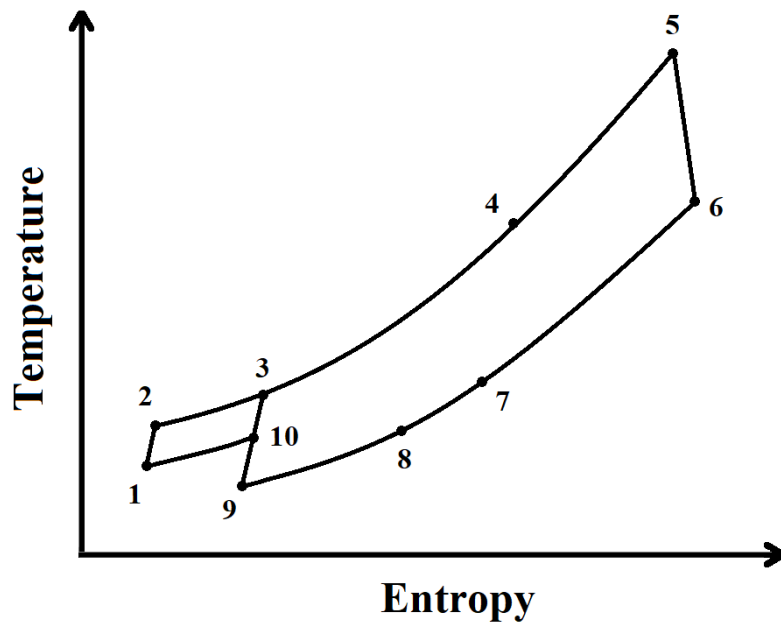
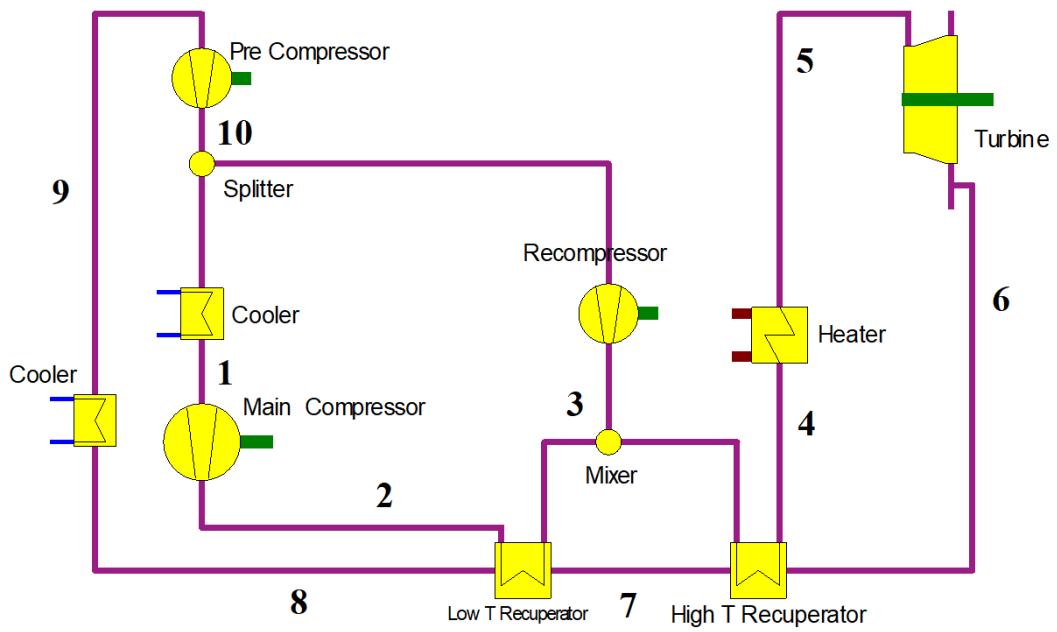


Figure 2.8: General layout and T-s diagram of the Partial Cooling sCO₂ cycle. The layout is generated using the software EBSILON®Professional.

2.3 Selected studies on sCO₂ Cycles and Hybridization of Geothermal

The efforts that are put in this thesis to hybridize geothermal with biomass originally stem from the study of Bonyadi et. al. [49]. To date, the study of Bonyadi et. al. is the first and the only study in the literature that hybridizes geothermal electric power plant (GEPP) by using a solar topping power cycle. It is worth to mention the work of Bonyadi et. al. [49] since the idea of using a sCO₂ cycle to hybridize geothermal in this thesis is inspired from it. In their study, Bonyadi et. al. added a solar powered steam Rankine cycle to a hypothetical existing Organic Rankine cycle (ORC) GEPP without requiring any modification for bottoming ORC. The solar topping cycle is coupled to the ORC such that the waste heat from the topping cycle is utilized in the ORC. Different operational scenarios are suggested with the intention of preserving the health of the geothermal resource. This conservation is performed in their study as more waste heat from the solar topping cycle is recovered during day time when direct insolation is available, the energy harvest from the geothermal brine to ORC is decreased, and replaced with more solar sourced heat. Hybridization of geothermal with solar thermal in this manner is especially synergistic since the thermal efficiencies of GEPPs are very susceptible to weather temperature, and thus drops significantly during hot summer months when solar availability at highest. Ultimately, their design has a solar efficiency of 12.2% and consumes up to 17% less brine than an equivalent stand-alone geothermal plant. The general layout of their hybrid power plant is supplied in Figure 2.8 by permission of the authors.

Another valuable study on hybridization of double flash type geothermal power plant is done by McTigue et. al. [50]. In their study, an existing double flash GEPP operating in China Lake, California (where both good geothermal and solar resources coexist) is retrofitted with solar thermal to increase the power generation. It is aimed to increase the power output of a turbine operating at 75% of its rated output (22.5 MW) to 100% its rated output (30 MW) by integrating array of Parabolic Trough (PT) collectors. In order to decide the optimum location for solar heat addition to double flash geothermal power plant, parametric analysis on thermal efficiency is performed for 4 different locations, namely before the re-injection of saturated liquid, after the condenser, before the first flash tank-separator, and after the first flash tank-separator.

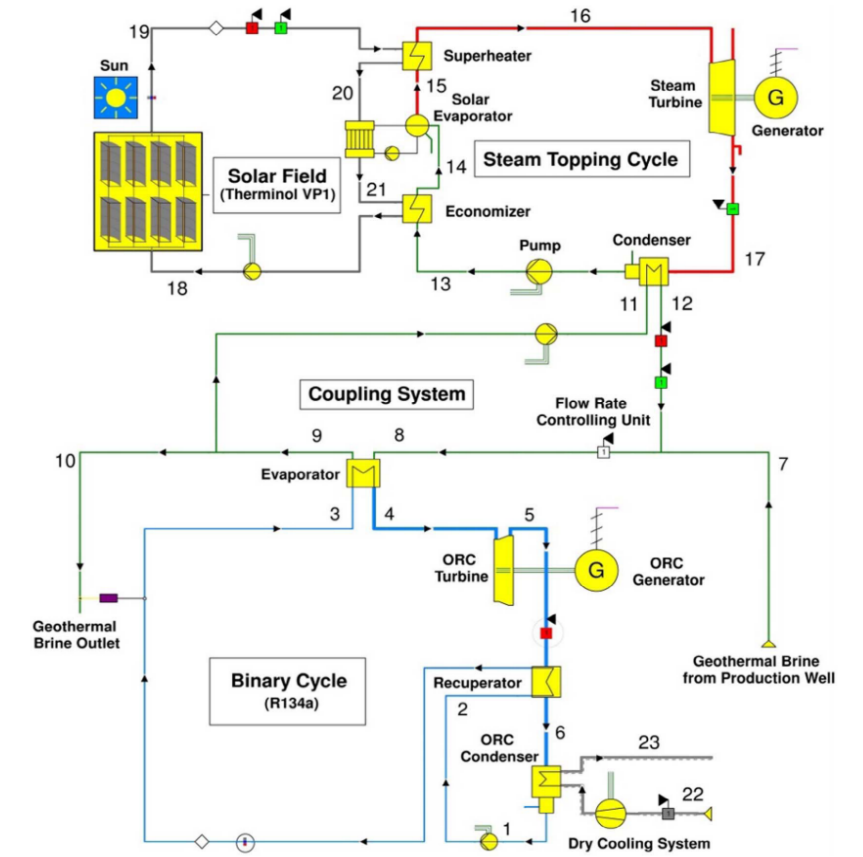


Figure 2.9: Layout of the solar-geothermal hybrid power plant by Bonyadi et. al.[49]

The optimum location for heat addition is found as the point after the first flash tank-separator. Thermal energy storage by means of storage fluid DPO (eutectic mixture of diphenyl oxide and biphenyl) is added to the hybrid configuration to increase the flexibility. Levelized Cost of Electricity (LCoE) with 3 hours of thermal storage is calculated as 0.08 \$/kWh, which is lower than equivalent conventional standalone CSP and battery integrated PV systems. Addition of a topping cycle for such an hybrid configuration is also suggested by the authors as potential future work with the intention of achieving greater thermal efficiencies.

Unlike the hybrid geothermal-solar systems, the interest for hybrid geothermal-biomass systems are limited in the literature. The state-of-the-art studies are limited to those using biomass sourced heat to supplement the operating enthalpy of low temperature geothermal [51], using biomass to compensate for the off-design conditions of geothermal power plant (such as efficiency drop due to high weather temperature)

[52], and multigeneration biogas-geothermal systems [53]. Similarly on the industrial side, when the coexistence of geothermal and agricultural lands or forestries are present, either biomass or geothermal is used to boost the performance of the other. For instance, a dry steam geothermal power plant in Cordia, Italy having a rated output of 20 MWe (but generating 13.8 MWe) is redesigned to accommodate a biomass furnace in order to superheat the geothermal steam. An additional 5.4 MWe gain is obtained from the biomass combustion. In another example from New Zealand, a wood waste biomass power plant operating in close proximity to forest plantations is supplemented by a geothermal preheat [54].

In addition to pinch-point problem, the sCO₂ cycles have another intrinsic problem regarding the heat addition to the cycle. It should be noted that even the most primitive configuration for a sCO₂ cycle is called as simple recuperated cycle. Due to their highly recuperative characteristics, the external heat addition to sCO₂ cycles is done at high temperature interval as it can be observed from Figures 2.7 and 2.8. The heat addition to these cycles can be observed between points 4 and 5 on T-s diagrams. In order to overcome this limitation, the sCO₂ cycles are often combined with bottoming ORC cycles operating at low temperatures [55, 56, 57, 58] or utilized in cascaded manner as sCO₂-sCO₂ and sCO₂-tCO₂ cycles [59, 60, 61]. Alternatively for coal powered sCO₂ cycles, advanced boiler/heater designs are introduced to fully exploit the heat available in the flue gas within the cycle at the cost of having more complex layouts [62, 63].

Motivated for the problem of a biomass powered sCO₂ cycle design, Manente and Lazzaretto introduced an innovative cascaded sCO₂ cycle design using woody biomass as a fuel [64]. In their study, two different cascaded sCO₂ cycles (Recompression sCO₂ - Simple Recuperated sCO₂ and Simple Recuperated sCO₂ - Simple Recuperated sCO₂) are investigated along with four different boiler arrangements, which are counter-current radiant-convective boiler, co-current radiant-convective boiler, counter-current convective boiler, and co-current convective boiler. It should be noted that in contrast to their names suggest, these heat addition units are not literally boilers as CO₂ is in fully supercritical state, and thus not changing phase. Among the analyzed configurations, Recompression sCO₂ - Simple Recuperated sCO₂ cascaded cycle coupled with a counter-current radiative-convective boiler demonstrates the best

performance in terms of biomass to electricity conversion efficiency, i.e. 36% for turbine inlet temperature of 550 °C. It is found that more heat is transferred from flue gas of the boiler to the bottoming cycle if a convective boiler is used, and accounts for lower thermal efficiencies for convective boiler configurations. When the air-preheating unit is removed, the thermal efficiency range drops from 30-36 % to 28-34%.

The pioneer and relatively the most respected study on RC sCO₂ cycles is done by Utamura [40]. In his thermodynamic analysis on a RC sCO₂ cycle, he demonstrated that thermal efficiency of 45% under maximum operating conditions of 20 MPa (200 bar) and 800 K (526.85 °C) is achievable. The suggested RC cycle configuration in his study also overcomes the pinch-point problem that is common in simple recuperated sCO₂ cycles accounting for mediocre thermal efficiencies , i.e. 39% for the same operating conditions. However, it is stated by the author that the high thermal efficiencies up to 45% are only possible if state-of-the-art heat exchangers with high temperature effectiveness (98%) are used as recuperators. Otherwise, the thermal efficiency drops to 40% for recuperators with 85% effectiveness. Coincidentally, Utamura designed bench scale novel microchannel heat exchangers reaching this high effectiveness value (98%) which later is used to verify his numerical findings with a bench scale sCO₂ cycle experiment [65, 41]. In order to optimize his model, Utamura conducted parametric analysis on key parameters such as the turbine expansion ratio and part-flow ratio, i.e. the ratio of the mass flow rate directed to main compressor after the flow is splitted. The design values giving the optimum results in his study are presented at Table 2.3, which is used as benchmark for verification in Chapter 5. The name of the components in Table 2.3 are modified to be consisted with the RC cycle presented at Figure 2.7.

Table 2.3: Design conditions of RC sCO₂ cycle by Utamura [40] as adapted to Figure 2.7.

Equipment	Parameter	Unit	Value
Compressors	Inlet temperature	31.85	°C
	Adiabatic efficiency	90	%
Turbine	Inlet temperature	526.85	°C
	Inlet pressure	200	bar
	Adiabatic efficiency	93	%
	Expansion ratio	2.51	-
Recuperators	Effectiveness	98	%
	Pressure drop ratio hot side	0.4	%
	Pressure drop ratio cold side	1.2	%
Heater	Pressure drop ratio	1.2	%
Cooler	Pressure drop ratio	1	%
Splitter	Part-flow ratio	0.68	-

CHAPTER 3

MATERIALS AND METHODS FOR BIOMASS CHARACTERIZATION

In this chapter, background of the obtained OR samples, used materials for the experimental study, and mathematical background for the combustion kinetics of the biomass samples are described.

3.1 Background of the Obtained Biomass

The studied olive residue (OR) samples are obtained from a olive oil factory named Altınvadi Zeytinyağı Fabrikası Küp Yağ San. Ve Tic. Aş, located in Karacasu province of Aydın. The samples are by-product of olive oil harvest season of 2018. Since different olive oil production methods exist, it is worth to mention these olive oil production methods to provide a clear background for the studied fuel samples.

Olive oil production includes several processes such as olive washing, grinding, beating, and the extraction. While the first three processes are more or less same for the different methods, it is worth noting that the most important process is the extraction since the type and amount of the waste depends on it.

The extraction methods can be divided under two main category: 1) traditional pressing, 2) centrifugation. Although the traditional pressing is relatively an obsolete technology and been taken over by centrifugation methods in the last decades, it is still used extensively especially in some countries such as Portugal. In order to provide more insight, a quantitative comparison of the methods from a 2006 study for selected European countries are presented at Figure 3.1 [66].

Traditional pressing is the most primitive method to extract oil, changed slightly over

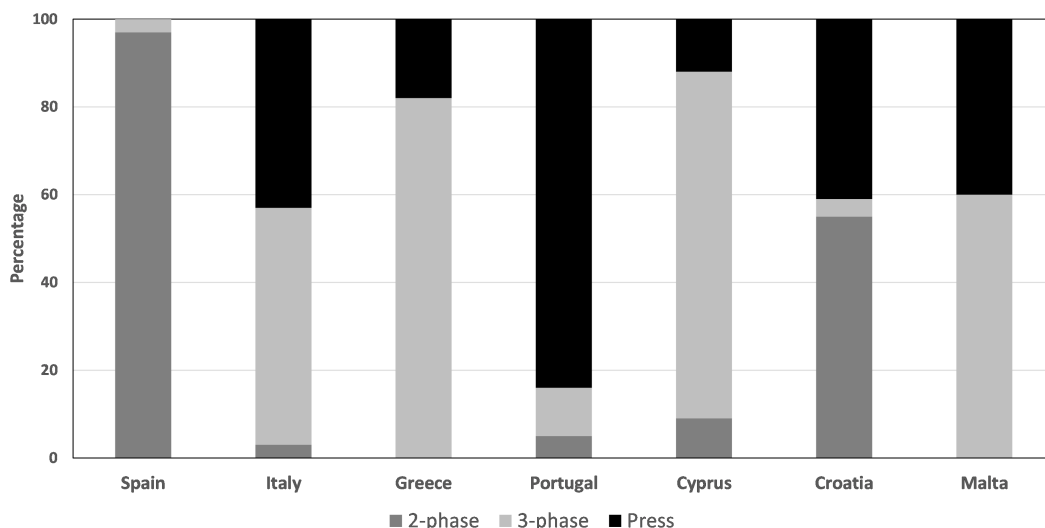


Figure 3.1: Distribution of olive oil extraction technologies for European countries [66]. Note that 2-phase and 3-phase are centrifugation methods.

the centuries.. After the olives are washed and grinded (generally via using “ancient” stone mills) , the grinded mud-like mixture are packed into a sort of felt packs, where the liquid oil-wastewater mixture is allowed to leak through the pores of the packs by itself. Then these bags are placed under a press for further and forced leakage. At the end, most of the emulsion will be drawn out of bags, leaving a solid waste with a trace amount of oil inside the packs. This solid leftover is called as olive residue, olive husk or olive pomace, and these terms are used interchangeably. Finally the leaked olive oil-wastewater mixture is sent to a decantation device where the oil is extracted, leaving a black colored wastewater as the final waste.

The centrifugation methods can also be divided under two category: 1) 2-phase systems, 2) 3-phase systems. In these systems, the grinded mud-like mixture is directly put into a 2-phase or 3-phase centrifugation device (allowed to mixed further with hot water if it is a 3-phase system) and a thick paste residue is extracted at the end of the centrifugation for 2-phase systems where a relatively dry residue is obtained in 3-phase systems . The remaining mixture is then subject to processes such as oil washing and oil recovery, where the olive oil is extracted as a final product. A schematic for all of the discussed methods is provided in Figure 3.2 [67].

The studied OR samples are obtained from a small-scale olive oil factory using tradi-

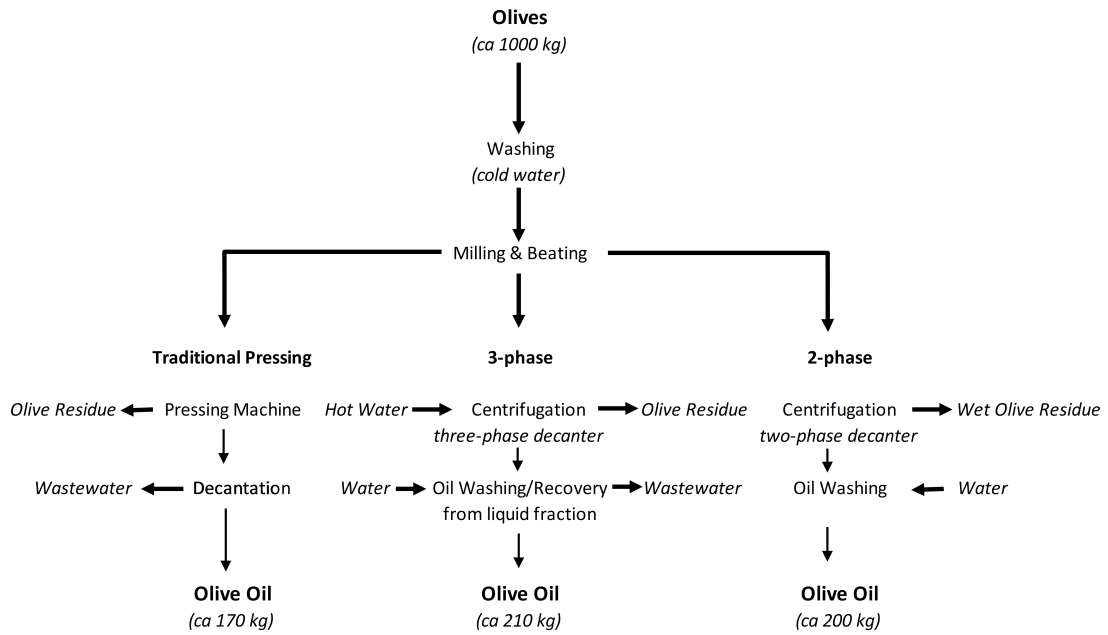


Figure 3.2: Overview of oil extraction methods [67]. Note that 2-phase and 3-phase are centrifugation methods.

tional pressing as the extraction method. Considering the final amounts of extracted oil between these three methods, it is likely that amount of extractable oil trapped in the OR obtained by traditional pressing is greater than those ORs obtained by other two methods.

3.2 Fuel Preparation

Initially, obtained OR samples are kept overnight in the muffle furnace at 105 °C to determine the excess moisture content of the as received fuel. The used muffle furnace (Figure 3.3) is located at Clean Combustion Technology Laboratory (CCTL) of Middle East Technical University (METU) Mechanical Engineering Department. This initial drying process to remove excess moisture is required prior to grinding, since, otherwise the moist fuel ends up sticking the walls of the grinder, and making the grinding process more difficult. Five samples with nominal masses of 1 gram are prepared and the average result of the excess moisture content of as received fuel is presented at Table 3.1. Although the fuel can still retrieve a trace amount of moisture after the initial drying, avoiding the effect of excess moisture on the further



Figure 3.3: Muffle furnace at CCTL METU



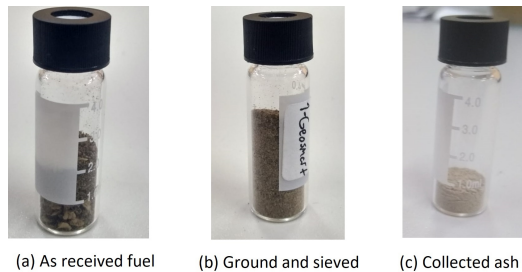
Figure 3.4: Ring mill grinder at Mineral Processing Laboratory METU

experiments is important.

After the removal of excess moisture, the samples are grounded using ring mill grinder (Figure 3.4) located at Mineral Processing Laboratory of METU Mining Engineering Department. The ground samples are sieved using Retsch sieve sets and the Retsch sieve shaker located in METU Mining Engineering (Figure 3.5). The prepared samples are stored in glass vials between particle size range of 106-125 μm .



Figure 3.5: Sieves and shaker.



(a) As received fuel (b) Ground and sieved (c) Collected ash

Figure 3.6: Studied OR in glass veils.

3.3 Experiments

After drying, grinding, sieving, and storing, further experiments can be done using the prepared samples. In order to conduct proximate analysis, a TGA experiment is done using Perkin Elmer Pyris STA 4000 thermogravimetric analyzer (Figure 3.7) located at Composite Material Characterization Laboratory of METU Center for Wind Energy Research (RÜZGEM). The thermogravimetric analyzer is programmed to follow the steps indicated below:

(in the presence of nitrogen atmosphere)

- 1) Heat the sample from 25 °C to 105 °C at 10 °C/min
- 2) Hold for 5 minutes at 105 °C
- 3) Heat from 105 °C to 950 °C at 10 °C/min
- 4) Cool from 950 °C to 450 °C at 20 °C/min
- 5) Hold for 5 minutes at 450 °C

(switch the atmosphere from nitrogen to air)

- 6) Heat from 450 °C to 950 °C at 10 °C/min
- 7) Hold for 5 minutes at 950 °C



Figure 3.7: Perkin Elmer Pyris STA 4000 Thermogravimetric analyzer (right) equipped with Fourier-transform infrared spectrometer (left) at RÜZGEM.

Thermogravimetric curve (weight vs time) for the proximate analysis is shown in Figure 3.8. The proximate analysis is done according to procedures described in [68]. The intervals for release of moisture, release of volatiles, combustion of the fixed carbon, and the remaining ash are also highlighted in Figure 3.8. Unexpectedly, there observed a jump in the graph when time is around 100 minutes, however, it can be explained by the change of the gas supply as that interval coincides with the end of the step 5 of the experiment.

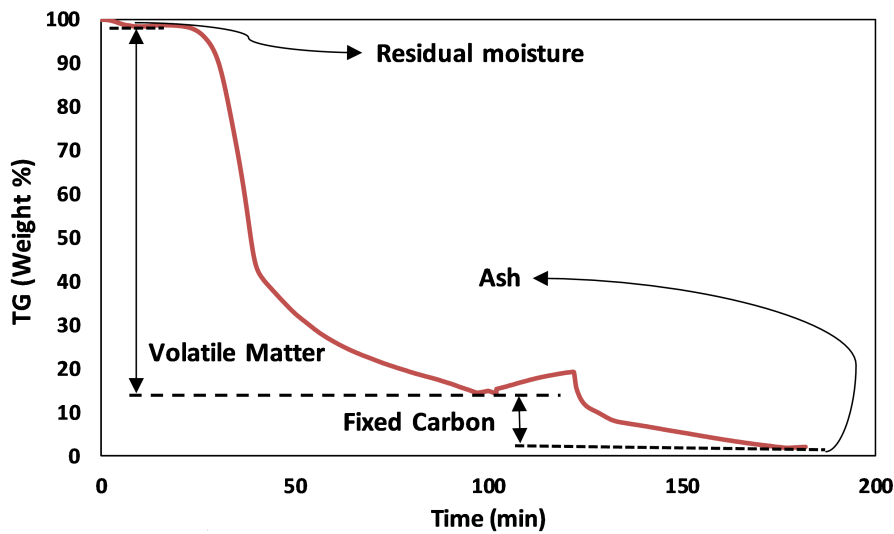


Figure 3.8: TGA profile for the proximate analysis.

Ultimate analysis, that is used to determine the elemental composition of the fuel, is performed by Central Laboratory of METU, and results are presented at Table 3.1.

TGA analysis to be used for the evaluation of combustion kinetic parameters is performed at Central Laboratory of METU under heating rate of 20 °C/min using thermogravimetric analyzer Perkin Elmer Pyris 1. Ash free TG and DTG curves from this analysis are presented in Chapter 4 at Figure 4.1.

Since the ash content of the studied OR sample is quite low (<2%) as it can also be observed from Figure 3.8, numerous experiments is needed to generate enough amount of ash to be delivered for ash analysis. The muffle furnace at Clean Combustion Technology Laboratory is used for the ashing by following the standard test method for ash in biomass ASTM E1755-01. The collected ash is delivered to Cen-

tral Laboratory of METU, where the fractions of inorganic matters are analyzed using Rigaku Ultima IV X-ray Diffractometer. The result of the ash analysis is presented at Table 3.1.

Table 3.1: Elemental analysis of the studied olive residue.

Parameter	
Moisture content (wt.%, as received)	
Moisture	7.5
Proximate Analysis (wt.%, dry basis)	
Volatile Matter	83.9
Fixed Carbon ^a	14.2
Ash	1.9
Ultimate Analysis (wt.%, dry ash free)	
C	51.5
H	6.2
N	0.7
S	-
O ^a	41.6
Lignocellulosic composition ^b (wt.%, dry ash free)	
Hemicellulose	37.8
Cellulose	37.3
Lignin	24.9
Ash analysis (wt.%, dry basis)	
SiO ₂	10.8
Al ₂ O ₃	3.3
Fe ₂ O ₃	4.6
CaO	33.1
SO ₃	10.0
MgO	4.4
P ₂ O ₅	8.5
K ₂ O	21.2
Na ₂ O	2.1
Cl	0.1
MnO	0.5
Other oxides	1.3
Calorific Value (dry basis)	
Higher Heating Value ^c (MJ/kg)	20.5

^a Calculated by difference

^b Calculated by an empirical correlation

^c Calculated numerically

3.4 Methodology for Biomass Characterization

3.4.1 Kinetic Parameters

As stated in Chapter 2, the kinetic analysis of solid fuel combustion is based on the rate equation supplied in Equation 3.1.

$$\frac{d\alpha}{dt} = k(T) f(\alpha) \quad (3.1)$$

where α is the conversion ratio, $d\alpha/dt$ is the conversion rate, k is the reaction rate, T is the temperature, and $f(\alpha)$ is the reaction model.

Note that Equations 3.1 and 3.2 are introduced in Chapter 2 as Equations 2.1 and 2.2. They are reintroduced here to improve the readability of this section.

The temperature dependence of the reaction rate, $k(T)$, is usually represented by the first order Arrhenius equation:

$$k(T) = A e^{-E_a/RT} \quad (3.2)$$

where A is the pre-exponential factor, E_a is the activation energy, R is the universal gas constant, and T is the temperature.

In thermogravimetric measurements, the conversion ratio (α) can be defined as the ratio of instantaneous weight loss to total weight loss given by equation:

$$\alpha = \frac{m_0 - m}{m_0 - m_f} \quad (3.3)$$

where m , m_0 and m_f are the instantaneous, initial and final masses of the sample, respectively.

The constant heat rate assumption is made for non-isothermal TGA experiments, and

this constant heat rate (β) is defined as:

$$\beta = \frac{dT}{dt} \quad (3.4)$$

Using Equation 3.4, Equation 3.1 can be transformed into:

$$\frac{d\alpha}{f(\alpha)} = \frac{k}{\beta} dT \quad (3.5)$$

where the left-hand side is a function of conversion ratio (α), and right-hand side is a function of temperature (T). Then, substituting Equation 3.2 into Equation 3.5, and integrating both sides of Equation 3.5, the following expression is obtained:

$$g(\alpha) = \int_0^\alpha \frac{d\alpha}{f(\alpha)} = \frac{A}{\beta} \int_0^T e^{-E_a/RT} dT \quad (3.6)$$

$g(\alpha)$ is only function of conversion ratio (α), and depends on the mechanism (presented at Table 3.2) controlling the reaction. Although no analytical solution exist for Equation 3.6, there are many approximations, with one of the most popular being the Coats-Redfern Method. CRM utilizes the asymptotic series expansion to approximate the exponential integral in Equation 3.6 [69], giving:

$$\ln \frac{g(\alpha)}{T^2} = \ln \left(\frac{A R}{\beta E_a} \left(1 - \frac{2 R T^*}{E_a} \right) \right) - \frac{E_a}{R T} \quad (3.7)$$

Plotting the left-hand side of Equation 3.7 versus $1/T$ gives E_a and A from the slope and intercept of the best fitted line as follows:

$$-\frac{E_a}{R} = \text{Slope} \quad (3.8)$$

$$\ln \left(\frac{A R}{\beta E_a} \left(1 - \frac{2 R T^*}{E_a} \right) \right) = \text{Intercept} \quad (3.9)$$

where T^* is the mean temperature of area of interest in TG data.

Using a model-fitting approach, i.e. CRM, enabled the fitting of different reaction mechanisms, represented by the mathematical function $g(\alpha)$. Within the context of this thesis, three main reaction mechanisms are evaluated: 1) reaction order controlled; 2) phase boundary reaction controlled; and 3) diffusion controlled. These mechanisms are presented at Table 3.2 as adapted from works of Gil et. al. and Phadnis [70, 71].

Table 3.2: Reaction models and corresponding $f(\alpha)$ and $g(\alpha)$ functions.

Model	$f(\alpha)$	$g(\alpha)$
Reaction Order Controlled		
O1 – First Order	$(1-\alpha)$	$-\ln(1-\alpha)$
O2 – Second Order	$(1-\alpha)^2$	$(1-\alpha)^{-1}$
O3 – Third Order	$(1/2)(1-\alpha)^3$	$(1-\alpha)^{-2}$
Phase Boundary Controlled		
R2 – Contracting Cylinder	$2(1-\alpha)^{1/2}$	$1-(1-\alpha)^{1/2}$
R3 – Contracting Sphere	$3(1-\alpha)^{2/3}$	$1-(1-\alpha)^{1/3}$
Diffusion Controlled		
D1 – 1-D Diffusion Controlled	$(1/2)(\alpha)^{-1}$	α^2
D2 – Valensi, 2-D	$(-\ln(1-\alpha))^{-1}$	$(1-\alpha) \ln(1-\alpha) + \alpha$
D3 – Jander, 3-D	$2(1-\alpha)^{2/3}(1-(1-\alpha)^{1/3})-1$	$(1-(1-\alpha)^{1/3})^2$
D4 – Ginstling-Brounshtein, 3-D	$(3/2)((1-\alpha)^{-1/3}-1)$	$1-2\alpha/3-(1-\alpha)^{2/3}$

After the plots of $\ln \frac{g(\alpha)}{T^2}$ vs $1/T$ are drawn for each reaction model, the goodness of the fitting is evaluated by the coefficient of determination, R^2 value, and the kinetic parameters E_a and A are found using Equations 3.8 and 3.9.

In reaction order controlled models (O1–O3), the dominant reaction mechanism is chemical kinetics; and models O1, O2, and O3 correspond to first, second, and third order, respectively. In the phase boundary controlled models (R2 and R3), the reaction is controlled by the movement of the interfaces of the particles. These interfaces move at constant velocities and cause reactions to occur almost instantaneously. As a result, the surface of the each particle is covered with layer of combustion products. Among the phase boundary controlled models, the contracting cylinder model (R2) creates a

reaction zone of circular structures, reacting inward from the periphery; whereas in the contracting sphere model (R3), spherical reaction zones are formed, and reacting radially inward from the surface. In diffusion controlled models (D1-D4), the reaction is controlled by diffusion of the oxygen into the reacting particles. 1-D diffusion represents a uni-dimensional diffusion where the reaction rate is only a function of diffusion barrier thickness; 2-D diffusion represents a two-dimensional diffusion into the cylinder where the reaction rate is functions of the radius and azimuth; and both D3 and D4 represent diffusion models that take three dimensions into account so that the particles are considered as spheres [28].

3.4.2 Higher Heating Value

The heating value of is one of the most important properties of biomass fuels especially for design considerations in power plant scale. Within the context of this thesis, heating rate is the only parameter from fuel characterization section that is directly integrated to hybrid power plant simulations along with the elemental composition of the fuel. However, the heating value of the studied OR is not determined experimentally due to lack of experimental equipment in Middle East Technical University. Fortunately, there are numerous studies in the literature to estimate the higher heating value (HHV) of biomass fuels accurately using proximate, ultimate and chemical analysis of the samples. It is suggested that the correlations based on ultimate analysis are the most accurate [72]. Therefore, eight different HHV correlations from the literature that are based on ultimate analysis of biomass fuels are selected and summarized in Table 3.3. Magalhaes et. al. [28] reported the HHV of their OR sample that are obtained from Balıkesir region of Turkey as 20.11 MJ/kg. Since the ultimate analysis of their OR is also available in the same study, a verification matrix using the ultimate analysis of Magalhaes et. al.[28] is created. Although all of the correlations in Table 3.3 shows good accuracy with a maximum absolute error smaller than 4.3%, the most accurate correlation in Table 3.3, Sheng and Azevedo [72] with an absolute error of 1.1%, is used in the evaluation of HHV of the studied OR within this thesis, resulting in HHV value of 20.5 MJ/kg, and presented in Table 3.1.

Table 3.3: Higher heating value estimation formulas for biomass fuels.

Source	Correlation (HHV, MJ/kg)
Tillman [73]	$HHV = 0.4373 C - 1.6701$
Gas Technology Institute [74]	$HHV = 0.341 C + 1.322 H - 0.120 - 0.12 N + 0.0686 S$ $- 0.0153 \text{ Ash}$
Graboski and Bain [75]	$HHV = 0.328 C + 1.4306 H - 0.0237 N + 0.0929 S$ $- (1-\text{Ash}/100) (40.11 H/C) + 0.3466$
Jenkins and Ebeling [76]	$HHV = -0.763 + 0.301 C + 0.525 H + 0.064 O$
Annamalai et. al. [76]	$HHV = 0.3516 C + 1.16225 H - 0.1109 O$ $+ 0.0628 N + 0.10465 S$
Demirbaş [77]	$HHV = 0.335 C + 1.423 H - 0.154 O - 0.145 N$
Channiwala and Parikh [78]	$HHV = 0.3491 C + 1.1783 H + 0.1005 S - 0.1034 O$ $- 0.0151 N - 0.0211 \text{ Ash}$
Sheng and Azevedo [72]	$HHV = -1.3675 + 0.3137 C + 0.7009 H + 0.0318 O$

3.4.3 Fouling and Slagging Potential

Slagging and fouling are two common types of ash deposition on the boiler surfaces. Generally, the distinction between them is made based the location where the deposition occurs. Slagging refers to deposition of molten ash in the radiative section of a boiler, i.e. mainly furnace walls of boiler, while fouling refers to the deposition of ash in the convective region, i.e. surfaces of superheater and reheaters. Both fouling and slagging possess serious threat to life cycle of boilers as they cause corrosion in the tubes and reduce the heat transfer rate within the boilers.

The slagging and fouling characteristics of biomass fuels are closely related to chemical composition of inorganic matter present in the biomass, i.e. ash. The concepts of slagging and fouling play crucial role for the design of biomass boilers. Therefore, numerous slagging and fouling indices to predict the ash behaviour during the combustion process are offered by researchers. For this purpose, empirical indices to predict the behaviour of especially biomass ash are introduced within this section.

Biomass fuels with high contents of silica and alkali metals can result in the formation of silicates with low melting point ($<800^{\circ}\text{C}$) that create deposits near the bed surfaces of the boiler. This tendency is especially common in herbaceous biomass fuels such as wheat or sorghum [79]. Miles et. al. [80] suggest that the alkali content of the fuel is one of the key indicator of the slagging and fouling problems in the boilers, and proposed the Alkali Index (AI) in Equation 3.10 to predict the effect of alkali metals in biomass ash on slagging and fouling potential:

$$AI = (K_2O + Na_2O) Ash / HHV \quad (3.10)$$

where HHV is the higher heating value (GJ/kg), Ash is the fraction of ash in the fuel, and K_2O and Na_2O are the weight percentages of these oxides (dry basis) in the ash composition.

According to this index:

$AI > 0.17$ kg Alkali per GJ fuel \rightarrow probable fouling and slagging.

$AI > 0.34$ kg Alkali per GJ fuel \rightarrow certain fouling and slagging at unmanageable

degree.

Chlorine plays a key role in promoting the transfer of potassium in the gas phase, where it participates in further reactions or is deposited on the cold surfaces. On these surfaces, it can react with the protective oxide layer of the boiler metal, and may initiate corrosion. Therefore, the following Chlorine-based index to predict the slagging in biomass fuels is proposed [79] :

$Cl < 0.2 \rightarrow$ low slagging trend.

$0.2 < Cl < 0.3 \rightarrow$ medium slagging trend.

$0.3 < Cl < 0.5 \rightarrow$ high slagging trend.

$0.5 < Cl \rightarrow$ very high slagging trend.

where Cl represents the chlorine content (% weight, dry basis) of the biomass ash.

Another useful parameter for predicting the fouling and slagging potential of the fuels is base-to-acid ratio (B/A), given in the Equation 3.11. In this equation, the compounds in the nominator are termed as basic compounds, B , and have low melting points; while the compounds in the denominator are called as acidic compounds, A , and have high melting points. Although there is no clear consensus in the literature for the interpretation of B/A values, some remarks can be given as Pronobis et. al [81] states that the slagging is low while $B/A < 0.75$ and $B/A > 2$, and the slagging potential is high between 0.75 and 2. Similarly, Teixeira et al. [82] suggest that slagging is maximum when B/A is around 0.75; meaning slagging is decreased as B/A increases from 0.75 to 2 or decreases below 0.75.

Originally, the parameter B/A is derived for the fuels for low phosphorus content, e.g. coal. However, most of the biomass fuels have considerable phosphorus content, and the phosphorus pentoxide, P_2O_5 , has the potential to drop melting temperature of the ash due to having a low melting temperature (569 °C), which ultimately increases the slagging potential. Therefore, a modified B/A ratio with addition of phosphorus, $B/A(+P)$, is proposed and given in Equation 3.12. Since base-to-acid ratio is also a useful parameter to calculate other indices such as Slagging and Fouling indices, (S_I and F_I), supplied in Equations 3.13-3.14, the modified ratio, $B/A(+P)$, is employed

in the calculation of S_I and F_I for the studied OR herein after. Another parameter for determining the slagging potential, Slag Ratio, S_R , is also supplied in Equation 3.15 [83].

$$B/A = \frac{Fe_2O_3 + CaO + MgO + Na_2O + K_2O}{SiO_2 + Al_2O_3 + Ti_2O} \quad (3.11)$$

$$B/A(+P) = \frac{Fe_2O_3 + CaO + MgO + Na_2O + K_2O + P_2O_5}{SiO_2 + Al_2O_3 + Ti_2O} \quad (3.12)$$

$$S_I = B/A(+P) \cdot S^d \quad (3.13)$$

$$F_I = B/A(+P) \cdot (Na_2O + K_2O) \quad (3.14)$$

$$S_R = \frac{SiO_2}{SiO_2 + Fe_2O_3 + CaO + MgO} \cdot 100 \quad (3.15)$$

Note that in above Equations 3.11-3.15: Al_2O_3 , CaO , Fe_2O_3 , K_2O , MgO , P_2O_5 , SiO_2 , and Ti_2O represent the weight percent of these compounds in the ash composition, while S^d is the weight concentration of sulphur on dry basis in the fuel.

In order to predict the slagging and fouling potential, the approximate ranges for Slagging Index, Slag Ratio and Fouling Index are provided in Table 3.4 as adapted from Febrero et. al[83].

3.4.4 Lignocellulosic Composition and Combustibility Index

Although biomass sources exist in diverse forms and compositions, they are generally chemical mixtures of polymer components, i.e., cellulose, hemicellulose, and lignin, as well as extractives. The chemical composition of the biomass source in terms of these polymers is one of the key parameters to determine the devolatilization characteristics, and therefore experiments are commonly conducted to determine the

Table 3.4: Approximate ranges for the selected slagging and fouling indices[83].

Parameter	Approximate Ranges
Slagging Index	$S_I < 0.6$ low slagging
	$S_I = 0.6-2.0$ medium
	$S_I = 2.0-2.6$ high
	$S_I > 2.6$ extremely high
Slagging Ratio	$S_R > 72$ low slagging
	$72 > S_R > 65$ medium
	$S_R < 65$ high
Fouling Index	$F_I < 0.6$ low fouling
	$0.6 < F_I < 40$ high
	$F_I > 40$ extremely high
	(tendency to sintering of deposits)

lignocellulosic composition of the biomass fuels. However, since this thesis focus on preliminary analysis on biomass, no experiment is done to determine the lignocellulosic composition of the studied OR. Instead, an empirical model based on ultimate and proximate analysis of the fuel is employed to calculate the lignocellulosic composition of the studied OR, according to Equations 3.16-3.17 [84]. The correlation range for the method developed by Sheng and Azavedo [84] is also given in Table 3.5. Note that for the studied OR, the values for O/C , H/C , and VM are 0.60, 1.44, and 83.9% respectively.

$$\begin{aligned}
 cellulose = & -1019.07 + 293.810 (O/C) - 187.639(O/C)^2 + & (3.16) \\
 & 65.1426(H/C) - 19.3025(H/C)^2 + 21.7448(VM) - \\
 & 0.132123 (VM)^2
 \end{aligned}$$

$$\begin{aligned}
 lignin = & 612.099 + 195.366 (O/C) - 156.535(O/C)^2 + & (3.17) \\
 & 511.357(H/C) - 177.025(H/C)^2 - 24.3224(VM) + \\
 & 0.145306 (VM)^2
 \end{aligned}$$

where VM represents the volatile matter in weight percent dry ash free basis; O/C

and H/C are the molar ratios of oxygen to carbon, and hydrogen to carbon, respectively. The hemicellulose composition is calculated by the difference.

Table 3.5: Correlation range of the method developed by Sheng and Azevedo[84].

	O/C (molar ratio)	H/C (molar ratio)	VM (wt.%)
Range	0.56-0.83	1.26-1.69	73-86

The combustion characteristics of fuel are often represented by the characteristic temperatures, as explained in Chapter 2. Combining these characteristic temperatures with TG data, a more comprehensive parameter, combustibility index, S , can be obtained as suggested by Zou et. al. [85]. Combustibility index can provide better measurement for the reactivity of the fuel, since it is sensitive to both the maximum rate of weight loss during the thermogravimetric analysis, and the characteristic temperatures, T_{ig} and T_B . Higher value of S means that the fuel combustion reactivity is better [85].

$$S = \frac{|dW/dt|_{max} \cdot |dW/dt|_{mean}}{T_{ig} \cdot T_B} \quad (3.18)$$

where $|dW/dt|_{max}$ and $|dW/dt|_{mean}$ represent the maximum and average rate of weight loss, respectively; while T_{ig} and T_B are the ignition and burnout temperatures ($^{\circ}\text{C}$), respectively.

CHAPTER 4

BIOMASS CHARACTERIZATION RESULTS

In this chapter, the results of experimental work on characterization of the studied biomass are discussed.

4.1 Results based on TGA data

Combustion experiment of the studied OR is conducted under heating rate of 20 °C/min, using a thermogravimetric analyzer. The thermogravimetric (TG) and derivative thermogravimetric (DTG) curves as a function of the temperature are presented in Figure 4.1 along with the identified stages of combustion where the moisture release stage is excluded. The characteristic temperatures of the studied OR based on the conducted TGA are also obtained using the method of characteristic temperatures, as explained in Chapter 2.

In Figure 4.1, Stage A refers to decomposition stage where the bonds between clusters of hydrocarbons are start to be loosen and break. This stage is defined between Decomposition Temperature (T_D) and Ignition Temperature (T_{ig}). Typically, the combustion stage in fuels is defined between Ignition Temperature (T_{ig}) and Burnout Temperature (T_B). However, for the studied OR, the combustion stage is divided into two stages, B and C. Stage B refers to main stage of combustion and defined by the major peak in DTG curve. Stage C, on the other hand, refers to the second stage of combustion, characterized by the second DTG peak. The existance of a secondary combustion stage in TGA data is attributed to the fact that volatiles and char are burning separately and it is a common phenomenon in biomass fuels [86].

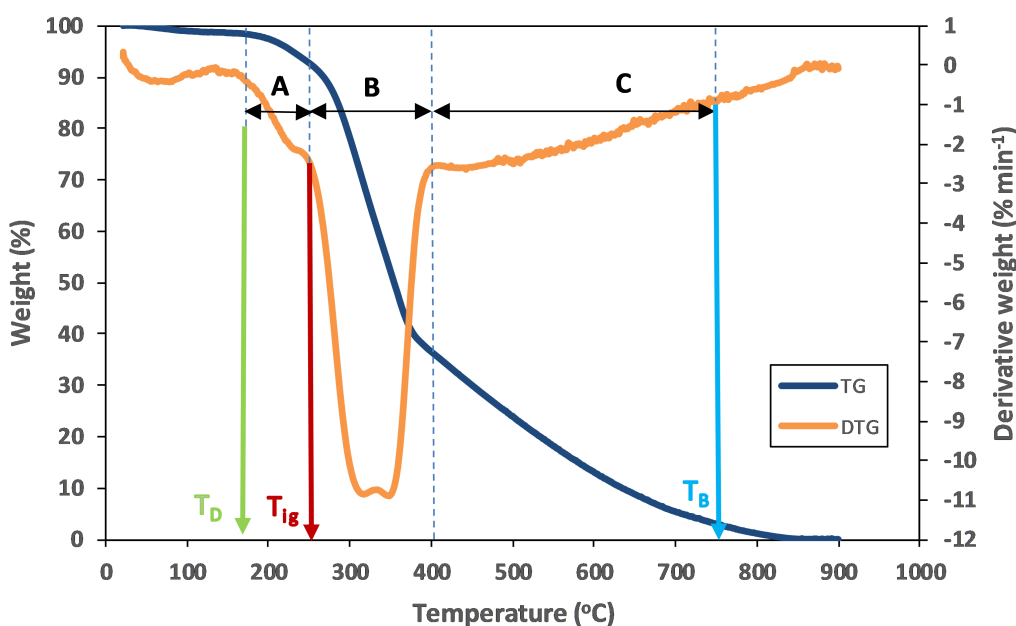


Figure 4.1: TG and DTG profiles for the studied OR under 20 °C/min with indication of characteristic temperatures and combustion stages

The weight loss of the respective stages A, B and C are presented at Table 4.1. According to Figure 4.1 and Table 4.1, the following arguments can be made. During the combustion, the studied OR showed two distinct stages of weight loss, Stage B and Stage C. Stage B is defined between 247 and 412 °C with twin peaks at 323 and 347 °C. The underlying theory leading to this result might be the release of two different volatile species with different but close peak temperatures around 340 °C. Since Fourier-transform infrared spectroscopy (FTIR) analysis is not done during the TGA, this hypothesis cannot be verified. FTIR is an experimental technique which is commonly used with TGA by coupling a FTIR device to TGA analyzer, as it also can be seen from Figure 3.7. It allows detection and measurement of gaseous species released during thermogravimetric analysis. The secondary combustion stage, Stage C, is defined between 412 and 737 °C with no pronounced peak. Considering the weight losses for Stage B and C, which are obtained from Table 4.1 as 38.8% and 48.7% respectively, and the volatile matter of the OR, i.e. 83.9%, from Table 3.1, it can be suggested that partial volatile combustion occurred during Stage B, while the rest of volatiles are combusted concurrently with fixed carbon during Stage C. In addition

to that, since sum of weight losses for Stage A and B, i.e. 87.5%, is lower than the sum of volatile matter and fixed carbon content of the studied OR, it indicates that the release of volatiles started to take place during the decomposition stage defined as Stage A.

Table 4.1: Weight losses for defined stages of combustion (in wt.%, dry basis), and unaccounted weight for studied OR.

Loss in Stage A	Loss in Stage B	Loss in Stage C	Total Loss	Ash content	Unaccounted
5.7	38.8	48.7	93.2	1.9	4.9

In order to provide more comprehensive and qualitative understanding on the combustion behaviour, the combustibility index, S , for the main stage of combustion, Stage B, is calculated and provided at Table 4.2 along with the characteristic temperatures for the studied OR. The calculated S value (units in $10^7\%min^{-1}K^{-3}$) for the studied OR, 16.8, is close to the value reported by Magalhaes et. al. [28], i.e. 25.3, for their OR but under the heating rate of 40 °C/min. The reported S values in their study for heating rates of 15 and 20 °C/min are 5.3 and 7.8, respectively. It is commonly reported in the literature that the combustibility index of the biomass fuels are higher than those of coals, it is increased as the biomass ratio of the coal-biomass blend is increased while being also directly proportional to increased heating rate [87] [88] [89]. In line with these findings, studied OR within this thesis exhibits a shifted behaviour to 40 °C/min of the OR studied by Magalhaes et. al. [28]. Combustibility index for another biomass fuel, babassu nutshell, under heating rate of 10 °C/min is reported as 17.88 by Protasio et. al. [87], and this value is interpreted as high compared to other biomass fuels. Therefore, the calculated S value for the studied OR in this thesis can refer to good combustibility characteristics compared to available studies in the literature.

Table 4.2: Characteristic temperatures (T_D – Decomposition Temperature; T_{ig} – Ignition Temperature; T_P – Peak Temperature; T_B – Burnout Temperature) of the studied OR in °C and Combustibility Index, S for Stage B

T_D	T_{ig}	T_P	T_B	$S (10^7\%min^{-1}K^3)$
180	247	347	737	16.8

The occurrence of two distinct combustion peaks for DTG in Figure 4.1 is also observed in studies of Yüzbaşı and Selçuk [17] and Magalhaes et. al. [28] where they investigated the characteristics of Turkish olive residue samples along with other fuels such as lignites. Specifically, Magalhaes et. al. [28] presented the TG and DTG curves of their OR sample for heating rates of 15, 20 and 40 °C/min. Although the TGA experiments within this thesis conducted under a single heating rate of 20 °C/min, both TG and DTG graphs in Figure 4.1 exhibit very good agreement with the TG and DTG curves presented by Magalhaes et. al. [28] under heating rate of 40 °C/min. For the other Turkish OR studied by Yüzbaşı and Selçuk [17], where the effect of the combustion environment is investigated under a single heating rate of 40 °C/min, the reported decomposition, ignition and peak temperatures are around 180, 250 and 310 °C, respectively, varying slightly over changing environment. Considering that these temperatures are in good agreement with the obtained temperatures at Table 4.2, it can be claimed that the direct results from the conducted TGA are in line with the findings on Turkish OR available in the literature.

4.2 Results on Kinetic Parameters

In determination of kinetic parameters for combustion, there is no consensus in the literature on the definition of the combustion interval as Gangavati et. al. [90], Wang et. al. [91], and Fang et. al. [92] consider single global reaction while Gil et al. [70] considers two stage reaction with three potential main reaction mechanism as provided in Table 3.2. In this thesis, the latter is adopted since two distinct combustion intervals, Stage B and C, are observed in DTG for the studied OR. In addition to that, two stage reaction method is also adopted by Alvarez et. al. [35] in determination of kinetic parameters of 28 biomass fuels, and therefore it is possible to make comparison of the studied OR with the 28 benchmark biomass results for both of the stages, B and C. Being particularly important for including an analysis on Turkish OR, Magalhaes et. al. [28] adopted the same method from Gil et al. [70], and thus adding another set of array for comparison.

The plots of left-hand side of Equation 3.7 versus $1/T$ are drawn for each of the 9 reaction model given in Table 3.2 for respective combustion stages B and C, and

supplied in Figure 4.2. The best fitting model is selected based on the R^2 value, and the kinetic parameters are calculated using Coats Redfern Method as explained in Chapter 3. The best fitting models and obtained kinetic parameters are summarized in Table 4.3.

Table 4.3: Temperature intervals, correspondent models and the kinetic parameters

Stage	T (°C)	Model	R^2	E_a (kJ/mol)	A (1/min)	k (1/min)
A	247-412	O3	0.9556	32.6	607.7	1
B	412-737	D3	0.9891	17	0.6	0.07

The results suggest that Stage B is best characterized by a reaction order controlled mechanism, particularly O3 - a third order model. The apparent activation energy for this stage is found as 32.6 kJ/mol. For Stage C the best fitted model is a diffusion controlled mechanism, D3, described by Jander's equation for solid state reaction kinetics in a sphere where diffusion in three directions play important role. The apparent activation energy for this stage is found as 17 kJ/mol.

Despite the best fitted models (O1 and D1, respectively, for Stage B and C) are different for the Turkish OR studied by Magalhaes et. al. [28], the dominant mechanisms (reaction order and diffusion controlled, respectively) are same as the ones found in this thesis.

It should be noted that although the pre-exponential constant (A) and the reaction rate (k) are considered as kinetic parameters (three of E_a , A , and k are referred as kinetic triplets), A and k values are not commonly reported in the literature. Therefore, a comparison table consisting of E_a values corresponding to two combustion stages of 28 biomass fuels under the heating rate of 15 °C/min is presented in Table 4.4 [35]. Apparent E_a values of Turkish OR from the study of Magalhaes et. al. [28] for heating rates of 15, 20 and 40 °C/min are also added to this table for comparison purposes. It should be noted that CRM is used in the evaluation of kinetic parameters for all of the presented cases.

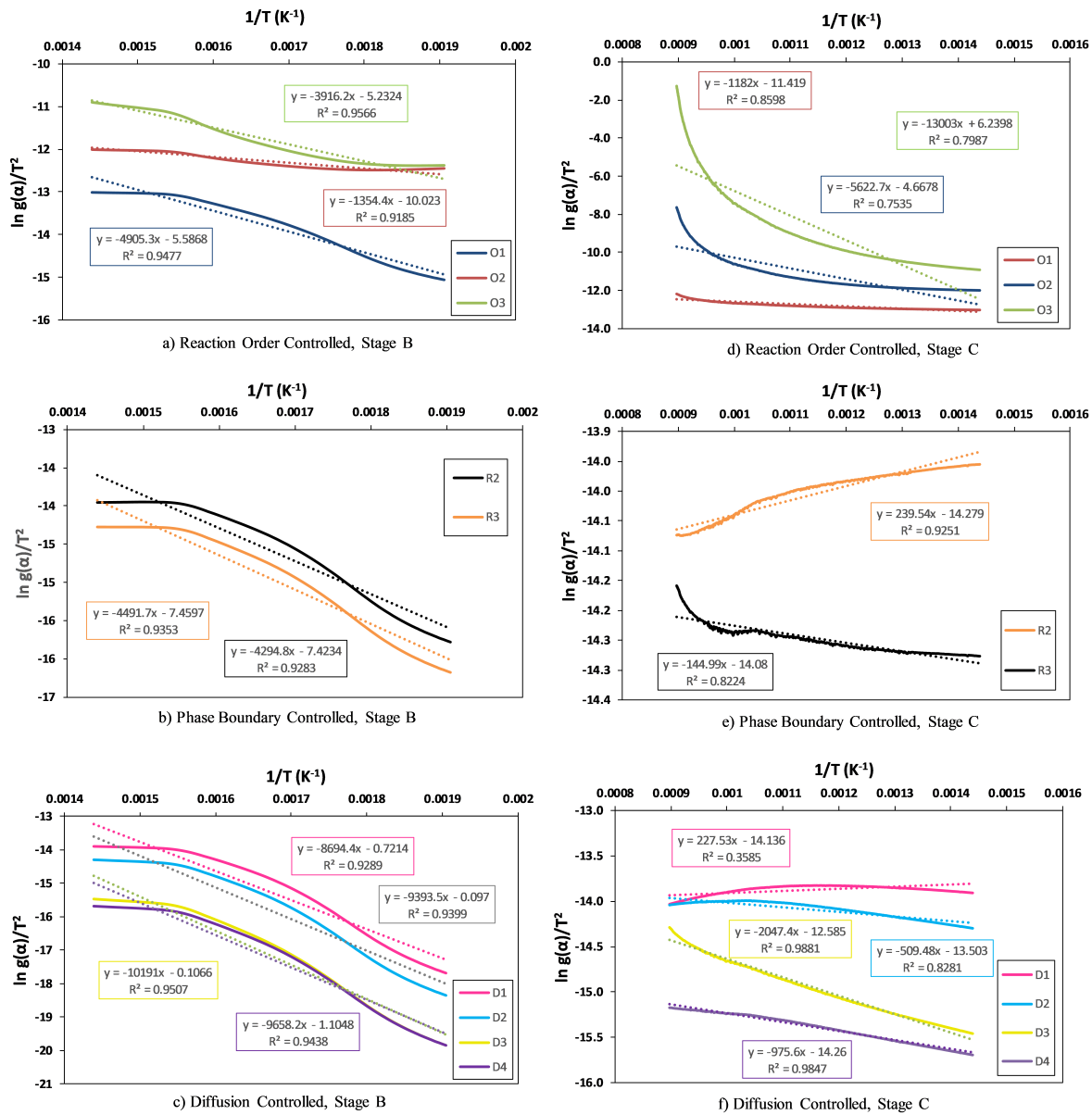


Figure 4.2: Evaluation of fittings to Stage B and C using reaction mechanism supplied in Table 3.2. O1 – First Order; O2 – Second Order; O3 – Third Order; R2 – Contracting Cylinder; R3 – Contracting Sphere; D1 – 1-D Diffusion Controlled; D2 – Valensi 2-D; D3 – Jander 3-D; D4 – Ginstling-Brounshtein, 3-D. Equation of the lines and the R^2 values are given in cascades as the same color with the fittings.

Table 4.4: Apparent activation energy values for the selected biomass fuels.

Sample	Stage B	Stage C
	E_a (kJ/mol)	E_a (kJ/mol)
Studied OR	32.6	17
Alvarez et. al. [35]		
Extracted olive pomace	32.3	14.6
Olive stone	46.3	47.6
Olive tree pruning	36.4	19.2
Almond shell	48.2	17.1
Apple tree leaves	29.4	20.6
Beetroot pellets	21.6	23.2
Briquette	42.8	55.5
Chesnut tree chips	46.6	53.8
Cocoa bean husk	29	15.1
Coffee bean husk	34.6	62.5
Corn cob	86.9	19.5
Eucalyptus tree chips	41.8	63
Gorse	30.7	47.1
Grape seed flour	25.6	57
Miscanthus	37.9	50.9
Pepper plant	21.4	47.3
Pine and pineapple leave pellets	45.1	7.5
Pine kernel shell	40.5	48.1
Pineapple leaf	36.9	49.2
Rice husk	53.9	32.8
Sainfoin	34.9	40.9
Scrubland pruning	29	20.9
Sorghum	49.9	18.1
Thistle	34.6	35
Vine shoot	51.6	48.2
Wheat straw	77.5	23.4
Wheat straw pellets	54.6	27.5
Magalhaes et. al. [28]		
Olive residue (15 °C/min)	44.2	13.4
Olive residue (20 °C/min)	46.5	12.1
Olive residue (40 °C/min)	47.7	9.1

In Table 4.4, it is observed that all of the reported apparent activation energy values lies in the range of 7 to 87 kJ/mol including the studied OR. Among the reported biomass fuels, extracted olive pomace [35] and the olive residue [28] are the most important ones due to being almost the same fuels as the studied OR, and thus it allow us to make a comparison. It should be noted that the terms olive pomace, olive residue and olive husk are used interchangeably as mentioned in Chapter 2. When the E_a values of the studied OR are compared with those of extracted olive pomace [35] and the olive residue [28], it is observed that E_a values tend to decrease as moved from Stage B to Stage C. Particularly, E_a values for the studied OR are in good agreement with those of extracted olive pomace reported by Alvarez et. al. [35]. On the other hand, obtained E_a values for the studied OR are slightly lower and slightly higher, respectively for Stage B and C, than those of reported by Magalhaes et. al. [28]. Several reasons might lead to this deviation. First of all, the biomass fuels themselves are obtained from different regions of Turkey. Their extraction methods might be different as no background information for the fuel is reported by Magalhaes et. al. [28]. In Turkey, the majority of the olive oil production is performed using 3-phase extraction technologies[93]. Since the studied OR is obtained through traditional pressing, it is likely that oily extractives are still present in the fuel. The lower E_a value for the Stage B might be the consequence of these residual extractives. Alternatively, the relatively higher content of the volatile matter for the studied OR might lead to lower apparent activation energy for Stage B, as well. The relatively higher value of the activation energy at Stage C, on the other hand, can be explained by the lower content of lignin for the studied OR compared to that of OR in Magalhaes et. al. [28]. It is reported that the required activation energy for lignin can be similar or even less than that of hemicellulose or cellulose [94] [95]. The low activation energy may cause lignin to decompose at lower temperatures, and thus making the decomposition of ligning to span over a broad temperature interval since the tightly bound ligning fibers cannot be cleaved rapidly [28].

Ultimately, despite the slight deviations in calculated apparent activation values for Stage B and C, it can be concluded that the kinetic parameters for the studied OR are in line with the findings from the literature.

4.3 Results on Slagging and Fouling Potential of the Fuel

The slagging and fouling characteristics of the studied OR is evaluated using the indices introduced in Chapter 3. The results and the potential tendencies for slagging and fouling are presented at Table 4.5.

Table 4.5: Slagging and Fouling Potential of the studied fuel.

Parameter	Value	Fouling and Slagging Potential
Alkali Index, AI	0.22	Probable
Chlorine Index	0.1	Low
Base-to-acid ratio, B/A	4.7	Low
Modified Base-to-acid ratio, B/A+P	5.3	Low
Slagging Index, S_I	1	Medium
Fouling Index, F_I	20.3	High
Slag Ratio, S_R	1.2	High

Based on the Alkali Index, the studied OR exhibits probable tendency for fouling and slagging mostly due to the significant amount of potassium oxide (K_2O) present in the biomass ash, 21.2 wt %. It is reported that potassium melts and vaporizes readily during combustion, and it is commonly deposited on screen tubes of tertiary superheaters along with the calcium silicates ($2 CaO \cdot SiO_2$) [80]. This potential could be especially severe if high temperatures are reached within the boiler considering that the sum of calcium oxide (CaO) and silicon dioxide (SiO_2) is 43.9 wt. % for the studied OR. Regarding Chlorine, Base-to-acid, and Modified Base-to-acid indices, studied OR seems to have a low tendency for slagging and fouling. However, the fouling and slagging potential solely based on the Base-to-acid ratios is a topic where the consensus is not achieved among the researchers. Rather, they are used in calculation of other indices, e.g. S_I and F_I . The studied OR shows medium and high tendency to slagging and fouling, respectively, based on the Slagging (S_I) and Fouling (F_I) indices. Alkali concentration (K_2O and Na_2O) is the main reason that led to high fouling potential based on the Fouling Index, while the 10 wt. % sulphur dioxide (SO_3) in the ash is responsible for the medium tendency for slagging based on (S_I). Finally, Slag Ratio (S_I) revealed that the studied OR has a strong tendency to slagging mostly due to high calcium oxide (CaO) concentration in the ash, 33.1

wt. %. S_R is related with the slag viscosity and implies that low value of S_R causes low viscosity and therefore high slagging inclination [81]. If the high slagging and fouling potentials based on the S_R and F_I values, respectively, are taken into account, it can be suggested that there might be serious slagging potential for the studied OR since thick deposits can be formed on the surfaces due to high F_I and cannot be removed due to slightly low viscosity (S_R value). It is reported that the slag viscosity should fall into a certain range in the boilers so that slag removal should be possible with soot and wall blowing [96].

Overall, the slagging and fouling potential of the studied OR is discussed based on the results of available empirical indices in the literature, however, it should be highlighted that the slagging and fouling tendency does not solely dependant on the inorganic matter of the fuel but also influenced by other parameters. Despite being less important than the inorganic composition, organic matter of the fuel also have an impact on fouling tendency [83]. Combustion parameters such as airflow is another parameter having a notable effect. For example, by increasing the amount of supplied air to the boiler, greater turbulence and larger excess air is achieved, resulting in less fouling but in the cost of decreased boiler efficiency. The design of the boiler itself also is one of the most important parameters effecting the slagging and fouling potential, therefore the preliminary results found in this section can create a starting point for the design of a boiler (or heater) using the studied OR as a fuel.

CHAPTER 5

METHODOLOGY FOR HYBRIDIZATION

In this chapter, the fundamental thermodynamic principles for single flash geothermal Rankine cycle and Recompression sCO₂ cycle are briefly discussed. Subsequently, the design parameters of the proposed hybrid power plant model is explained.

5.1 Mathematical Background

5.1.1 Single Flash Geothermal Steam Rankine Cycle Equations

Thermodynamic processes that a geofluid undergoes in single flash type GEPP are best demonstrated by a T-s diagram. The typical T-s diagram of a single flash GEPP is presented at Figure 5.1.

After the geofluid is collected through the production wells, it is allowed for mixing at a mixing chamber generally at 2-phase state (State 1), before subjected to the throttling process called "flashing". Since the flashing process is assumed as an isenthalpic process, one can write:

$$h_1 = h_2 \quad (5.1)$$

where h represent the enthalpy of the geofluid.

It should be noted that despite the presence of impurities in the geothermal water such as heavy metals, minerals, gaseous components such as CO₂, the geofluid within this thesis is assumed and modeled as pure water. Thus, all intensive thermodynamic

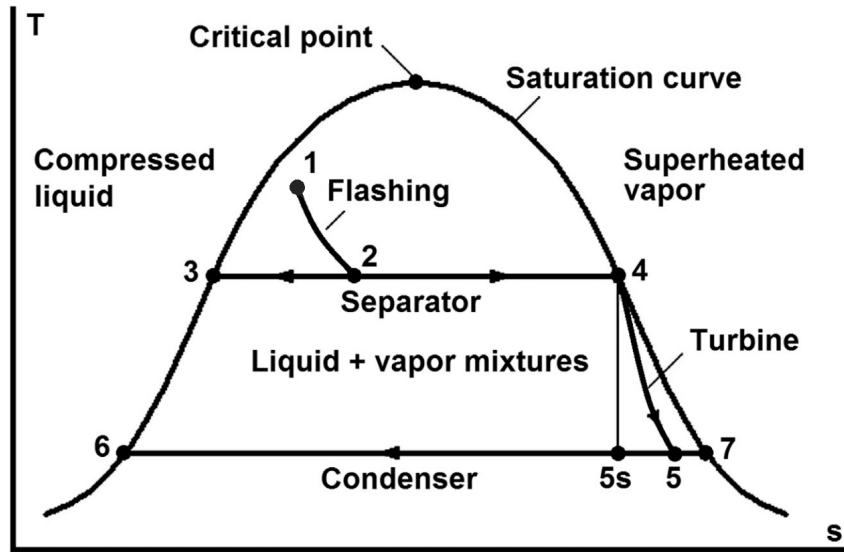


Figure 5.1: T-s diagram for a single flash GEPP

properties of geofluid are obtained for pure water in EBSILON.

After the flashing, the separation takes place as an isobaric process between states 2 and 3-4 in Figure 5.1. The quality of the mixture at State 2, is found from:

$$x_2 = \frac{h_2 - h_3}{h_4 - h_3} \quad (5.2)$$

where x is the quality of water.

Note that the states 3 and 4 are located on the saturated liquid and vapor curves, respectively, and enthalpies at the respective states can be found using the so-called lever rule of thermodynamics [97].

The geofluid leaving the separator as saturated liquid (State 3) is either further utilized in district heating or being reinjected through the injection wells in single flash GEPPs. In any case, it is out of scope of this thesis. The stream leaving separator as saturated vapor (State 4) is expanded in the steam turbine. The specific work produced by the steam turbine, w_t , is calculated as:

$$w_t = h_4 - h_5 \quad (5.3)$$

Note that this expansion process is not an ideal (isentropic) process. The isentropic turbine efficiency, η_t , is the ratio of the actual specific work to the isentropic specific work, and is expressed as:

$$\eta_t = \frac{h_4 - h_5}{h_4 - h_{5s}} \quad (5.4)$$

where State 5s represents the end of isentropic expansion process.

The total power output of the turbine, \dot{W}_t , is calculated as:

$$\dot{W}_t = x_2 \dot{m}_{total} w_t \quad (5.5)$$

The mechanical power generated by the turbine, \dot{W}_t , is converted into the electrical power, \dot{W}_e , upon multiplication with the generator efficiency, η_g :

$$\dot{W}_e = \eta_g \dot{W}_t \quad (5.6)$$

The power consumption of the auxiliary components such as pumps, cooling tower fans etc. should be extracted from \dot{W}_e to find the net power output of the power plant.

In his comprehensive book on geothermarmal power plants, DiPippo suggests using a modified isentropic efficiency for geothermal turbines before using Equation 5.4 [97]. Considering that the geothermal steam turbines operate in the wet region of water dome (Figure 5.1) DiPippo suggests an average of 1% drop in the turbine efficiency for each 1% deviation from the saturated vapor state. This new isentropic efficiency is called as wet turbine efficiency, η_{tw} , and is calculated as:

$$\eta_{tw} = \eta_{td} \frac{x_4 + x_5}{2} \quad (5.7)$$

where η_{td} is the dry turbine efficiency and can be conservatively assumed as 0.85 for geothermal steam turbines.

It should be noted that all of the characteristic equations for the single flash geother-

mal (Equations 5.1-5.14) in this thesis are compiled from the comprehensive geothermal book of DiPippo [97].

The fluid properties at State 5s can easily be calculated from the known pressure and entropy values at State 5s. Then, the enthalpy at State 5 is found using the following equation where the negative effect of moisture on the turbine efficiency is taken into account:

$$h_5 = \frac{h_4 - F \left(1 - \frac{h_6}{h_7 - h_6}\right)}{1 + \frac{F}{h_7 - h_6}} \quad (5.8)$$

where factor F is defined as:

$$F = \frac{\eta_{td}}{2} (h_4 - h_5) \quad (5.9)$$

The energy balance equation for the condensing process relates the required flow rate of cooling water, \dot{m}_{cw} , to the steam flow rate, $x_2 \dot{m}_{total}$, as follows:

$$\dot{m}_{cw} = x_2 \dot{m}_{total} \frac{h_5 - h_6}{\bar{c} (T_6 - T_{cw})} \quad (5.10)$$

where \bar{c} and T_{cw} are the mean specific heat of the water during the condensation process and inlet temperature of the cooling water, respectively.

Note that the Equation 5.10 is valid for direct-contact (DC) type condensers, which is the case for Kızıldere-1 GEPP. In DC condensers, there is one outlet stream as opposed to two outlet streams in surface-contact type condensers. The turbine exhaust is condensed upon mixing with the cooling water coming from the wet cooling tower (WCT) by means of vacuum effect. A representative sketch is for DC condenser supplied in Figure 5.2. Note that the condensate outlet at State 6 is directed to the WCT through the cooling tower circulation pump.

The condensate outlet from the condenser (State 6) is pumped to the cooling tower (State 8) where it falls naturally with gravity. The ambient air enters WCT with a

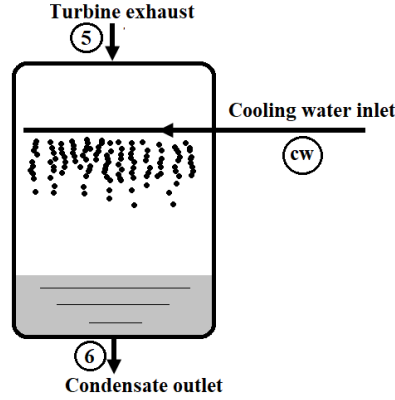


Figure 5.2: Direct-contact condenser. Vessel is assumed to be perfectly insulated.

certain amount of water vapor which depends on the relative humidity of the air, and picks up more water vapor as the condensate cools down due to chilling effect. The evaporation of the water vapor removes heat from the condensate water, and thus decreases its temperature. The following first law equation describes the overall operation of the WCT under steady state and adiabatic conditions:

$$\dot{m}_g h_g - \dot{m}_{cw} h_{cw} = \dot{m}_d h_d - \dot{m}_a h_a + \dot{m}_b h_b \quad (5.11)$$

where the subscripts d,a and b represent the air outlet, air inlet, and blowdown water, respectively.

Note that both the air inlet and air outlet streams contain water in the vapor phase. The mass conservation for the water can be written as:

$$\dot{m}_g - \dot{m}_{wa} = \dot{m}_{cw} - \dot{m}_b + \dot{m}_{wd} \quad (5.12)$$

where \dot{m}_{wa} and \dot{m}_{wd} represent the water content of the inlet and outlet air, respectively. These values can be found from the specific humidity, ω , of the air streams as:

$$\dot{m}_{wa} = \omega_a \dot{m}_a \quad (5.13)$$

$$\dot{m}_{wd} = \omega_d \dot{m}_d \quad (5.14)$$

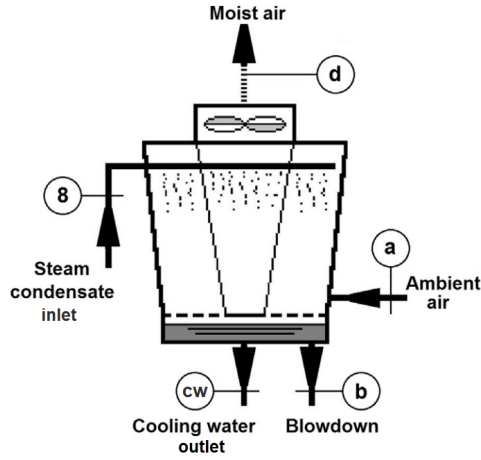


Figure 5.3: Representative sketch of the wet cooling tower.

5.1.2 The sCO₂ Cycle Equations

The modeled RC sCO₂ cycle in this thesis consists of the following components as depicted in Figure 2.7: 2 compressors, 1 turbine, 1 heater, 1 splitter, 1 mixer, and 3 heat exchangers, i.e. high temperature recuperator (HTR), low temperature recuperator (LTR) and the cooler. For the sake of simplicity, the governing thermodynamic relations of the sCO₂ cycle is supplied for the simple recuperated cycle presented in Figure 2.5.

The compressor is used for increasing the pressure of the CO₂ at the vicinity of the critical point of the CO₂ as mentioned previously. The work consumed by the compressor between the fixed states of 1 and 2 (Figure 2.5) is found for the adiabatic compression case as [98]:

$$\dot{W}_{in} = \frac{\dot{m} (h_2 - h_1)}{\eta_{comp}} \quad (5.15)$$

where \dot{W}_{in} , η_{comp} , and \dot{m} are the power input, the isentropic efficiency of the compressor, and the mass flow rate of the cycle, respectively.

Similarly, for the turbine operating between the fixed states of 4 and 5 in Figure 2.5, the mechanical power produced by the turbine, \dot{W}_{out} , is found from:

$$\dot{W}_{out} = \dot{m} (h_4 - h_5) \eta_{turb} \quad (5.16)$$

where η_{turb} is the isentropic efficiency of the turbine.

The heat exchangers (cooler and recuperator) are modeled as counter flow heat exchangers, and are governed by either of the two inputs: the effectiveness or the terminal temperature difference (TTD). The terminal temperature difference can be divided into two, namely lower terminal temperature difference (LTTD) and upper terminal temperature difference (UTTD). LTTD and UTTD represent the temperature difference of the two streams on the inlet and outlet side of the cold flow, respectively. In this thesis, effectiveness is used as the input variable for the heat exchangers where a positive minimum temperature difference along the heat exchanger, i.e. pinch point, is always ensured. Effectiveness (ϵ) is a performance parameter for heat exchangers and becomes 100% for the adiabatic case transferring the maximum amount of heat. The formula for effectiveness is expressed as follows [98]:

$$\epsilon = \frac{\dot{Q}_{actual}}{\dot{Q}_{max}} = \frac{(\dot{m} c_p \Delta T)_{cold\ or\ hot}}{(\dot{m} c_p)_{min} (T_{hot,in} - T_{cold,in})} \quad (5.17)$$

where $(\dot{m} c_p)_{min}$ is the smaller of the heat capacity rate between hot and cold fluids, and $(\dot{m})_{min}$ is the smaller mass flow rate.

The modeled heat exchangers in EBSILON are discretized and Equation 5.17 is solved for the temperatures of cold and hot streams using the predetermined value of effectiveness. Using the found outlet temperatures of hot and cold streams, log mean temperature difference ($LMTD$) can be defined as:

$$LMTD = \frac{(T_{hot,in} - T_{cold,out}) - (T_{hot,out} - T_{cold,in})}{\ln \frac{T_{hot,in} - T_{cold,out}}{T_{hot,out} - T_{cold,in}}} \quad (5.18)$$

where subscripts in and out imply the inlet and outlet of streams, respectively.

The heat exchanger conductance (commonly known as UA value and expressed in kW/K), is dependent on the effectiveness and serve as an important cost parameter[99]. Some authors assume that it represents the size of the heat exchanger, and perform optimization on the conductance value [100, 48]. The conductance of heat exchanger (UA value) can be calculated as:

$$UA = \frac{\dot{Q}_{actual}}{LMTD} \quad (5.19)$$

where \dot{Q}_{actual} is the heat duty of the heat exchanger and can be found from either cold or hot side of the heat exchanger using the nominator of Equation 5.17.

The heater is the place where the fuel is burned and some of the thermal energy resulting from combustion is transferred to the working fluid of the power cycle, i.e. CO_2 . Since the CO_2 is at fully critical state in sCO₂ cycles, no phase change occurs in the heater. There are two methods to determine the energy efficiency of the heater, namely direct and indirect methods. The direct boiler efficiency, η_{boiler} , is used in this thesis and expressed as:

$$\eta_{boiler} = \frac{\dot{Q}_{useful}}{\dot{Q}_{input}} = \frac{\dot{m}_{CO_2} (h_4 - h_3)}{\dot{m}_{fuel} HV_{fuel}} \quad (5.20)$$

where HV_{fuel} is the heating value of the fuel and can either be taken as lower heating value (LHV) or higher heating value (HHV) depending on the phase of the water at the outlet of the heater.

The thermal efficiency of the sCO₂ cycle, η_{CO_2} is found as:

$$\eta_{CO_2} = \frac{\dot{W}_{net}}{\dot{Q}_{useful}} = \frac{\dot{W}_{out} - \dot{W}_{in}}{\dot{m}_{CO_2} (h_4 - h_3)} \quad (5.21)$$

where \dot{Q}_{useful} is the heat supplied to the sCO₂ cycle.

5.2 Design of the Hybrid Power Plant

In this thesis, the existing Kızıldere-1 Single Flash GEPP is hybridized through a biomass driven sCO₂ topping cycle. The modeling of both bottoming steam Rankine and topping sCO₂ cycle is done using the simulation software EBSILON®Professional. In this section, the procedure regarding the design of the hybrid power plant is explained in further detail.

5.2.1 Model Verification

Upon signing an NDA with Zorlu Energy, the operational data of the Kızıldere-1 (KZD-1) GEPP is shared with METU. Based on the shared data, the modeling of the KZD-1 is done in EBSILON, and later verified by Zorlu Energy.

The overall scheme of the KZD-1’s EBSILON model and its T-s diagram are presented in Figure 5.4 and 5.5, respectively. Note that KZD-1 uses multiple production wells, each at a slightly different condition. Therefore, multiple State 1 exists compared to the T-s diagram of a generic single flash GEPP in Figure 5.1.

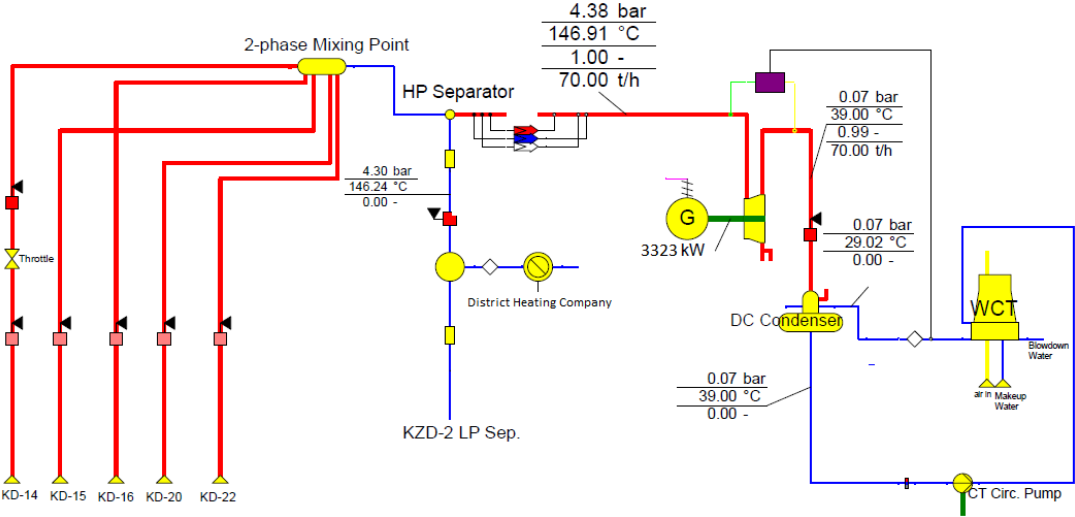


Figure 5.4: EBSILON model of KZD-1 GEPP.

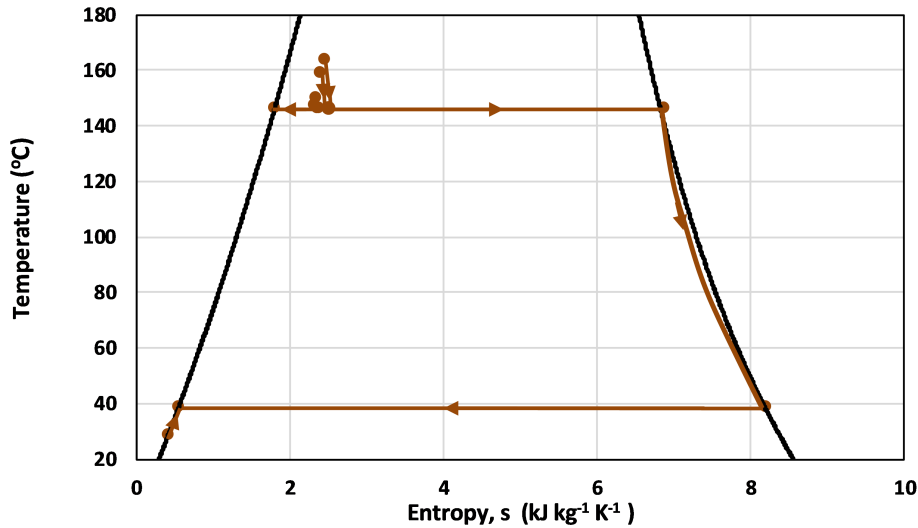


Figure 5.5: T-s diagram of the KZD-1 model.

Note that the power output of the turbine for the current operation of KZD-1 is 3.3 MWe, which is far below its rated output of 17.8 MWe. There are two reasons led to this poor power production. First, the steam mass flow rate fed to turbine is 70 ton/h (19.45 kg/s), almost half of the turbine maximum capacity of 42.42 kg/s [101]. Second, the isentropic efficiency of the turbine is currently 28% based on the basic thermodynamic calculations that are verified by Zorlu Energy. Considering that the KZD-1 is Turkey's first geothermal site commissioned in 1984 and operating for almost 40 years, the isentropic efficiency of the turbine might decay significantly. It is worth to mention that the isentropic efficiency of KZD-1 turbine is reported as 71.2% in a 2004 study by Gokcen et. al. [101]. Nevertheless, the reasons caused low isentropic efficiency at KZD-1 turbine are out of scope of this thesis.

Although it is not possible to verify the proposed hybrid power plant model due to its novelty, a standalone sCO_2 cycle is modeled in EBSILON and verified using the RC cycle proposed by Utamura [40]. Using the design conditions in Table 2.3 for components and the same inlet states for compressor and turbine in their T-s diagram, the verification model presented in Figure 5.6 is created using EBSILON, and compared with the T-s diagram supplied by Utamura in Figure 5.7 [40]. The thermal efficiency of 45.2% is achieved for the verification model which is in line with the maximum 45% thermal efficiency of Utamura. Overall, the verification results build confidence in the robustness of the further EBSILON models.

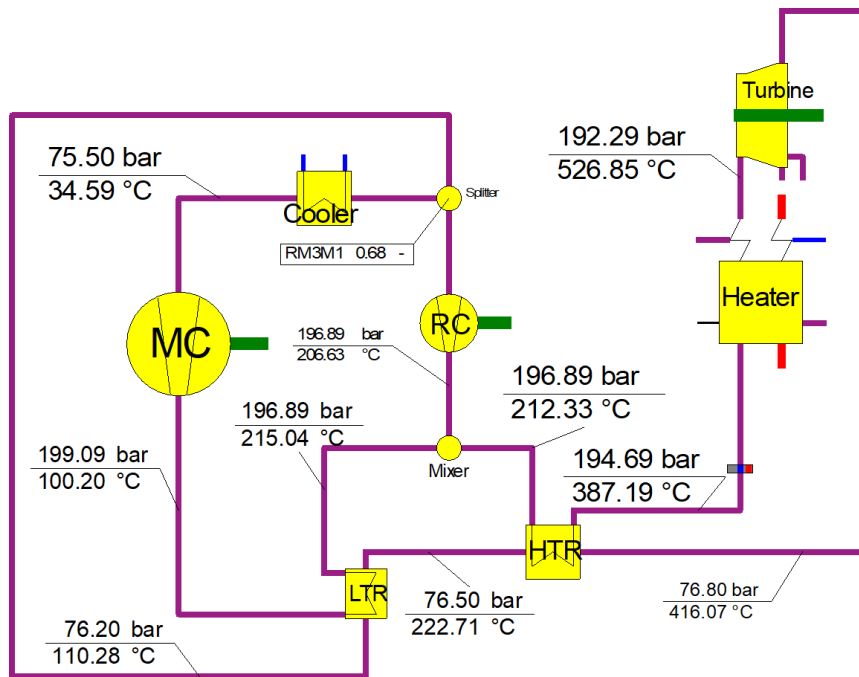


Figure 5.6: Verification model with design conditions of Utamura[40].

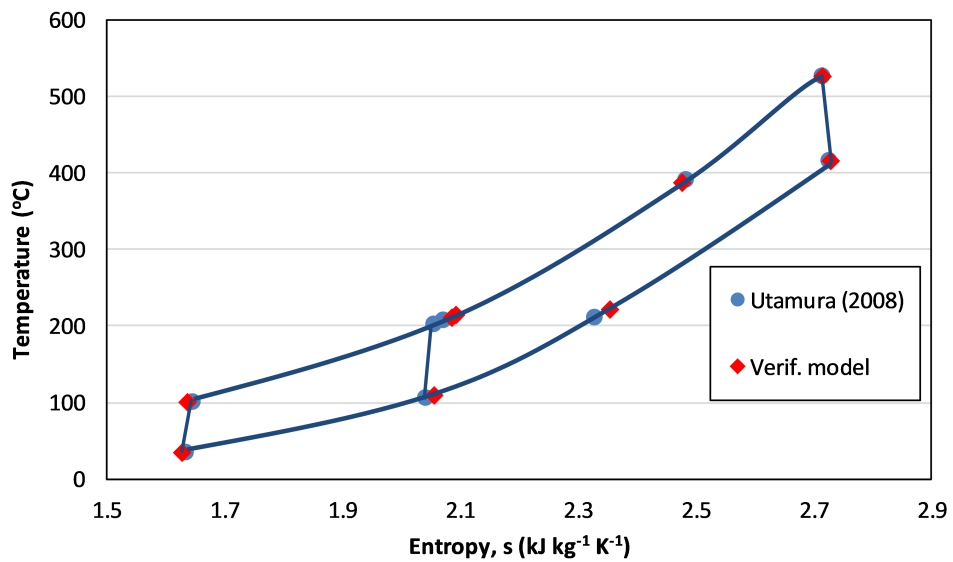


Figure 5.7: T-s diagram for the verification model and Utamura [40].

5.2.2 Design Parameters of the Hybrid Model

The 28% isentropic efficiency of KZD-1 turbine is so low that the turbine expansion process at T-s diagram of the KZD-1 (Figure 5.5) follows almost the saturation curve of water, where 99% quality is achieved at the steam exhaust. Considering that this turbine efficiency poorly represents the single flash GEPPs, a new, dry isentropic efficiency for KZD-1 turbine is defined as 85% in order to make the efforts to hybridize a single flash GEPP meaningful. A dry efficiency of 85% is selected since this value is typical for geothermal steam turbines as mentioned by DiPippo [97]. After using Equation 5.7 for KZD-1, this isentropic efficiency is converted into 80%, which is in line with the typical isentropic efficiency of geothermal steam turbines [102]. Note that in reality, the isentropic efficiency of steam turbines vary with respect to steam inlet conditions such as steam mass flow rate, temperature, and pressure. However, a single value of 80% isentropic efficiency is used hereafter to calculate the power output of KZD-1 turbine. For the hybridization scenarios discussed in following sections, it is assumed that the KZD-1 turbine is replaced with a brand-new geothermal steam turbine having 80% isentropic efficiency. The power output of the KZD-1 turbine is calculated and updated as 9.5 MWe.

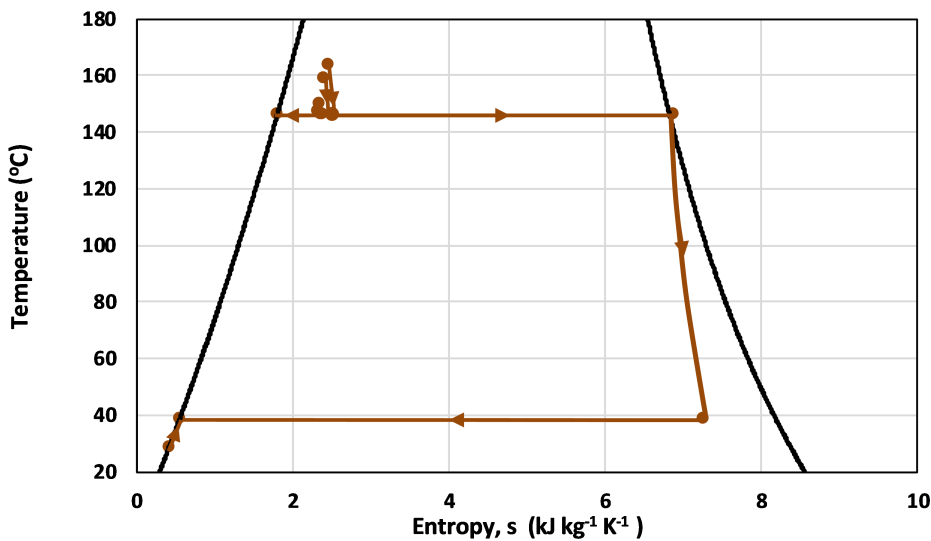


Figure 5.8: Modified T-s diagram of KZD-1 with 80% turbine isentropic efficiency.

After the two standalone cycles (steam Rankine and sCO₂) are modeled and verified, the question arises, "how can two completely different cycles with different heat

sources actually be coupled?". The initial idea of coupling two cycles (topping sCO₂ and bottoming steam Rankine) through the heat exchanger, i.e. topping cycle cooler, where the bottoming cycle is used as the heat sink as in the study of Bonyadi et. al. [49] is not completely possible given the circumstances. First of all, the corrected net power output of KZD-1 according the new turbine efficiency (9.3 MWe) is approximately half of its rated capacity (17.8 MWe) [101]. Therefore, supposing that the KZD-1 output is desired to be doubled only by using the rejected heat from the topping cycle to the bottoming cycle, the scale of the topping cycle must be enormous (>50 MWe) especially if the limited conversion efficiencies of the GEPPs due to low turbine inlet temperatures (<160 °C) are considered. Secondly, if coupling between two cycles is considered through the heat exchanger, i.e. cooler of the topping cycle, the inlet state of CO₂ to the main compressor is highly susceptible to the changes in the cold side (water) flowrate for a fixed effectiveness or pinch-point of the cooler. In other words, as more heat (by means of \dot{m}_{H_2O}) is rejected from topping sCO₂ cycle to the bottoming steam Rankine cycle through the cooler of the topping cycle under a certain pinch-point or effectiveness condition of the coupling heat exchanger, the compressor inlet temperature of CO₂ increases for a fixed CO₂ flowrate. This behaviour is extremely undesirable, since the whole point of sCO₂ cycles is to minimize the compression work by taking advantage of the thermophysical properties of CO₂ at the vicinity of its critical temperature. The negative effect of compressor inlet temperature on the compression work and the thermal efficiency becomes more profound at compression inlet temperatures above 50 °C. Thus, another solution for the coupling of two cycles is needed.

As discussed earlier, the external heat addition to the sCO₂ cycles are being done between a high temperature interval mainly due to the highly recuperative characteristics of the sCO₂ cycles. In order to overcome this problem, the sCO₂ cycles are used in cascaded manner, either in sCO₂-sCO₂, or in sCO₂-tCO₂ configurations [64, 59, 60, 61, 103, 104, 105]. Inspired from these studies, the external heat supplied by the biomass combustion can be utilized such that it is first transferred to the sCO₂ cycle (by means radiative heat transfer), while the remaining is utilized in the bottoming Steam rankine cycle (by means of both radiative and convective heat transfer). In the light of these, a novel configuration to hybridize geothermal steam Rankine cycle

with a biomass driven sCO₂ cycle is proposed in Figure 5.9.

For the proposed hybrid power plant configuration, it should be noted that the existing bottoming geothermal steam Rankine cycle is not modified except for the addition of two components, mixer and splitter (State 10 and 12). The existing bottoming geothermal cycle is, in fact, not cyclic, but instead an open cycle since all of the geothermal steam is lost as water vapor through the WCT eventually. However, the parts of the geothermal power plant subjected to hybridization (steam turbine, mixer and splitter) forms a bottoming cycle with the addition of the dry cooling system and biomass heater. The heat transfer fluid for the hybridization is taken from the basin of the KZD-1 WCT (State 15). Note that this heat transfer fluid, i.e. cooling water (at 1 bar and 29 °C) is used in closed-loop since the same flowrate is extracted through the splitter at State 12, and sent back to the basin of the WCT where it is originally taken from at its original temperature and pressure. In fact, the source of this water is not very crucial considering that it is fed back at the same conditions to its original source. Alternatively, it can also be taken from a nearby river, e.g. Büyük Menderes River, assuming the river has sufficient and reliable flow.

The cooling water (State 15) is first pumped to a pressure slightly higher than the turbine inlet pressure of the bottoming cycle to account for the subsequent pressure losses (State 16), then sensibly preheated through the cooler using the rejected heat from the topping sCO₂ cycle. The preheated water at State 17 is evaporated (State 18) with the radiation from the combustion and the convective heat transfer from the flue gas before it is fed to the KZD-1 steam turbine (State 10). After passing through the turbine, the biomass sourced fraction of the exhaust steam is extracted through the splitter (State 12), condensed and sensibly cooled via the dry cooling system before it is poured into the basin of the WCT. The partial extraction of steam exhaust and its dry cooling are particularly done due to considerable water consumption of KZD-1 GEPP (>20 kg per kWe). For the current operation of the KZD-1 GEPP, more than 95% of the geothermal steam is lost as water vapor through the WCT while the rest is directed to blow down.

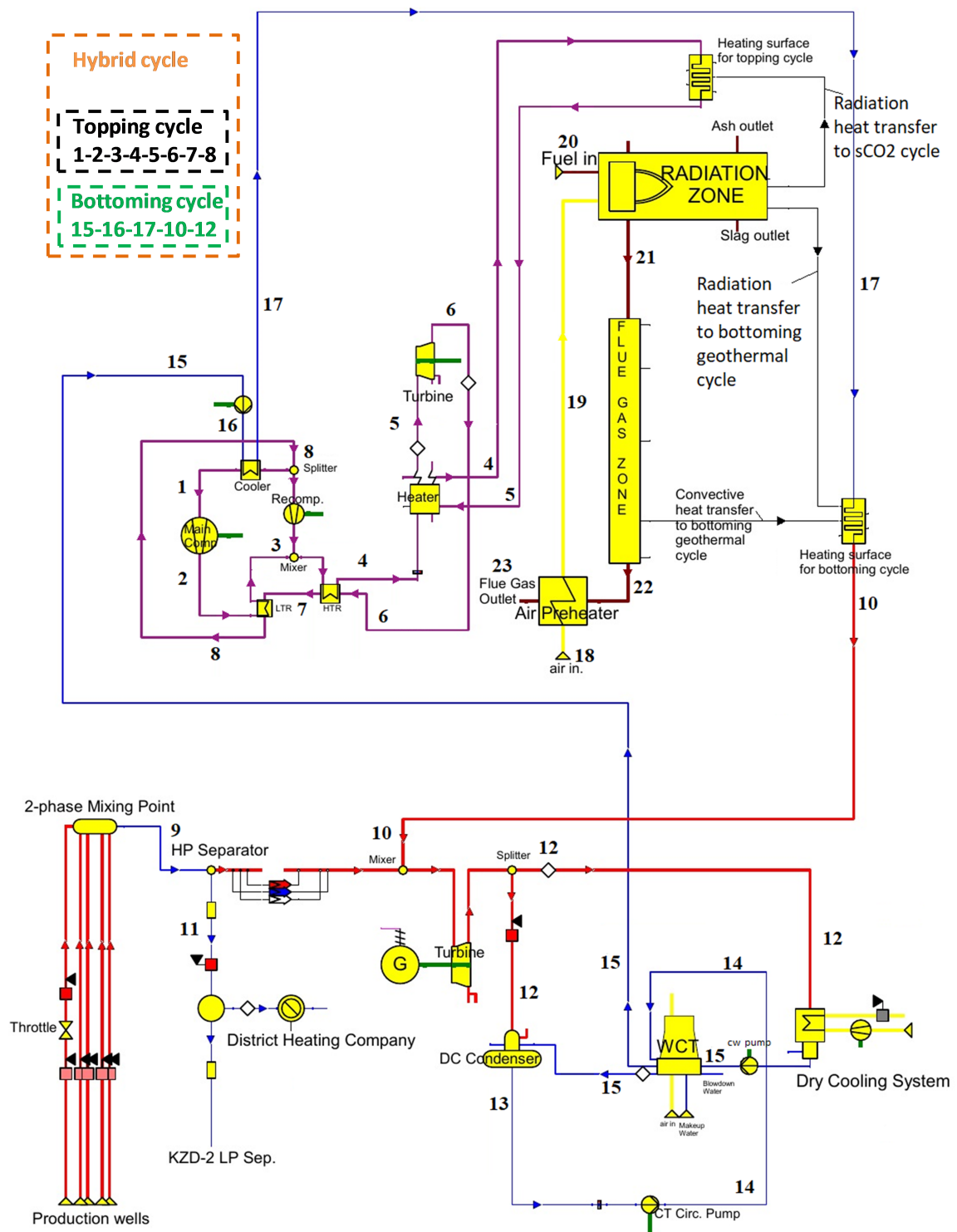


Figure 5.9: Proposed hybrid power plant configuration.

The distinction between the two terms, the hybrid power plant and the hybrid cycle should be specified for better interpretation of the results that are discussed in following chapter. The hybrid plant refers all the components and substances presented in Figure 5.9, whereas the hybrid cycle refers the combination of topping and bottoming cycle. The distinction between the bottoming cycle and KZD-1 GEPP should also be specified as two concepts differ from each other. The bottoming cycle (with State points 15-16-17-10-12) interacts with the KZD-1 GEPP when two streams of steam vapor are mixed (State 10) before they pass through the KZD-1 steam turbine. This co-occurrence lasts until the biomass heated portion of the steam exhaust is extracted through the splitter at State 12. Note that the existing components and the working conditions of the KZD-1 GEPP remain unchanged during the hybridization. Although the power output of the KZD-1 turbine is increased due to increased steam flow rate, this increased power output is later distributed hypothetically between KZD-1 GEPP and bottoming cycle. The combination of the existing KZD-1 GEPP, hybrid cycle (topping+bottoming), and the heater forms the hybrid plant.

The topping sCO₂ cycle used for hybridization is adapted from the work of Utamura [40]. The turbine inlet condition is fixed at 550 °C and 200 bar in order to be parallel with the designs in the literature. Note that these turbine inlet conditions are quite common in the literature for RC sCO₂ cycles [42, 104, 105, 106, 64, 107, 108, 109]. Generally in commercial boilers, the temperature of the tubes is controlled by the working fluid (water) flow to stay below 650 °C in order to protect the material integrity of the boiler tubes [62]. Although specific materials such as 617, 230, 740H nickel alloys can withstand higher pressures and temperatures, they are quite expensive compared to conventional boiler materials. Therefore, in order to provide more freedom in terms of the material selection for the heater-boiler of the hybrid power plant, the turbine inlet temperature is limited and fixed at 550 °C.

Currently, the steam mass flow rate of KZD-1 is 19.45 kg/s (70 ton/h) as shown in Figure 5.4, and the net power output of the KZD-1 GEPP is 9.3 MWe if the modified turbine isentropic efficiency of 80% is taken into account. The additional cooling water flowrate that is to be preheated, and eventually evaporated by biomass sourced heat is the decision to be made carefully. For this purpose, a two-dimensional parametric analysis with three-dimensional output is conducted and presented in Figure 5.10.

Note that these two parameters are the mass flow rate of the cooling water subjected to hybridization, and the mass flow rate of the working fluid (CO_2) of the topping cycle. These two flow rates can be considered as the two most important parameters of the hybrid cycle since their values define the key concepts such as the the power output and the thermal efficiencies. The output matrix is defined for 4 parameters, namely the net power output of the hybrid plant, net power output of the topping cycle, the thermal efficiency of the topping cycle, and the thermal efficiency of the hybrid cycle. The rated output of the KZD-1 GEPP plant is 17.8 MWe [101, 97]. The net total power production of the hybrid plant therefore should be limited by this value since the license granted to the power plant investor is possibly limited by it. On the other hand, the net power output of the topping cycle is a factor that is directly proportional to the investments costs. In other words, as the scale of the topping cycle increases, the additional components to be bought for the hybridization become more costly. Therefore, the topping cycle is desired to be kept as small as possible. However, the thermal efficiency of the hybrid cycle tends to decrease as the ratio of cooling water mass flow rate to CO_2 mass flow rate increases. This behaviour is visible on the far right tip of Figure 5.10d where the thermal efficiency of the hybrid cycle exhibits a minima. The underlying theory leading this result is the standalone efficiencies of the topping and the bottoming cycles. Assuming both cycles rejecting heat at the same temperature isothermally, the Carnot efficiency of the topping cycle would always be higher than that of the bottoming cycle due to higher turbine inlet temperature (TIT). Since the mass flow rate of the topping cycle is directly proportional to the power output of the topping cycle, a trade-off between the investment costs and hybrid thermal efficiency emerges. In short, the two mass flow rates (H_2O and CO_2) should be adjusted such that the net power output of the hybrid plant is kept close but below the rated output of the original GEPP, while retaining good hybrid thermal efficiency and smaller topping cycle. Note that the thermal efficiency of the standalone topping sCO₂ cycle (Figure 5.10b) is not presented as a decision parameter but as an indicator to monitor the deviation from the optimum compression temperature of the topping cycle. For the conducted parametric analysis the base inputs are presented in Table 5.1.

For clarification, the mathematical definition of 4 output parameters in conducted

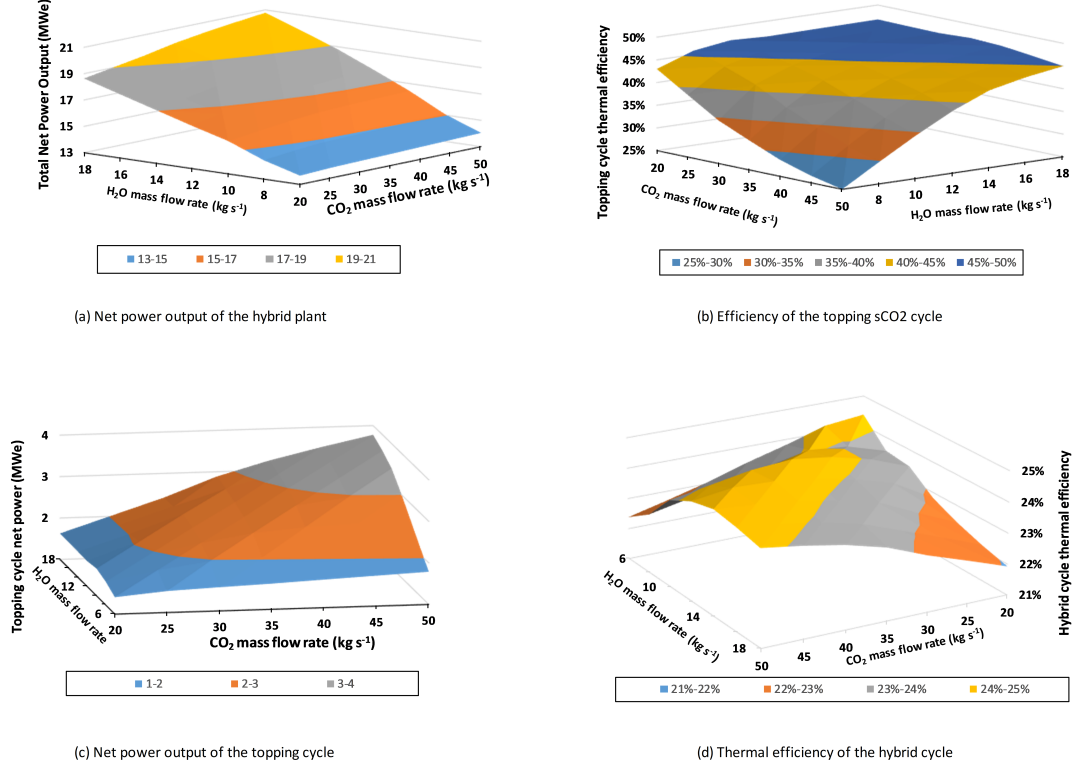


Figure 5.10: Results of the parametric analysis on H_2O and CO_2 mass flow rates.

two-dimensional parametric study (Figure 5.10) along with additional key parameter indicators (KPIs) which are presented in following results chapter at Table 6.3 should be given. The total net power output in Figure 5.10a ($P_{net,total}$) refers the overall net power output of the hybrid plant, i.e. the combination of KZD-1 GEPP and hybrid (topping+bottoming) cycle, as follows:

$$P_{net,total} = P_{net,KZD-1} + P_{net,topping} + P_{net,bottoming} \quad (5.22)$$

where $P_{net,KZD-1}$, $P_{net,topping}$, and $P_{net,bottoming}$ are the net power output of KZD-1 GEPP, topping and bottoming cycle, respectively. These three terms are also formulated as:

$$P_{net,KZD-1} = P_{turbine,KZD-1} - P_{auxillary,KZD-1} \quad (5.23)$$

$$P_{net,topping} = P_{turbine,topping} - P_{MC,topping} - P_{RC,topping} \quad (5.24)$$

$$P_{net,bottoming} = P_{turbine,bottoming} - P_{auxillary,bottoming} \quad (5.25)$$

where auxiliary term for KZD-1 refers the power consumption of the cooling water circulation pump operating between DC condenser and WCT. Similarly, the auxiliary term for bottoming cycle includes the power consumption of the pumps used to circulate the cooling water subjected to hybridization along with the power consumption of the dry cooling system. In fact, the biggest contribution to this term results from the latter. The subscripts MC and RC in Equation 5.26 refer the consumption of main compressor and recompressor in the topping sCO₂ cycle, respectively.

In parallel with the net power outputs, the thermal efficiencies for the topping, bottoming, and hybrid cycle are formulized as:

$$\eta_{topping} = \frac{P_{net,topping}}{\dot{Q}_{top,in}} = \frac{P_{net,topping}}{\dot{m}_{CO_2} (h_5 - h_4)} \quad (5.26)$$

$$\eta_{bottoming} = \frac{P_{net,bottoming}}{\dot{Q}_{bot,in 1} + \dot{Q}_{bot,in 2}} = \frac{P_{net,bottoming}}{\dot{m}_{H_2O} (h_{17} - h_{16}) + \dot{m}_{H_2O} (h_{10} - h_{17})} \quad (5.27)$$

$$\eta_{hybrid} = \frac{P_{net,topping} + P_{net,bottoming}}{\dot{m}_{CO_2} (h_5 - h_4) + \dot{m}_{H_2O} (h_{17} - h_{16}) + \dot{m}_{H_2O} (h_{10} - h_{17})} \quad (5.28)$$

In addition to the thermal efficiencies, biomass-to-electricity efficiency, η_{b-to-e} , can be defined by multiplying the direct boiler efficiency, η_{boiler} , with the hybrid thermal efficiency, η_{hybrid} , or alternatively calculated using:

$$\eta_{b-to-e} = \frac{P_{net,hybrid}}{\dot{Q}_{input}} = \frac{P_{net,topping} + P_{net,bottoming}}{\dot{m}_{fuel} LHV_{fuel}} \quad (5.29)$$

Note that the direct boiler efficiency (η_{boiler}) definition in Section 5.1.2 is given for the standalone sCO₂ cycle, and should be modified for the hybrid cycle as:

$$\eta_{boiler} = \frac{\dot{m}_{CO_2} (h_5 - h_4) + \dot{m}_{H_2O} (h_{17} - h_{16}) + \dot{m}_{H_2O} (h_{10} - h_{17})}{\dot{m}_{fuel} LHV_{fuel}} \quad (5.30)$$

Considering the trade-off between the thermal efficiency of the hybrid cycle and the additional investment costs for the hybridization, the flow rates are selected for CO₂ and the cooling water as 45 kg/s and 12 kg/s, respectively. This flow rate pair provides the maximum possible hybrid thermal efficiency of 22.4% while keeping the power output of the topping cycle at 2.9 MWe. The power output of the hybrid plant for the selected flow rate pair is 17.5 MWe.

Table 5.1: Base inputs for the parametric analysis on the flow rates.

Equipment	Parameter	Unit	Value
Compressors	Isentropic efficiency	92	%
Pumps	Isentropic efficiency	80	%
CO ₂ Turbine	Isentropic efficiency	92	%
	Expansion ratio	2.51	-
Steam Turbine	Isentropic efficiency	80	%
Recuperators	Effectiveness	96	%
	Cold side pressure drop	2.2	bar
	Hot side pressure drop	0.3	bar
Heater	Pressure drop	2.4	bar
Cooler	Effectiveness	80	%
	Cold side pressure drop	0.1	bar
	Hot side pressure drop	0.6	bar
Splitter	Part-flow ratio	0.68	-

After the flow rates are decided, the two values from the base inputs, namely the part-flow ratio and the turbine expansion ratio for the topping cycle can be optimized. Note that the optimum values for the part-flow and turbine expansion ratio are found

by Utamura as 0.68 and 2.51, respectively [40].

The part-flow ratio is varied from 0.4 to 1 in even 0.02 increments while the turbine expansion ratio is changed from 2.5 to 3.5 by the increments of 0.1. All other inputs except for these two ratios are kept constant and equal to the values in Table 5.1.

The optimum part-flow ratio appears at 0.5 and stays steadily until 0.8 as depicted in Figure 5.11. The design value is therefore selected as 0.7, which is consistent with Utamura's optimum value of 0.68.

Similarly, the turbine expansion ratio makes a peak for the hybrid thermal efficiency at 2.6, and stays steadily until it reaches 3.4 as shown in Figure 5.12. However, this ratio controls the pressure at the turbine exhaust directly while the temperature at the turbine exhaust is affected indirectly. Since the state at the turbine exhaust forms a boundary condition for the recuperation process, the heat duty and the size of the heat exchangers, namely HTR and LTR, are affected by the pressure ratio. Assuming that UA value (heat transfer conductance in kW/K) for these two heat exchangers represents the size of the heat exchangers, one can observe the effect of pressure ratio on the size of the heat exchangers in Figure 5.13. In addition to the size, the heat duty of the recuperators are presented in Figure 5.14. Taken these two additional output parameters (heat exchanger size and heat duty) into account, the optimum expansion ratio is selected as 3 in order to achieve smaller LTR size, evenly distributed heat duty among the recuperators while retaining good thermal efficiency for the hybrid cycle.

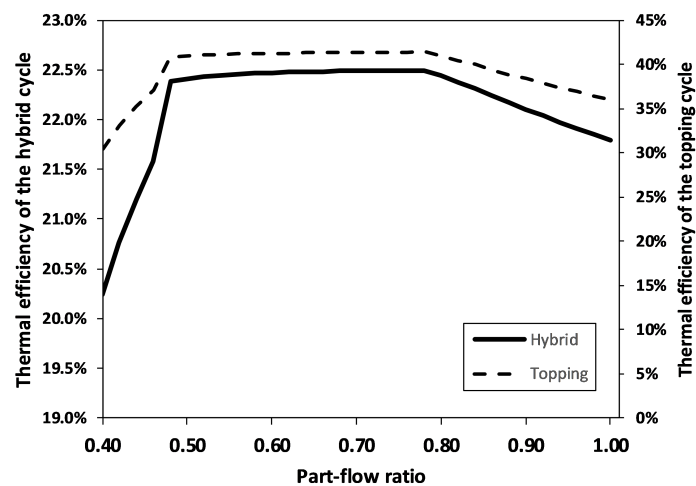


Figure 5.11: Trends in thermal efficiencies with variations in part-flow ratio.

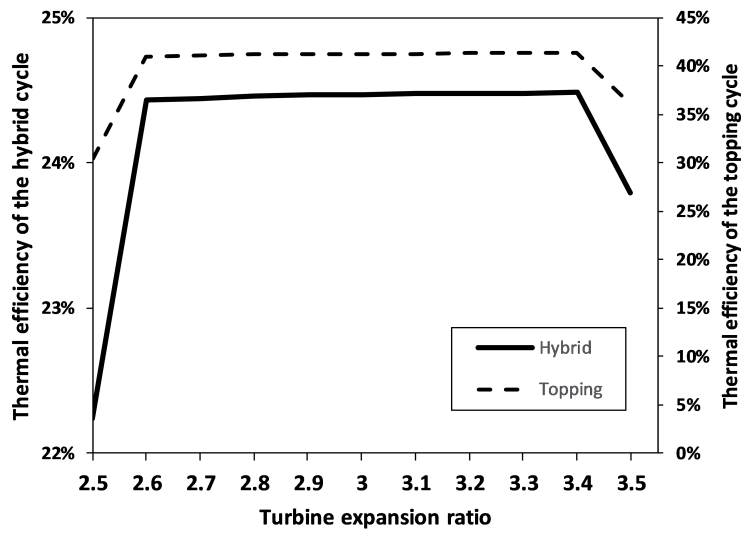


Figure 5.12: Effect of turbine expansion ratio on the thermal efficiency.

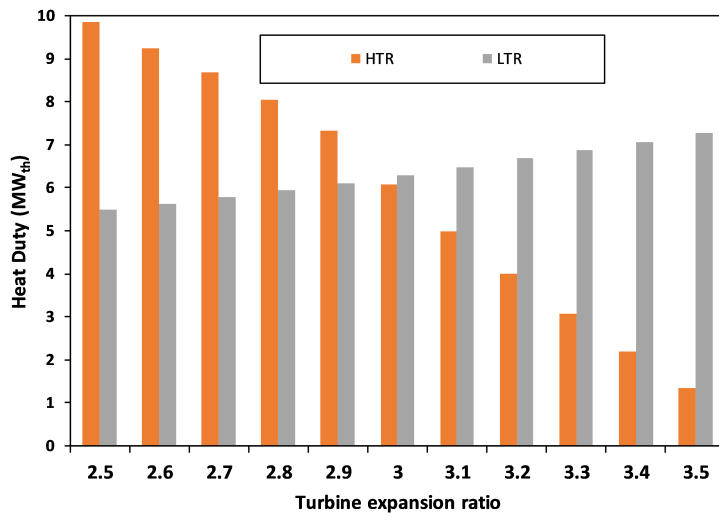


Figure 5.13: Effect of turbine expansion ratio on the heat duty of recuperators.

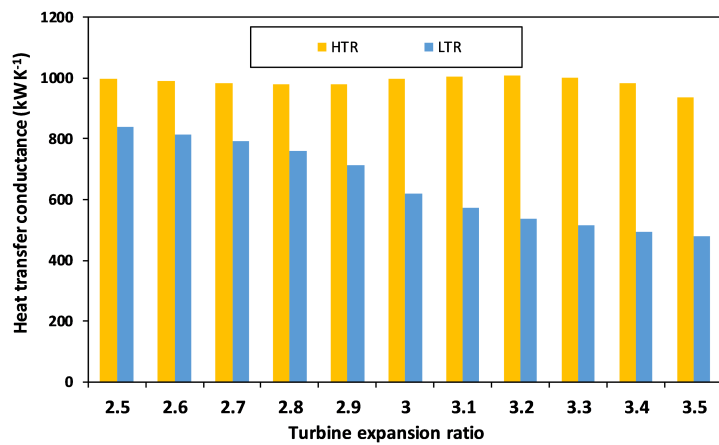


Figure 5.14: Effect of turbine expansion ratio on the size of the recuperators.

Upon the two parameters, part-flow ratio and turbine expansion ratio, are concluded as 0.7 and 3, respectively, the net power output of the hybrid plant increases to 17.8 MWe. The thermal efficiency of the hybrid cycle for the optimized case becomes 24.5%.

Since two working fluids (water and CO_2) are to be heated up in the same heater, a novel boiler-heater design is necessary to finalize the hybrid power plant configuration. In parallel to the work of Manente and Lazzaretto [64], HHV of the fuel is converted into LHV using the empirical formula:

$$LHV = HHV(1 - w) - 2.444 w - 2.444 H - 8.936 (1 - w) \quad (5.31)$$

where w and H are the mass fractions of moisture and hydrogen, respectively.

Using the as received moisture content, 7.5%, from Table 3.1, LHV of the studied OR is calculated as 17.5 MJ/kg (wet basis).

The schematic of the heater, which is developed and modeled in EBSILON, is presented in Figure 5.15 having state numbers compatible with Figure 5.9. Note that the proposed heater configuration in Figure 5.15 is the modified version of the radiative-convective counter-current boiler from the work of Manente and Lazzaretto which demonstrated the best energy conversion efficiency among the other boiler configurations [64].

EbsBoiler module of EBSILON is used to calculate the flue gas composition and combustion temperature under the complete combustion condition for the excess air ratio (λ) of 1.5. Note that the excess air for most of the biomass fuels is normally set to 25% or above [110]. Therefore, the presumed value of 1.5 is both reasonable, and consistent with the design value of Manente and Lazzaretto. The flue gas temperature in biomass furnaces is generally kept below 1000 °C, and the temperature control of the flue gas is done either by increasing the excess air ratio (λ) (at the cost of having lower boiler efficiency) or by the recirculation of the flue gas inside the furnace [64]. In the proposed heater configuration, the temperature of the flue gas is controlled by the quality of the cooling water at the radiative outlet of the heater. Note that for the proposed heater configuration in Figure 5.15 (or in 5.9), the sCO_2 and the preheated

cooling water are heated in the radiative section of the heater, then the evaporation of the cooling water is completed using the heat from the flue gas (convective section). The quality of the cooling water at the intermediate stage between the radiative and convective section determines both the flue gas temperature and the distribution of the heat transfer for radiation and convection. In other words, the design of the heater is done such that the heat addition to the topping sCO₂ cycle (between States 4 and 5) is completely done by means of radiation in the the radiative section of the heater. In addition, radiative section provides just enough heat transfer to the preheated water at State 17 to bring it to a specific steam quality. This intermediate steam quality determines the flue gas temperature and the rest of the convective heat transfer which is ultimately used to bring the water to quality of 1 at State 10.

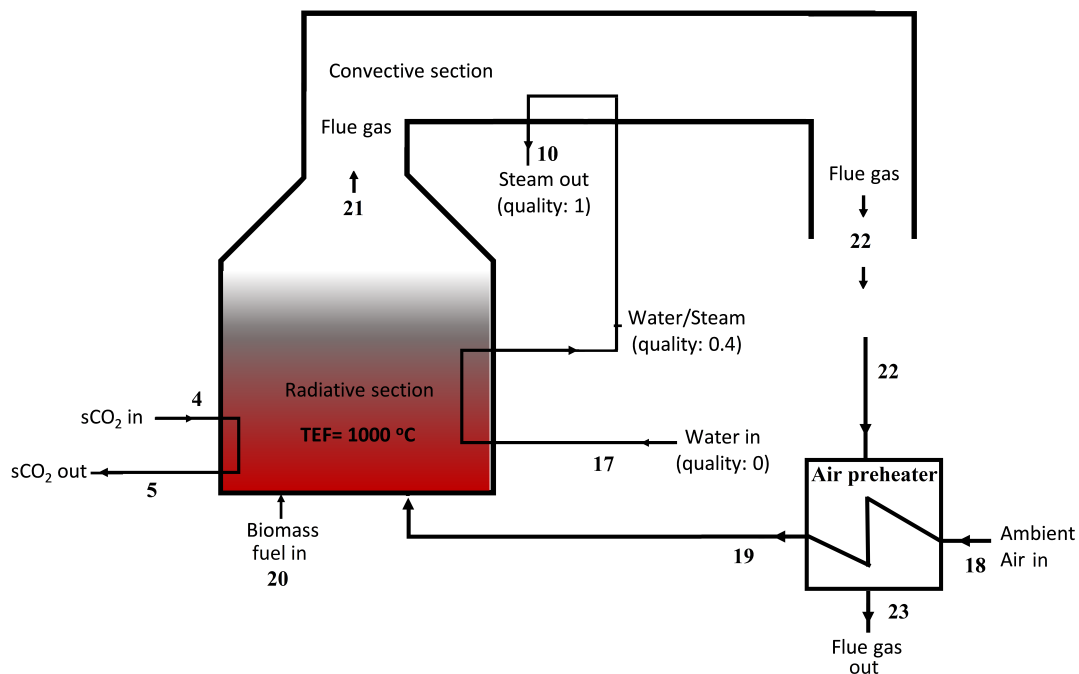


Figure 5.15: Radiative-convective counter-current heater configuration.

A verification combustion model is created in EbsBoiler module of EBSILON for the different cases in the study of Manente and Lazzaretto [64]. The verification of the results are presented in Table 5.2 for 1 kg/s woody biomass fuel used in their work.

The combustion model in EBSILON for the studied OR and the proposed heater is assumed to be done correctly considering the maximum absolute error of 2.3% in Table 5.2.

Table 5.2: Model verification results based on the model of Manente and Lazzaretto[64].

	Inputs		Outputs					
	λ	T _{air} (°C)	T _{flue gas} (°C)	m _{flue gas} (kg s ⁻¹)	X _{CO2}	X _{H2O}	X _{N2}	X _{O2}
Verification values								
	1.5	20	1405	8.225	0.1826	0.0754	0.6738	0.0682
		100	1457					
	2.37	20	1000	12.41	0.1211	0.0499	0.7053	0.1237
	2.56	100	1000	13.33	0.1127	0.0465	0.7095	0.1313
Model output								
	1.5	20	1407	8.273	0.1820	0.0749	0.6752	0.0679
		100	1458.6					
	2.37	20	999.9	12.49	0.1230	0.0496	0.7065	0.1209
	2.56	100	1000.7	13.41	0.1125	0.0462	0.7107	0.1306
Error: (Model-Verif)/Verif			0.1%	0.6%	-0.3%	-0.7%	0.2%	-0.4%
			0.1%					
			0.0%	0.6%	1.6%	-0.6%	0.2%	-2.3%
			0.1%	0.6%	-0.2%	-0.6%	0.2%	-0.5%

In their mathematical model on boiler design, Stehlik et. al. [111] state that the boilers can be classified according to the heat-transfer mechanism either as radiative or convective, and suggest that the combustion heat can be divided approximately into three parts: radiation chamber (45%- 55%); convective sections (45%-25%); and stack and other heat losses (10%-20%). A parametric analysis is conducted on intermediate steam quality in order to observe the flue gas temperature and the heat transfer distribution in the proposed heater design. The results are presented in Figure 5.16. Note that the effective temperature of radiation (TEF) and the heat loss in the radiative section is assumed as 1000 °C and 5% respectively, in order to be consistent with Manente and Lazzaretto.

The temperature of the flue gas leaving the radiative section of the heater is inversely proportional to the intermediate steam quality as it can be observed from Figure 5.16. The underlying theory led to this result is the radiative heat transfer to the flue gas. The flue gas is subjected to less radiation as the radiation is used to increase the quality of the water. As the steam quality of 0.4 is reached, the radiation, convection and the losses account for 50.3%, 39.7%, and 10.13% and lie in the range suggested by Stehlik et. al. [111]. The temperature of the flue gas is kept at 850.3 °C at this quality. Therefore, the intermediate steam quality is concluded as 0.4 hereafter.

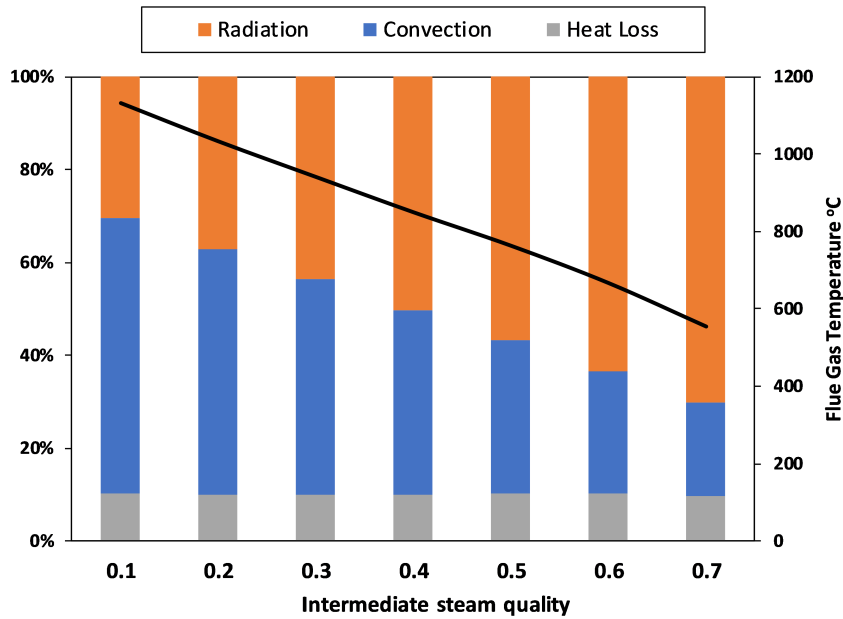


Figure 5.16: Heat transfer distribution and the flue gas temperature after the radiative section in the proposed heater with varying intermediate steam quality.

Mass flow rate, temperature and composition of the flue gas for the proposed model is presented in Table 5.3 along with the adiabatic combustion temperature. The mass flow rate of the biomass fuel (OR) in the heater is adjusted such that the temperature of the flue gas at air preheater outlet (State 23) is limited at minimum allowable temperature of 110 °C in order to prevent dew point [62]. The effectiveness of the counter-current air preheater is 70%. Under these finalized conditions, the fuel consumption in the heater is 2.2 kg/s.

Table 5.3: Flue gas mass flow rate, temperature and composition for the studied OR.

m_{fuel} (kg s ⁻¹)	λ	$T_{\text{adiabatic flame}}$ (°C)	T_{air} (°C)	$T_{\text{flue gas}}$ (°C)	$m_{\text{flue gas}}$ (kg s ⁻¹)	X_{CO_2}	$X_{\text{H}_2\text{O}}$	X_{N_2}	X_{O_2}
2.2	1.5	1581.8	180.6	850.3	21.4	0.1775	0.0623	0.6909	0.0693

CHAPTER 6

HYBRIDIZATION RESULTS

In this chapter, energetic results and the performance parameters related to proposed hybrid power plant configuration are discussed.

The procedure on determining the hybrid power plant parameters are described in Chapter 5. The heater-boiler design is done such that it satisfies both the needs of the hybrid (topping+bottoming) cycle and is parallel with the designs in literature.

The final design parameters are presented in Table 6.1 as the outcome of the optimization in Chapter 5.

Table 6.1: Optimized design parameters.

Equipment	Parameter	Unit	Value
Compressors	Isentropic efficiency	92	%
Pumps	Isentropic efficiency	80	%
CO ₂ Turbine	Isentropic efficiency	92	%
	Expansion ratio	3	-
Steam Turbine	Isentropic efficiency	80	%
Recuperators	Effectiveness	96	%
	Cold side pressure drop	2.2	bar
	Hot side pressure drop	0.3	bar
Cooler	Effectiveness	80	%
	Cold side pressure drop	0.1	bar
	Hot side pressure drop	0.6	bar
Splitter	Part-flow ratio	0.7	-
Air-preheater	Effectiveness	70	%
Heater	Excess air ratio	1.5	-
	Radiation losses	5	%
	CO ₂ pressure drop	2.4	bar
	Water pressure drop	0.1	bar

Intensive properties for thermodynamic states of 1-23 in Figure 5.9 are presented in Table 6.2 for the final design parameters.

Table 6.2: Intensive properties for States 1-23 in Figure 5.9.

State	Fluid	Pressure (bar)	Temperature (°C)	Quality	Enthalpy (kJ kg ⁻¹)
1	CO ₂	65.47	44.4	1	450.6
2	CO ₂	206.8	143.8	1	509.8
3	CO ₂	204.6	288.2	1	711.8
4	CO ₂	202.4	402.5	1	853.3
5	CO ₂	200	550	1	1035.1
6	CO ₂	66.67	418	1	890.2
7	CO ₂	66.37	293.6	1	745.0
8	CO ₂	66.07	167.5	1	604.8
9	Water	4.38	146.9	0.11	861.8
10	Water	4.38	146.9	1	2742.2
11	Water	4.38	146.9	0	618.9
12	Water	0.07	39	0.87	2253.9
13	Water	0.07	39	0	163.4
14	Water	1	39.1	0	163.5
15	Water	1	29	0	121.7
16	Water	4.58	29	0	122.1
17	Water	4.48	127.7	0	536.5
18	Air	1	20	-	20.1
19	Air	1	180.6	-	182.6
20	Fuel	1	30	-	17500
21	Flue gas	1	850.3	-	979.4
22	Flue gas	1	248	-	265.0
23	Flue gas	1	113.3	-	118.9

The energy accounting on power generation and consumption of the hybrid power plant is supplied in Table 6.3. It should be noted that although the power output from steam turbine is 15.4 MWe, 9.5 MWe can be attributed to geothermal (KZD-1) and 5.9 MWe can be attributed to the biomass powered bottoming cycle since turbine is shared by these two systems.

The energetic results are also demonstrated in Figure 6.1. Only the heat additions and net power generations are demonstrated for the sake of simplicity.

The maximum thermal efficiency of 24.5% is achieved for the hybrid cycle, while the

Table 6.3: Energy accounting for the hybrid power plant.

Parameter	Unit	Value
$P_{\text{turbine,topping}}$	MW	6.5
$P_{\text{MC,topping}}$	MW	1.9
$P_{\text{RC,topping}}$	MW	1.5
$P_{\text{net,topping}}$	MW	3.2
$P_{\text{turbine,bottoming}}$	MW	5.9
$P_{\text{compressor,bottoming}}$	MW	0.6
$P_{\text{net,bottoming}}$	MW	5.3
$P_{\text{turbine,KZD-1}}$	MW	9.5
$P_{\text{auxillary,KZD-1}}$	MW	0.2
$P_{\text{net,KZD-1}}$	MW	9.3
$P_{\text{net,total}}$	MW	17.8
η_{topping}	%	38.7
$\eta_{\text{bottoming}}$	%	16.9
η_{hybrid}	%	24.5
η_{boiler}	%	90
$\eta_{\text{b-to-e}}$	%	22
Fuel consumption	kg s^{-1}	2.2

thermal efficiency of the topping cycle and biomass-to-electricity conversion ratio are found as 38.7% and 22%, respectively. Note that the same turbine inlet conditions (550 °C and 200 bar) are used for the topping sCO₂ cycle in the study of Manente and Lazzaretto where the proposed heater design in this thesis is also adapted from [64]. Therefore, their study can be used as a reference case to compare the thermal efficiencies of the cycles and biomass-to-electricity ratio. The biomass-to-electricity conversion ratio in their study lies in the range of 28%-36% depending on the boiler design and air inlet conditions, while the efficiencies of the topping RC sCO₂ and the bottoming sCO₂ cycle are reported as 44.2% 28.3% as shown in Table 6.4.

Table 6.4: Comparison of efficiencies with those of Manente and Lazzaretto[64].

	η_{topping}	$\eta_{\text{bottoming}}$	$\eta_{\text{b-to-e}}$
Manante and Lazzaretto [64]	44.2	28.3	28-36%
This thesis	38.7	16.9	22

The first and the most important reason to hold lower biomass-to-electricity conversion ratio in this thesis is the fixed and unalterable condition of the bottoming cycle,

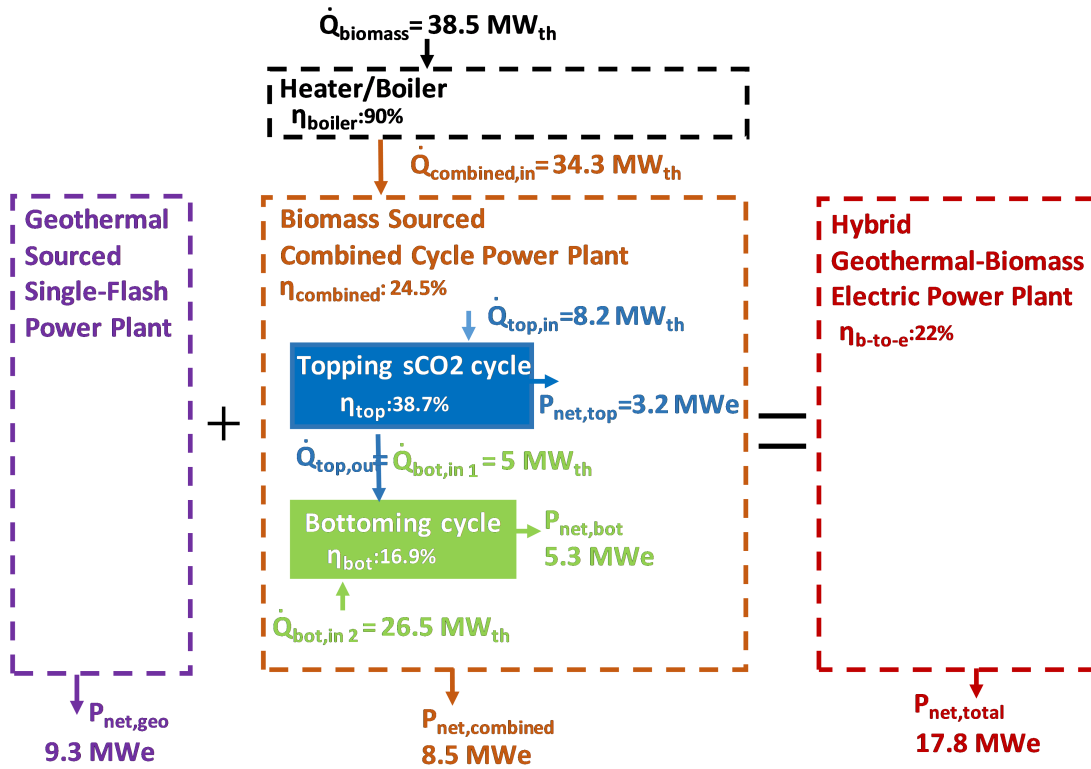


Figure 6.1: Energetic Results of Hybridized Power Plant. Note the Geothermal Sourced Single-Flash Power Plant and the Bottoming Cycle of the Biomass Sourced Combined-Cycle Power Plant share the same turbine.

i.e. the TIT of $146.9 \text{ }^\circ\text{C}$ in the steam turbine. However, in their study, Manente and Lazzaretto are capable of selecting the optimum conditions for the bottoming cycle freely. The TIT for the bottoming sCO₂ cycle in their study, for instance, is $313.9 \text{ }^\circ\text{C}$. As a result, 12.4% lower efficiency is reached in the bottoming cycle compared to their study. Second, the thermal efficiency of the topping cycle in this thesis is penalized due to deviation from optimum sCO₂ compressor inlet condition (State 1). As mentioned in previous sections, the compression work in sCO₂ cycles is minimized if the compression takes place in the vicinity of the critical point of the CO₂ at $31.8 \text{ }^\circ\text{C}$. Note that the compression inlet temperature for the topping cycle is $44.4 \text{ }^\circ\text{C}$ as reported in Table 6.2. Accordingly, the main compression process in T-s diagram of the topping cycle shifted slightly rightward in Figure 6.6. This deviation resulted from the fact that the rejected heat of the topping cycle is utilized in the bottoming cycle using the coupling heat exchanger, cooler. As the flowrate of the cooling water that is to be preheated by the cooler is increased, the temperature of the hot side outlet of the

cooler (State 1) is increased under a fixed effectiveness value of the cooler, penalizing the efficiency of the topping cycle. However, this setback is not completely unfavorable since it allows utilization of 5 MW thermal heat in the bottoming cycle. In fact, the scale of the topping cycle is desired to be as small as possible to minimize the investment costs. In relation to that, the allocation of the biomass sourced heat between the topping and the bottoming cycle is done in the favor of bottoming cycle as shown in Figure 6.2. Although this allocation is another important reason of achieving lower conversion efficiencies compared to the work of Manente and Lazzaretto, the motivation in this thesis is not reaching the best conversion efficiencies but rather using the existing components of KZD-1 (steam turbine) to the full extent and increasing the net power output of the hybrid plant to its rated output of 17.8 MWe. Note that the net power output distribution in the work of Manente and Lazzaretto is 90%-10% favoring topping cycle, while it is 62%-38% favoring bottoming cycle in this thesis.

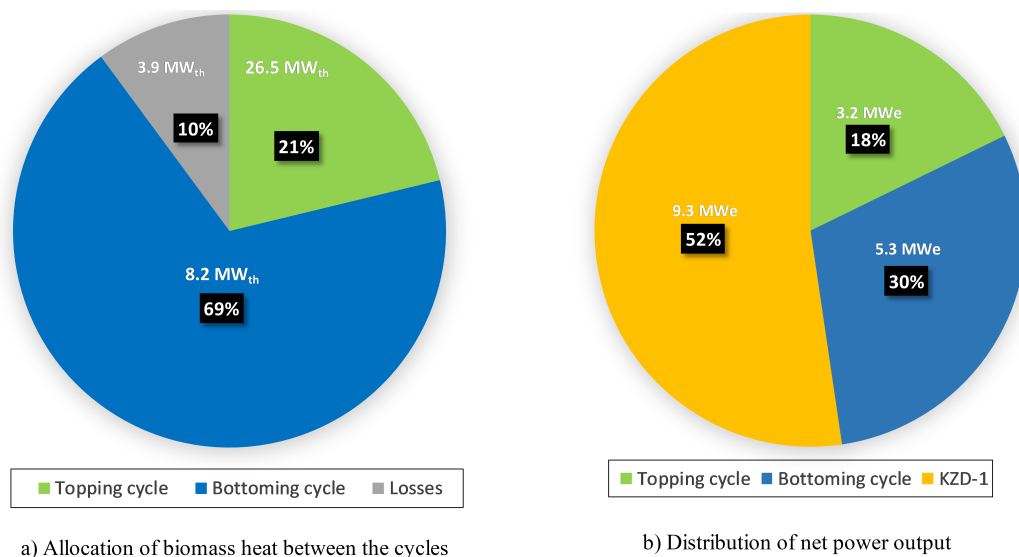


Figure 6.2: Allocation of biomass heat and power distribution between the cycles.

Although no exergy analysis is performed in this thesis, Q-T profiles of heat exchangers are presented in Figure 6.3, 6.4, and 6.5 for the heater, recuperators, and the cooler, respectively. Note that in the heater, adiabatic flame temperature (TAF) is calculated as 1581.3 °C by EBSILON, and the effective temperature of radiation (TEF) is assumed as 1000 °C.

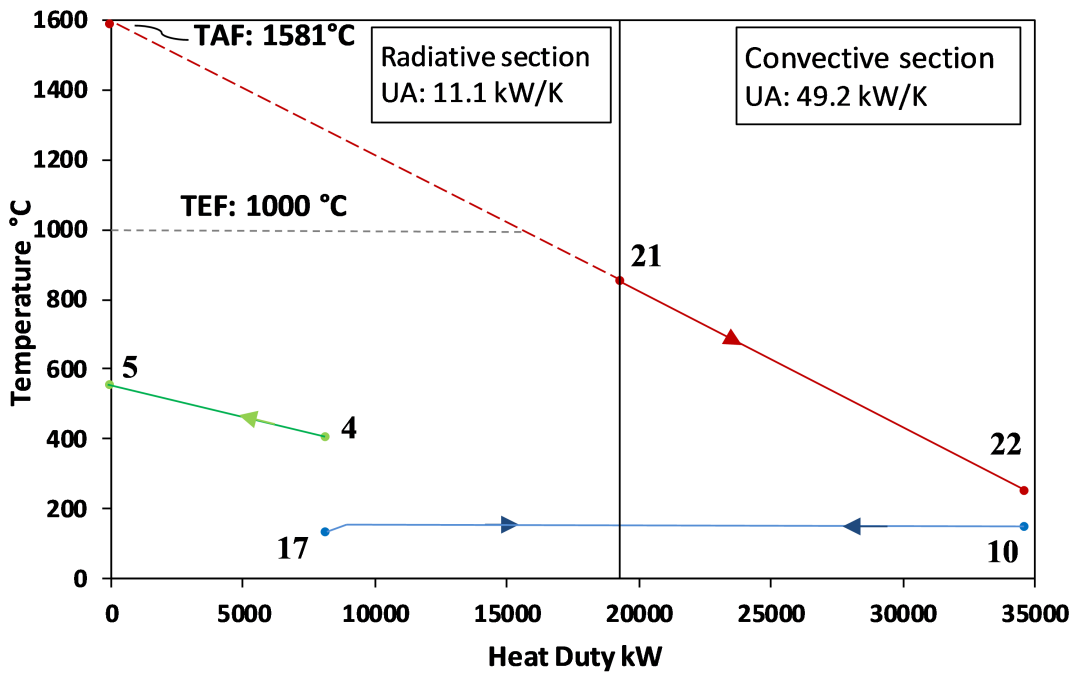


Figure 6.3: Q-T diagram of the radiative-convective heater with assumed TEF=1000°C.

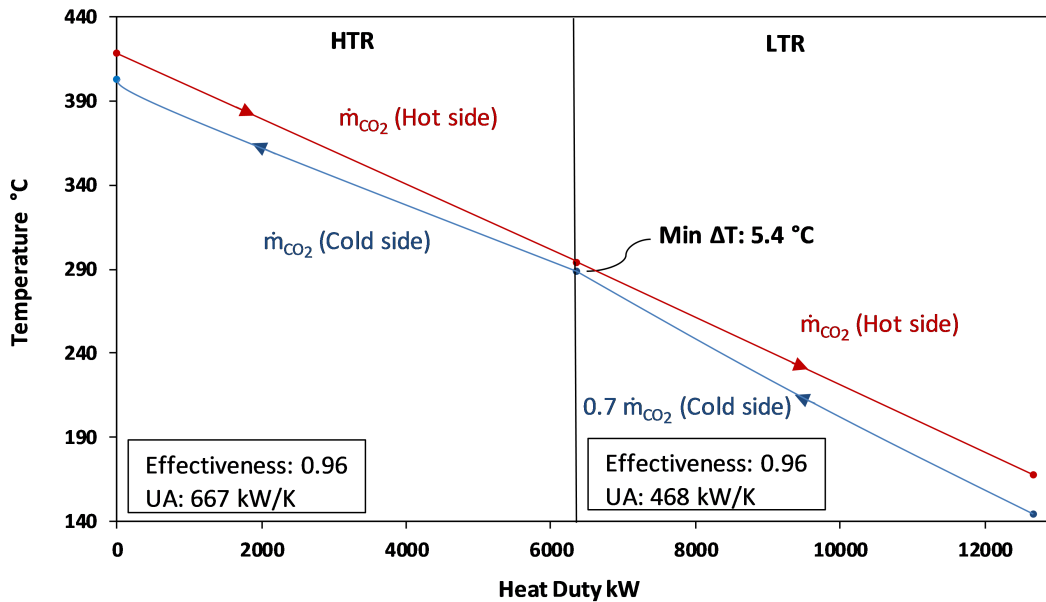


Figure 6.4: Q-T diagram of the recuperators.

For the recuperators, it is assured that no pinch problem exists, and the minimum temperature difference between two streams is kept above 5 °C with effectiveness of 96%. Good temperature matches are observed for the recuperators and the cooler. Although it is expected for recuperators to have good temperature match between cold and hot CO_2 streams due to having the same working fluid on both sides, the good temperature match on the cooler is surprisingly promising and stems from the fact that water is sensibly heated through the cooler. Having a good temperature match at the cooler possesses an extra importance since the cooler acts as a coupling mechanism between the two cycles. As a result, it can be clearly suggested that a good synergy between the topping sCO_2 and the bottoming steam Rankine cycle is observed.

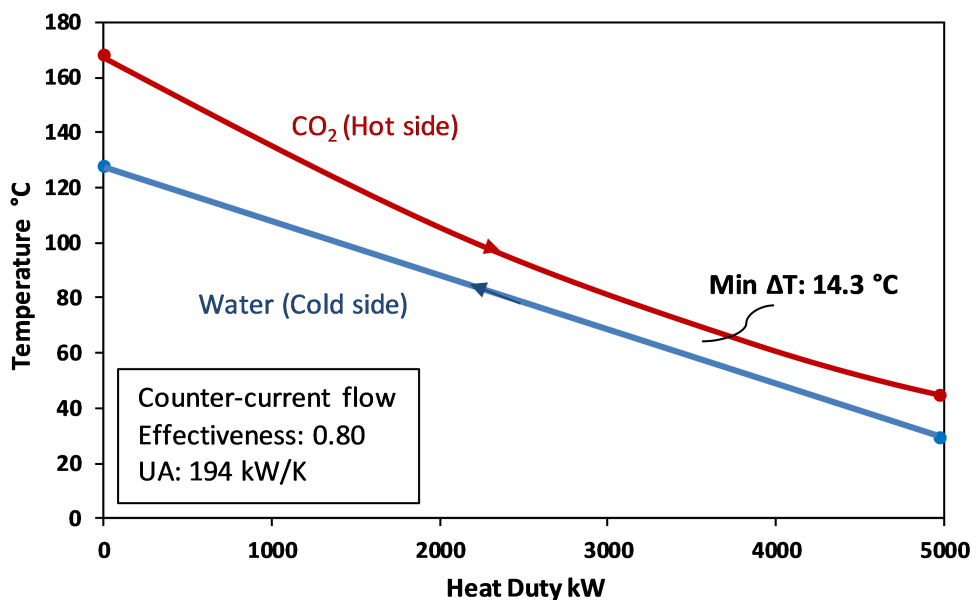


Figure 6.5: Q-T diagram of the coupling heat exchanger (cooler) between topping and bottoming cycles.

Last but not least, the intrinsic problem of sCO_2 cycles, i.e. high temperature head addition to the cycle, is overcome owing to the utilization of convective heat transfer from the flue gas under 402.5 °C to the bottoming cycle. Note that the heat addition to the proposed topping sCO_2 cycle takes place between States 4 and 5 in Figure 6.6. As mentioned in previous chapter, in order to overcome this drawback, several authors in the literature suggested adding a second sCO_2 cycle at the tail end of the primary topping cycle, ending up two sCO_2 cycles used in cascaded manner. Therefore,

the requirement of using additional sCO₂ components (recuperators, compressors, turbines) is eliminated in the proposed hybrid design. 90% of the biomass heat is successfully transferred to topping and bottoming cycles. As stated by Manente and Fortuna on their sCO₂ cycle design for waste heat recovery, one of the main novelties in the recent literature on hybrid plant layouts is the sharing of some equipment to reduce the number of components[112]. Considering the proposed hybrid power plant configuration in this thesis where the existing components of KZD-1 are intended to be utilized to the full extent, this novelty is inarguably accomplished.

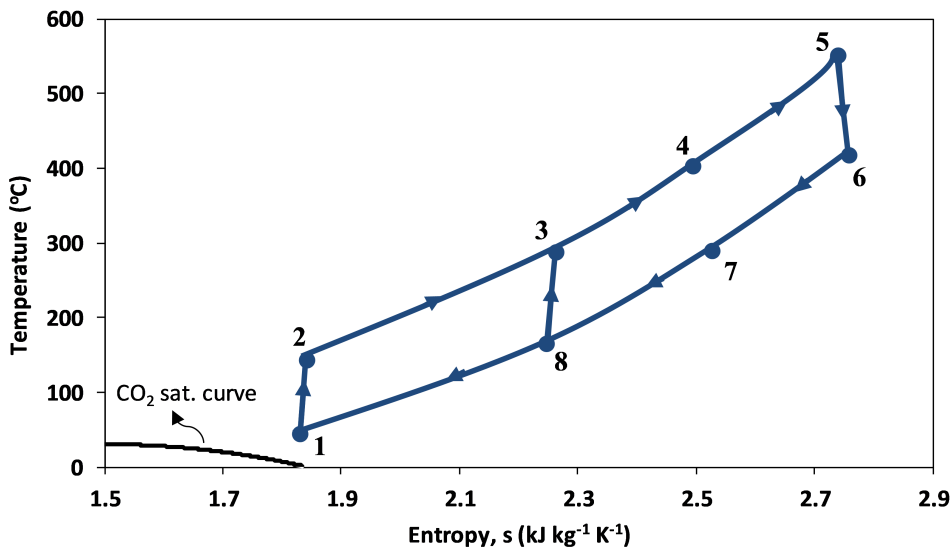


Figure 6.6: T-s diagram of the proposed topping cycle.

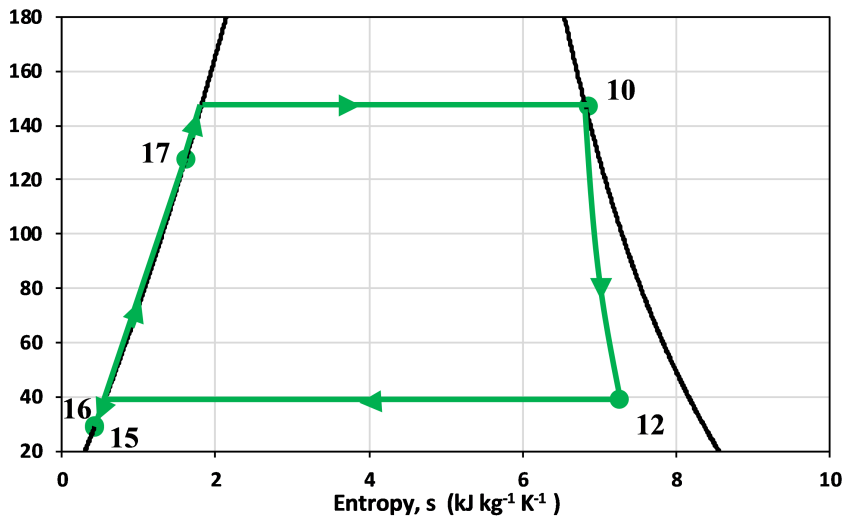


Figure 6.7: T-s diagram of the proposed bottoming cycle.

CHAPTER 7

CONCLUSION

In this thesis, Kızıldere-1 (KZD-1) Geothermal Electric Power Plant is hybridized using a biomass driven supercritical CO_2 topping cycle.

Olive residue (OR) is used as solid biomass fuel source due to being abundantly present in Southwestern Anatolia where KZD-1 is located. The characterization of the fuel is done for the particular OR samples collected from an olive oil factory nearby KZD-1 site. Thermogravimetric analysis (TGA) is used to determine the kinetic parameters under heating rate of 20 °C/min. Two main stages are observed for combustion, and the apparent activation energies are calculated as 32.6 and 17 kJ/mol for the respective stages. The results on kinetic parameters are in line with other OR results in the literature. The slagging and fouling potential for the studied OR is calculated based on the indices in the literature. It is found that the formation of thick deposits (indicated by F_I due to high CaO concentration) might not be removed due to low viscosity of slag (indicated by S_R due to high K_2O concentration). Therefore, the blends of studied OR with other fuels and inorganic materials [113] or co-firing can be used to decrease this potential [114, 115].

It is aimed to increase the net power output of the hybrid plant to rated output of KZD-1 GEPP (17.8 MWe) while keeping the hybrid cycle thermal efficiency, and the topping cycle as high and as small as possible, respectively. Overall, hybrid cycle thermal efficiency and biomass-to-electricity-ratio of 24.5% and 22% are achieved, respectively. The net power output of the hybrid power plant is increased to 17.8 MWe while the net production of the topping cycle is kept at 3.2 MWe. Corresponding fuel consumption for the hybrid plant is found as 2.2 kg/s.

Two intrinsic problems of sCO₂ cycles, namely pinch-point and high temperature head addition, are overcome by means of hybridization. No pinch-point problem is observed in the cooler of topping sCO₂ cycle. There are two reasons for this improvement. First, since the flow is split as required by the recompression sCO₂ cycle, the heat duty on the cooler is lightened, making it less susceptible to pinch-point problem. Second, the main compression process for the topping cycle slightly deviated from optimum conditions (shifted towards right on the T-s diagram in Figure 6.6) due to the heat exchange between two cycles. Note that the thermophysical properties of CO₂ exhibits unique properties at the vicinity of its critical point (Figure 2.6). Although the cycle efficiency is penalized, deviation from the critical point of CO₂ is another reason for not encountering a pinch-point problem in the cooler where 14.3 °C minimum temperature difference is ensured. The heat addition to sCO₂ cycle is done between 402.5 and 550 °C. Proposed hybrid model allows utilizing the heat in the flue gas under 402.5 °C in the bottoming cycle. Therefore the requirement of adding another sCO₂ cycle at the tail end of the topping sCO₂ cycle is eliminated.

7.1 Economical and Environmental Impacts

Based upon the discussions with geothermal power plant investors in Turkey it is found out that the changing the wellhead and operating conditions at any geothermal site is strictly abstained. Therefore, the proposed hybrid plant is done so that existing wellhead and operating conditions of KZD-1 is not changed. Only the steam flow rate feeding the KZD-1 turbine, which is normally working under capacity, is increased by means of biomass combustion. In this sense, hybridization of KZD-1 becomes plug-and-play concept. In order to address flexibility, the proposed working fluid rates for topping and bottoming cycle (45 kg/s and 12 kg/s) can represent the maximum demand in electricity. Depending on the demand or price of electricity (since KZD-1 is selling electricity to open market) these flow rates can be adjusted so that the intensive properties presented in Table 6.2 remains constant. Under the transient load with varying extensive properties, the fluctuations are confined to the hybrid (topping+bottoming) cycle so that the operating conditions of KZD-1 is not affected. KZD-1 continues to operate at 9.3 MWe (hypothetical) and 1.3 MWe (real).

The electricity prices generally vary throughout the day as it can be seen from the realtime market price curve of MWh electricity in Turkey for the day April 30th, 2020 in Figure 7.1. This price fluctuation is caused by several factors such as the variations in electricity production by solar photovoltaic and wind, weather conditions, and demand. Apart from the daily fluctuations, the geothermal electricity production has a fundamental problem of efficiency drop in hot summer months. For instance, the average weather temperature increases 21.8 °C from winter to summer (July avg: 27.9 °C, January avg: 6.1 °C) for city of Denizli where KZD-1 is located [116]. This weather temperature dictates the condensation (minimum) temperature, thereby decreases the thermal efficiency of geothermal power plants significantly. Ultimately, Turkey’s nominal geothermal electricity production decreases almost 20% from winter to summer [117]. If the proposed hybrid plant can respond the seasonal and daily fluctuations by means of increase in its flexibility, additional profit can be made by the power plant investors. In fact, it is also the main motivation of H2020 project GeoSmart, and the integration of sCO₂ cycle in this thesis supports this flexibility potential.

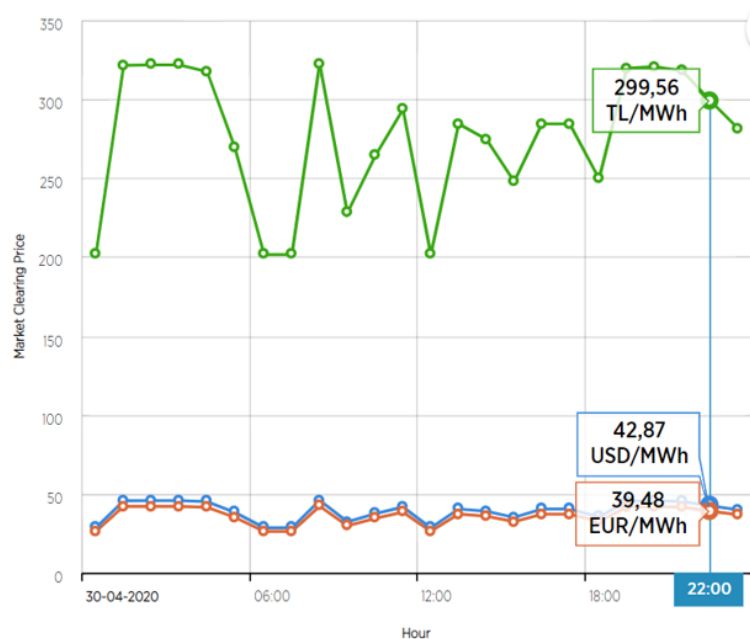


Figure 7.1: Electricity Market Price in Turkey for MWh electricity on April 30th, 2020. The image is adapted from Transparency Platform EPIAŞ [117].

This study does not include a quantitative economic or LCoE analysis since there are

uncertainties related to non-commercial sCO₂ cycles. However, the topping sCO₂ cycle is kept relatively small, i.e. 3.2 MWe, and almost 70% of the biomass heat is utilized in bottoming cycle (Figure 6.2) using the existing components of KZD-1 to avoid potential investment costs.

Olive residue is used as a fuel source, which is abundantly found in Southwestern Anatolia. Although olive residue cannot be considered as waste since it is already used for domestic heating and has an economic value, it is still more economic and environmentally friendly compared to Turkish lignites and import coal. As an adverse impact, high slagging and fouling potential is predicted for the studied olive residue based on the indices in the literature. However, the ash content of the OR is low (1.9%) especially compared to ash content of Turkish lignites, e.g. Soma lignite 13%, Tunçbilek lignite 14% [118]. This indicates that the maintenance to remove slagging and fouling can be done less frequently compared to industrial boilers using Turkish lignites as the fuel. Moreover, the ash from the olive residue can further be utilized as additive for agriculture or reconditioning of the soil. Considering that Büyük Menderes Plain is one of the biggest agricultural site of Turkey, zero waste management can be achieved with a sustainable manner.

7.2 Challenges and Future Work

Although sCO₂ cycles offer great potential for flexible electricity generation, they are next generation power cycles and require advanced turbomachinery components. For instance, the isentropic efficiency for the modeled sCO₂ turbine and compressors used in thesis are 92%, whereas 96% effectiveness are assumed for the recuperators. Despite the existence of bench scale demonstrations with advanced turbomachinery components [41, 42, 43, 44], there has not been a full-scale sCO₂ cycle power block over 1 MWe as of 2020. The first commercial demonstrations are expected by 2022 [39]. Apart from the challenges in turbomachinery to build commercial sCO₂ cycles, there might be challenges related to the design of the novel heater proposed in this thesis. Although, the UA values are specified in Figure 6.3 regarding the radiative and convective sections of the boiler, the challenges to build a heater capable of supplying predetermined radiative and convective sections for two different types of working

fluids (water and CO_2) with the presence of phase change (water/steam) are not taken into account.

Some concluding remarks has to be made regarding the the hybridization of KZD-1 with biomass driven sCO₂ cycle. In this thesis, olive residue used as a fuel source to power the sCO₂ cycle and provide additional steam for the bottoming cycle due to its abundancy nearby KZD-1 geothermal site. However, it should be noted that the proposed hybrid power plant model and fuel selection are completely discrete phenomena. More clearly, the hybridization results can be adapted by a different single flash GEPP in Philippines using a rice husk as the fuel source. The calorific value and the composition of the fuel are the only concepts that are taken into account during the design of the hybrid plant. The rest of the biomass characterization results in this thesis are presented to supply preliminary findings regarding the potential of using local biomass fuel source of olive residue in Western Anatolia. Lastly, some geochemical features of KZD-1 site are completely ignored throughout this thesis. For example, the geothermal brine in KZD-1 site is so rich in terms of CO_2 that substantial compressor power (2 MWe) is used to extract the CO_2 after the seperator. Considering the real net power output of the KZD-1, i.e. 3.3 MWe due to 28% turbine isentropic efficiency, the real electricity production is as low as 1.3 MWe.

In conclusion, the efforts on hybridization of geothermal with biomass driven sCO₂ cycle in this thesis represent the steady state case for maximum power output conditions of the hybrid plant with presented energetic results only, and lacks a vital exergy analysis. As a future work, exergy and economic analysis with varying load conditions can be done as further improvement. Nonetheless, it is believed that studies such as this thesis can form the initial block for the future scenarios that combines sCO₂ cycles with their potentially biggest commercial rival, steam Rankine cycles.

REFERENCES

- [1] World Bank, “Terms of Reference: Characterizing the declining CO2 emissions from Turkish geothermal power plants,” 2019.
- [2] A. Richter, “Turkey targets 2,000 MW geothermal power generation capacity by 2020,” 2019.
- [3] MTA, “Türkiye Jeotermal Enerji Potansiyeli ve Arama Çalışmaları,” tech. rep., Republic of Turkey General Directorate of Mineral Research and Exploration, 2020.
- [4] FAO, “FAOSTAT Databank.”
- [5] International Olive Council, “The Turkish Olive Oil Sector,” 2017.
- [6] I. Chemical and P. Analysis, *Biomass 8 8.1*. 2016.
- [7] N. S. Suresh, N. C. Thirumalai, and S. Dasappa, “Modeling and analysis of solar thermal and biomass hybrid power plants,” *Applied Thermal Engineering*, 2019.
- [8] D. Meyer-Kohlstock, T. Haupt, E. Heldt, N. Heldt, and E. Kraft, “Biochar as additive in biogas-production from bio-waste,” *Energies*, vol. 9, no. 4, 2016.
- [9] F. Monlau, C. Sambusiti, N. Antoniou, A. Barakat, and A. Zabaniotou, “A new concept for enhancing energy recovery from agricultural residues by coupling anaerobic digestion and pyrolysis process,” *Applied Energy*, 2015.
- [10] D. D. Toporov, “Theoretical Aspects of Burning Pulverised Fuel in Atmosphere,” in *Combustion of Pulverised Coal in a Mixture of Oxygen and Recycled Flue Gas*, 2014.
- [11] S. Pereira and M. Costa, “Short rotation coppice for bioenergy: From biomass characterization to establishment – A review,” 2017.

- [12] M. Mandø, "Direct combustion of biomass," in *Biomass Combustion Science, Technology and Engineering*, 2013.
- [13] S. G. Sahu, N. Chakraborty, and P. Sarkar, "Coal-biomass co-combustion: An overview," 2014.
- [14] A. W. Coats and J. P. Redfern, "Thermogravimetric Analysis A Review," *Principles and Applications of Thermal Analysis*, vol. 88, pp. 906–919, 1963.
- [15] F. Yousefzad Farrokhi and F. Kazanç, "Combustion Behavior and Kinetics of Turkish Lignite Blended with Biomass/Magnesite Dust," *Journal of Energy Engineering*, vol. 144, no. 6, pp. 1–13, 2018.
- [16] D. Magalhães, F. Kazanç, A. Ferreira, M. Rabaçal, and M. Costa, "Ignition behavior of Turkish biomass and lignite fuels at low and high heating rates," *Fuel*, vol. 207, pp. 154–164, 2017.
- [17] N. S. Yuzbasi and N. Selçuk, "Air and oxy-fuel combustion characteristics of biomass/lignite blends in TGA-FTIR," *Fuel Processing Technology*, 2011.
- [18] A. Arenillas, F. Rubiera, B. Arias, J. J. Pis, J. M. Faúndez, A. L. Gordon, and X. A. García, "A TG/DTA study on the effect of coal blending on ignition behaviour," *Journal of Thermal Analysis and Calorimetry*, vol. 76, no. 2, pp. 603–614, 2004.
- [19] "Chapter 3 Theory of Solid State Reaction Kinetics," in *Comprehensive Chemical Kinetics*, 1980.
- [20] S. De, A. Kumar, A. V. S. Moholkar Bhaskar, and T. Editors, *Coal and Biomass Gasification Energy, Environment, and Sustainability Recent Advances and Future Challenges*. 2018.
- [21] D. W. van Krevelen, C. van Heerden, and F. J. Huntjes, "Physicochemical aspects of the pyrolysis of coal and related organic compound," *Fuel*, vol. 30, pp. 253–259, 1951.
- [22] H. E. Kissinger, "Reaction Kinetics in Differential Thermal Analysis," *Analytical Chemistry*, vol. 29, no. 11, pp. 1702–1706, 1957.

- [23] J. Flynn and L. Wall, "General Treatment of the Thermogravimetry of Polymers," *JOURNAL OF RESEARCH of the National Bureau of Standards - A. Physics and Chemistry*, vol. 70A, no. 6, pp. 487–523, 1966.
- [24] T. Ozawa, "A New Method of Analyzing Thermogravimetric Data," *Bulletin of the Chemical Society of Japan*, vol. 38, no. 11, pp. 1881–1886, 1965.
- [25] S. Vyazovkin and D. Dollimore, "Linear and nonlinear procedures in isoconversional computations of the activation energy of nonisothermal reactions in solids," *Journal of Chemical Information and Computer Sciences*, vol. 36, no. 1, pp. 42–45, 1996.
- [26] T. W. and Chen, "Kinetic Study on the Thermal Dehydration of $\text{CaCO}_3 \cdot \text{H}_2\text{O}$ by the Master Plots Method," *AIChE Journal*, vol. 52, no. 6, pp. 2211–2216, 2006.
- [27] J. A. Kennedy and S. M. Clark, "A new method for the analysis of non-isothermal DSC and diffraction data," *Thermochimica Acta*, 1997.
- [28] D. Magalhães, F. Kazanç, J. Riaza, S. Erensoy, Ö. Kabaklı, and H. Chalmers, "Combustion of Turkish lignites and olive residue: Experiments and kinetic modelling," *Fuel*, vol. 203, pp. 868–876, 2017.
- [29] F. Guo, Y. He, A. Hassanpour, J. Gardy, and Z. Zhong, "Thermogravimetric analysis on the co-combustion of biomass pellets with lignite and bituminous coal," *Energy*, 2020.
- [30] F. Ferrara, A. Orsini, A. Plaisant, and A. Pettinau, "Pyrolysis of coal, biomass and their blends: Performance assessment by thermogravimetric analysis," *Bioresource Technology*, 2014.
- [31] O. Chansa, Z. Luo, and C. Yu, "Study of the kinetic behaviour of biomass and coal during oxyfuel co-combustion," *Chinese Journal of Chemical Engineering*, 2020.
- [32] X. Liu, M. Chen, and Y. Wei, "Kinetics based on two-stage scheme for co-combustion of herbaceous biomass and bituminous coal," *Fuel*, vol. 143, pp. 577–585, 2015.

- [33] K. Konwar, H. P. Nath, N. Bhuyan, B. K. Saikia, R. C. Borah, A. C. Kalita, and N. Saikia, “Effect of biomass addition on the devolatilization kinetics, mechanisms and thermodynamics of a northeast Indian low rank sub-bituminous coal,” *Fuel*, 2019.
- [34] D. López-González, A. Avalos-Ramirez, A. Giroir-Fendler, S. Godbout, M. Fernandez-Lopez, L. Sanchez-Silva, and J. L. Valverde, “Combustion kinetic study of woody and herbaceous crops by thermal analysis coupled to mass spectrometry,” *Energy*, vol. 90, no. x, pp. 1626–1635, 2015.
- [35] A. Álvarez, C. Pizarro, R. García, J. L. Bueno, and A. G. Lavín, “Determination of kinetic parameters for biomass combustion,” *Bioresource Technology*, vol. 216, pp. 36–43, 2016.
- [36] M. V. Kok and E. Özgür, “Thermal analysis and kinetics of biomass samples,” *Fuel Processing Technology*, vol. 106, no. February 2013, pp. 739–743, 2013.
- [37] C. Buratti, S. Mousavi, M. Barbanera, E. Lascaro, F. Cotana, and M. Bufacchi, “Thermal behaviour and kinetic study of the olive oil production chain residues and their mixtures during co-combustion,” *Bioresource Technology*, vol. 214, pp. 266–275, 2016.
- [38] F. Crespi, G. Gavagnin, D. Sánchez, and G. S. Martínez, “Supercritical carbon dioxide cycles for power generation: A review,” 2017.
- [39] J. Marion, “10 MWe Supercritical Carbon Dioxide (sCO₂) Pilot Power Plant,” tech. rep., GTI, 2018.
- [40] M. Utamura, “Thermodynamic analysis of part- flow cycle supercritical CO₂ gas turbines,” *Proceedings of the ASME Turbo Expo*, vol. 2, no. November, pp. 423–430, 2008.
- [41] M. Utamura, H. Hasuike, K. Ogawa, T. Yamamoto, T. Fukushima, T. Watanabe, and T. Himeno, “Demonstration of Supercritical CO₂ Closed Regenerative Brayton Cycle in a Bench Scale Experiment,” in *Proceedings of ASME Turbo Expo*, (Copenhagen, Denmark GT2012-68697), pp. 1–10, 2012.
- [42] V. Dostal and P. Hajek, “Proceedings of the 2014 22nd International Conference on Nuclear Engineering,” (Prague, Czech Republic), pp. 1–7, 2014.

- [43] T. Conboy, S. Wright, J. Pasch, D. Fleming, G. Rochau, and R. Fuller, "Performance characteristics of an operating supercritical CO₂ brayton cycle," *Journal of Engineering for Gas Turbines and Power*, vol. 134, no. 11, pp. 1–12, 2012.
- [44] T. Conboy, J. Pasch, and D. Fleming, "Control of a supercritical CO₂ recompression brayton cycle demonstration loop," *Journal of Engineering for Gas Turbines and Power*, vol. 135, no. 11, pp. 1–12, 2013.
- [45] G. Angelino, "Carbon dioxide condensation cycles for power production," *Journal of Engineering for Gas Turbines and Power*, vol. 90, no. 3, pp. 287–295, 1968.
- [46] E. G. Feher, "The supercritical thermodynamic power cycle," *Energy Conversion*, vol. 8, no. 2, pp. 85–90, 1968.
- [47] X. Wang, Q. Liu, Z. Bai, J. Lei, and H. Jin, "Thermodynamic Analysis of the Cascaded Supercritical CO₂ Cycle Integrated with Solar and Biomass Energy," in *Energy Procedia*, 2017.
- [48] S. M. Besarati and D. Y. Goswami, "Supercritical CO₂ and other advanced power cycles for concentrating solar thermal (CST) systems," *Advances in Concentrating Solar Thermal Research and Technology*, no. January, pp. 157–178, 2017.
- [49] N. Bonyadi, E. Johnson, and D. Baker, "Technoeconomic and exergy analysis of a solar geothermal hybrid electric power plant using a novel combined cycle," *Energy Conversion and Management*, vol. 156, no. October 2017, pp. 542–554, 2018.
- [50] J. D. McTigue, J. Castro, G. Mungas, N. Kramer, J. King, C. Turchi, and G. Zhu, "Hybridizing a geothermal power plant with concentrating solar power and thermal storage to increase power generation and dispatchability," *Applied Energy*, 2018.
- [51] A. Borsukiewicz-Gozdur, "Dual-fluid-hybrid power plant co-powered by low-temperature geothermal water," *Geothermics*, vol. 39, no. 2, pp. 170–176, 2010.

- [52] S. Briola, R. Gabbrielli, and A. Bischi, “Off-design performance analysis of a novel hybrid binary geothermal-biomass power plant in extreme environmental conditions,” *Energy Conversion and Management*, vol. 195, no. May, pp. 210–225, 2019.
- [53] H. Rostamzadeh, S. G. Gargari, A. S. Namin, and H. Ghaebi, “A novel multi-generation system driven by a hybrid biogas-geothermal heat source, Part I: Thermodynamic modeling,” *Energy Conversion and Management*, vol. 177, no. June, pp. 535–562, 2018.
- [54] R. DiPippo, “Combined and hybrid geothermal power systems,” in *Geothermal Power Generation: Developments and Innovation*, 2016.
- [55] S. M. Besarati and D. Yogi Goswami, “Analysis of Advanced Supercritical Carbon Dioxide Power Cycles With a Bottoming Cycle for Concentrating Solar Power Applications,” *Journal of Solar Energy Engineering*, vol. 136, no. 1, pp. 1–7, 2014.
- [56] H. Zhang, S. Shao, H. Zhao, and Z. Feng, “Gt2014-26500 Thermodynamic Analysis of a Sco 2 Part-Flow Cycle Combined With,” pp. 1–8, 2014.
- [57] X. Wang and Y. Dai, “Exergoeconomic analysis of utilizing the transcritical CO₂ cycle and the ORC for a recompression supercritical CO₂ cycle waste heat recovery: A comparative study,” *Applied Energy*, vol. 170, pp. 193–207, 2016.
- [58] A. D. Akbari and S. M. Mahmoudi, “Thermoeconomic analysis & optimization of the combined supercritical CO₂ (carbon dioxide) recompression Brayton/organic Rankine cycle,” *Energy*, vol. 78, pp. 501–512, 2014.
- [59] X. Wang, Y. Wu, J. Wang, and Y. Dai, “Thermo-economic Analysis of a Recompression sCO₂ Cycle Combined with a tCO₂ Cycle,” in *Proceedings of ASME Turbo Expo 2015: Turbine Technical Conference and Exposition GT2015*, (Montréal, Canada), pp. 1–11, 2015.
- [60] X. Wang, J. Wang, P. Zhao, and Y. Dai, “Thermodynamic Comparison and Optimization of Supercritical CO₂ Brayton Cycles with a Bottoming Transcritical CO₂ Cycle,” *Journal of Energy Engineering*, vol. 142, no. 3, pp. 1–11, 2016.

- [61] C. Wu, X. J. Yan, S. S. Wang, K. L. Bai, J. Di, S. F. Cheng, and J. Li, "System optimisation and performance analysis of CO₂ transcritical power cycle for waste heat recovery," *Energy*, vol. 100, pp. 391–400, 2016.
- [62] M. Mecheri and Y. Le Moullec, "Supercritical CO₂ Brayton cycles for coal-fired power plants," *Energy*, 2016.
- [63] Y. Le Moullec, "Conceptual study of a high efficiency coal-fired power plant with CO₂ capture using a supercritical CO₂ Brayton cycle," *Energy*, vol. 49, no. 1, pp. 32–46, 2013.
- [64] G. Manente and A. Lazzaretto, "Innovative biomass to power conversion systems based on cascaded supercritical CO₂ Brayton cycles," *Biomass and Bioenergy*, 2014.
- [65] M. Utamura, "Thermal-hydraulic characteristics of microchannel heat exchanger and its application to solar gas turbines," *Proceedings of the ASME Turbo Expo*, vol. 4 PART A, no. May, pp. 287–294, 2007.
- [66] A. Roig, M. L. Cayuela, and M. A. Sánchez-Monedero, "An overview on olive mill wastes and their valorisation methods," *Waste Management*, vol. 26, no. 9, pp. 960–969, 2006.
- [67] G. Tamasi, C. Bonechi, A. Belyakova, A. Pardini, and C. Rossi, "the Olive Tree, a Source of Antioxidant Compounds," *Journal of the Siena Academy of Sciences*, vol. 8, no. 1, 2017.
- [68] M. C. Mayoral, M. T. Izquierdo, J. M. Andrés, and B. Rubio, "Different approaches to proximate analysis by thermogravimetry analysis," *Thermochimica Acta*, vol. 370, no. 1-2, pp. 91–97, 2001.
- [69] B. Janković, B. Adnadević, and J. Jovanović, "Application of model-fitting and model-free kinetics to the study of non-isothermal dehydration of equilibrium swollen poly (acrylic acid) hydrogel: Thermogravimetric analysis," *Thermochimica Acta*, 2007.
- [70] M. V. Gil, D. Casal, C. Pevida, J. J. Pis, and F. Rubiera, "Thermal behaviour and kinetics of coal/biomass blends during co-combustion," *Bioresour. Technology*, vol. 101, no. 14, pp. 5601–5608, 2010.

- [71] A. B. Phadnis and V. V. Deshpande, "Determination of the kinetics and mechanism of a solid state reaction. A simple approach," *Thermochimica Acta*, vol. 62, no. 2-3, pp. 361–367, 1983.
- [72] C. Sheng and J. L. Azevedo, "Estimating the higher heating value of biomass fuels from basic analysis data," *Biomass and Bioenergy*, vol. 28, no. 5, pp. 499–507, 2005.
- [73] D. A. Tilman, *Wood as an energy resource*. New York: Academic Press, 1978.
- [74] Institute of Gas Technology, *Coal conversion systems technical data book*. NTIS, Springfield, VA, erda no. f ed., 1978.
- [75] M. Graboski and R. Bain, "Properties of biomass relevant to gasification," in *Biomass Gasification: Principles and Technology* (T. Reed, ed.), pp. 41–71, NJ: Noyes Data Corporation, 1981.
- [76] B. M. Jenkins and J. M. Ebeling, "Correlation of physical and chemical properties of terrestrial biomass with conversion," in *Symposium Energy from Biomass and Waste IX IGT*, p. 371, 1985.
- [77] A. Demirbaş, "Calculation of high heating values of biomass fuels," *Fuel*, no. 76, pp. 431–434, 1997.
- [78] S. A. Channiwala and P. P. Parikh, "A unified correlation for estimating HHV of solid, liquid and gaseous fuels," *Fuel*, vol. 81, no. 8, pp. 1051–1063, 2002.
- [79] D. J. Vega-Nieva, "Slagging and Fouling Risks Derived from the Combustion of Solid Biofuels," vol. 85, pp. 137–147, 2015.
- [80] T. R. Miles, T. R. Miles, L. L. Baxter, R. W. Bryers, B. M. Jenkins, and L. L. Oden, "Boiler deposits from firing biomass fuels," *Biomass and Bioenergy*, vol. 10, no. 2-3, pp. 125–138, 1996.
- [81] M. Pronobis, "Evaluation of the influence of biomass co-combustion on boiler furnace slagging by means of fusibility correlations," *Biomass and Bioenergy*, vol. 28, no. 4, pp. 375–383, 2005.

- [82] P. Teixeira, H. Lopes, I. Gulyurtlu, N. Lapa, and P. Abelha, "Evaluation of slagging and fouling tendency during biomass co-firing with coal in a fluidized bed," *Biomass and Bioenergy*, vol. 39, pp. 192–203, 2012.
- [83] L. Febrero, E. Granada, A. Regueiro, and J. L. Míguez, "Influence of combustion parameters on fouling composition after wood pellet burning in a lab-scale low-power boiler," *Energies*, vol. 8, no. 9, pp. 9794–9816, 2015.
- [84] C. Sheng and J. L. Azevedo, "Modeling biomass devolatilization using the chemical percolation devolatilization model for the main components," *Proceedings of the Combustion Institute*, 2002.
- [85] C. Zou, L. Zhang, S. Cao, and C. Zheng, "A study of combustion characteristics of pulverized coal in O₂/H₂O atmosphere," *Fuel*, vol. 115, pp. 312–320, 2014.
- [86] Q. Haiying and Z. Bo, *Cleaner Combustion and Sustainable World*. New York: Springer, 2013.
- [87] T. d. P. Protásio, M. G. Junior, S. Mirmehdi, P. F. Trugilho, A. Napoli, and K. M. Knovack, "Combustão da biomassa E do carvão vegetal da casca do coco babaçu," *Cerne*, vol. 23, no. 1, pp. 1–10, 2017.
- [88] S. W. Park, C. H. Jang, K. R. Baek, and J. K. Yang, "Torrefaction and low-temperature carbonization of woody biomass: Evaluation of fuel characteristics of the products," *Energy*, vol. 45, no. 1, pp. 676–685, 2012.
- [89] S. S. Idris, N. A. Rahman, and K. Ismail, "Combustion characteristics of Malaysian oil palm biomass, sub-bituminous coal and their respective blends via thermogravimetric analysis (TGA)," *Bioresource Technology*, vol. 123, no. 2012, pp. 581–591, 2012.
- [90] P. B. Gangavati, M. J. Safi, A. Singh, B. Prasad, and I. M. Mishra, "Pyrolysis and thermal oxidation kinetics of sugar mill press mud," *Thermochimica Acta*, vol. 428, no. 1-2, pp. 63–70, 2005.
- [91] G. Wang, J. Zhang, J. Shao, and S. Ren, "Characterisation and model fitting kinetic analysis of coal/biomass co-combustion," *Thermochimica Acta*, vol. 591, pp. 68–74, 2014.

- [92] M. X. Fang, D. K. Shen, Y. X. Li, C. J. Yu, Z. Y. Luo, and K. F. Cen, “Kinetic study on pyrolysis and combustion of wood under different oxygen concentrations by using TG-FTIR analysis,” *Journal of Analytical and Applied Pyrolysis*, vol. 77, no. 1, pp. 22–27, 2006.
- [93] “2018 Yılı Zeytin ve Zeytinyağı Raporu,” tech. rep., T.C. Ticaret Bakanlığı Esnaf, Sanatkarlar ve Kooperatifçilik Genel Müdürlüğü, 2019.
- [94] D. Vamvuka, N. Pasadakis, E. Kastanaki, P. Grammelis, and E. Kakaras, “Kinetic modeling of coal/agricultural by-product blends,” *Energy and Fuels*, vol. 17, no. 3, pp. 549–558, 2003.
- [95] A. I. Ferreiro, M. Rabaçal, and M. Costa, “A combined genetic algorithm and least squares fitting procedure for the estimation of the kinetic parameters of the pyrolysis of agricultural residues,” *Energy Conversion and Management*, vol. 125, pp. 290–300, 2016.
- [96] M. Massoudi and P. Wang, “A Brief Review of Viscosity Models for Slag in Coal Gasification,” no. November 2011, pp. 1–51, 2012.
- [97] R. DiPippo, *Geothermal power plants*, vol. 7. 2012.
- [98] I. Dincer and Y. Bicer, *Fundamentals of energy systems*. 2020.
- [99] C. S. Turchi, Z. Ma, and J. Dyreby, “Supercritical carbon dioxide power cycle configurations for use in concentrating solar power systems,” *Proceedings of the ASME Turbo Expo*, vol. 5, no. April, pp. 967–973, 2012.
- [100] T. Neises and C. Turchi, “A comparison of supercritical carbon dioxide power cycle configurations with an emphasis on CSP applications,” *Energy Procedia*, vol. 49, pp. 1187–1196, 2014.
- [101] G. Gokcen, H. K. Ozturk, and A. Hepbasli, “Overview of Kizildere Geothermal Power Plant in Turkey,” *Energy Conversion and Management*, vol. 45, no. 1, pp. 83–98, 2004.
- [102] S. Akar, C. Augustine, P. Kurup, and M. Mann, “Global value chain and manufacturing analysis on geothermal power plant turbines,” *Transactions - Geothermal Resources Council*, vol. 41, no. September, pp. 2384–2400, 2017.

- [103] Y. Cao, A. S. Rattner, and Y. Dai, “Thermoeconomic analysis of a gas turbine and cascaded CO₂ combined cycle using thermal oil as an intermediate heat-transfer fluid,” *Energy*, vol. 162, pp. 1253–1268, 2018.
- [104] X. Wang, Q. Liu, Z. Bai, J. Lei, and H. Jin, “Thermodynamic Analysis of the Cascaded Supercritical CO₂ Cycle Integrated with Solar and Biomass Energy,” *Energy Procedia*, vol. 105, pp. 445–452, 2017.
- [105] E. Sun, J. Xu, M. Li, H. Li, C. Liu, and J. Xie, “Synergetics: The cooperative phenomenon in multi-compressions S-CO₂ power cycles,” *Energy Conversion and Management: X*, vol. 7, no. April, p. 100042, 2020.
- [106] C. Wu, X. J. Yan, S. S. Wang, K. L. Bai, J. Di, S. F. Cheng, and J. Li, “System optimisation and performance analysis of CO₂ transcritical power cycle for waste heat recovery,” *Energy*, 2016.
- [107] Y. M. Kim, C. G. Kim, and D. Favrat, “Transcritical or supercritical CO₂ cycles using both low- and high-temperature heat sources,” *Energy*, 2012.
- [108] C. S. Turchi, Z. Ma, T. Neises, and M. Wagner, “Thermodynamic Study of Advanced Supercritical Carbon Dioxide Power Cycles for High Performance Concentrating Solar Power Systems,” pp. 1–9, 2020.
- [109] S. M. Besarati and D. Y. Goswami, “(validation için iyi gibi) Analysis of advanced supercritical carbon dioxide power cycles with a bottoming cycle for concentrating solar power applications,” *ASME International Mechanical Engineering Congress and Exposition, Proceedings (IMECE)*, vol. 6 A, no. February, pp. 2–8, 2013.
- [110] C. Yin, L. A. Rosendahl, and S. K. Kær, “Grate-firing of biomass for heat and power production,” *Progress in Energy and Combustion Science*, vol. 34, no. 6, pp. 725–754, 2008.
- [111] P. Stehlík, S. Zagermann, and T. Gängler, “Furnace integration into processes justified by detailed calculation using a simple mathematical model,” *Chemical Engineering & Processing: Process Intensification*, vol. 34, no. 1, pp. 9–23, 1995.

- [112] G. Manente and F. M. Fortuna, “Supercritical CO₂ power cycles for waste heat recovery: A systematic comparison between traditional and novel layouts with dual expansion,” *Energy Conversion and Management*, 2019.
- [113] K. Tabit, H. Hajjou, M. Waqif, and L. Saâdi, “Effect of CaO/SiO₂ ratio on phase transformation and properties of anorthite-based ceramics from coal fly ash and steel slag,” *Ceramics International*, vol. 46, no. 6, pp. 7550–7558, 2020.
- [114] Y. Shao, J. Wang, F. Preto, J. Zhu, and C. Xu, “Ash deposition in biomass combustion or co-firing for power/heat generation,” *Energies*, vol. 5, no. 12, pp. 5171–5189, 2012.
- [115] Y. Zhu, Y. Niu, H. Tan, and X. Wang, “Short review on the origin and counter-measure of biomass slagging in grate furnace,” *Frontiers in Energy Research*, vol. 2, no. FEB, pp. 1–10, 2014.
- [116] General Directorate of Meteorology (MGM), Republic of Turkey, “Official Weather Statistics (1981-2010),” tech. rep., 2020.
- [117] EPIAŞ, “Transparency Platform,” tech. rep., 2020.
- [118] D. Magalhães, A. Panahi, F. Kazanç, and Y. A. Levendis, “Comparison of single particle combustion behaviours of raw and torrefied biomass with Turkish lignites,” *Fuel*, 2019.